



**UCGE Reports
Number 20159**

Department of Geomatics Engineering

**The Development of a
Backpack Mobile Mapping System**

(URL: <http://www.geomatics.ucalgary.ca/links/GradTheses.html>)

by

Cameron MacKenzie Ellum

December, 2001



THE UNIVERSITY OF CALGARY

The Development of a Backpack Mobile Mapping System

by

Cameron MacKenzie Ellum

A THESIS

**SUBMITTED TO THE FACULTY OF GRADUATE STUDIES
IN PARTIAL FULFILLMENT OF THE REQUIREMENTS FOR THE
DEGREE OF MASTER OF SCIENCE**

DEPARTMENT OF GEOMATICS ENGINEERING

CALGARY, ALBERTA

DECEMBER, 2001

© Cameron MacKenzie Ellum 2001

Abstract

This research details the development of a backpack mobile mapping system. The system integrates an inclinometer, digital magnetic compass, dual-frequency GPS receiver and consumer digital camera into a multi-sensor mapping system. The GPS provides estimates of the camera's position at the exposure stations, and the magnetic compass and inclinometer provide estimates of the camera's attitude. These exterior orientation estimates are used together with image point measurements in a photogrammetric bundle adjustment, and the result is 3-D georeferenced coordinates. The design and implementation of the prototype system is detailed, and new techniques for including navigational data in a bundle adjustment are derived. Using the prototype system, absolute horizontal and vertical object space accuracies of 0.2 metres (RMS) and 0.3 metres (RMS), respectively, are achieved.

Acknowledgements

I would like to express my sincere gratitude to Dr. Naser El-Sheimy. Throughout the last two and a half years he has been both a generous supervisor and a good friend. Any academic accomplishments I have made during this period are as much a reflection of his efforts to motivate me as they are of anything else. Dr. Chapman and Dr. Schwarz are also thanked, both for their invaluable feedback on my thesis, and for educating and inspiring me during my undergraduate studies.

Many thanks go to my friends and colleagues. Michael Kern and Fadi Bayoud are thanked, in particular, for delaying my thesis by at least a year by making our work environment so much fun. Kris Morin is thanked for accompanying me on our many highly educational (if not in the way intended) foreign adventures. The help of Bruce Wright in getting the prototype system to work is greatly appreciated.

Special thanks go to my very special friend Lynn. Her companionship improved the quality of both my thesis and life. Perhaps more importantly she also taught me that when things get rough, to “suck-it-up, buttercup!”.

Finally, the deepest gratitude of all goes to my parents. This research, and indeed, my entire education, is the result of a thirst for knowledge that was sparked and encouraged by them. All that I am, and all that I ever will be, I owe to them.

Contents

Approval Page	ii
Abstract	iii
Acknowledgements	iv
List of Tables	viii
List of Figures	x
Notation	xiii
1 Introduction	1
1.1 Overview of Mobile Mapping Systems	4
1.2 History of Land-Based MMS	6
1.3 Research Objectives	11
1.4 Thesis Outline	11
2 Close-Range Photogrammetry	13
2.1 The Central Perspective Projection	15
2.2 Geometric Camera Calibration	21
2.2.1 Focal Length	22
2.2.2 Principal Point Offsets	24
2.2.3 Lens Distortion Parameters	26
2.2.4 Additional Parameters	31
2.2.5 Calibration Techniques	33
2.3 Extended Collinearity Equations	34
3 Adjustment of Photogrammetric Networks	37
3.1 Bundle Adjustment	38
3.2 Inclusion of GPS Positions	44

3.2.1	Traditional Method	44
3.2.2	Determination of the GPS/Camera Offset Vector	45
3.2.3	Modification of the Collinearity Equations	48
3.3	Inclusion of Orientation Observations	50
3.4	Inclusion of Relative Orientations	60
3.5	Using an ECEF Cartesian Frame as the Mapping Frame	64
3.6	A Note on Datum Definition and the Use of Inner Constraints	67
4	Navigation Sensors	70
4.1	GPS	70
4.2	Inclinometer	71
4.3	Digital Compass	74
5	System Implementation	77
5.1	System Components	77
5.1.1	NovAtel GPS Receiver	77
5.1.2	Leica Digital Compass/Inclinometer	79
5.1.3	Kodak Consumer Digital Camera	80
5.2	Configuration	83
5.3	Software	85
5.3.1	Bundle Adjustment	87
5.3.2	Graphical Point Picker	90
5.3.3	Other Software	93
5.4	System Operation	97
6	Testing and Results	99
6.1	Sensor Testing	99
6.1.1	Camera Calibration	100
6.1.2	DMC Accelerometer Testing	102
6.2	Proof-of-concept Testing	110
6.2.1	Test Field	110
6.2.2	Navigation Sensor Accuracy	113
6.2.3	Mapping Accuracy	116
6.3	Prototype System Testing	123
6.3.1	Test Field	123
6.3.2	Navigation Sensor Accuracy	124
6.3.3	Mapping Accuracy	129

7	Conclusions	134
7.1	Conclusions	134
7.2	Specific Contributions	136
7.3	Future Investigations	137
A	Derivations	148
A.1	Rotation Matrices and Derivatives	148
A.2	Derivatives of Roll, Pitch, and Yaw Rotation Matrix	150
A.3	Error Propagation for Angle Conversion	152
A.4	Linearised Collinearity Equations for Roll, Pitch, and Yaw Angles . .	157

List of Tables

1.1	Comparison of Current Spatial Data Collection Techniques	3
1.2	Implementations of Land-Based Multi-Sensor Systems	10
2.1	Categories of Photogrammetry	14
2.2	Camera Calibration Methods	35
4.1	GPS Accuracies	71
5.1	Leica DMC-SX Specifications	80
5.2	Kodak DC260 Specifications	82
5.3	IMU Calibration Software Testing	97
6.1	Kodak DC-260 Interior Orientation Stability	100
6.2	DMC Accelerometer Calibration	109
6.3	L1/L2 Carrier Phase Differential GPS Position Differences	114
6.4	C/A Code Differential GPS Position Differences	115
6.5	DMC Attitude Angle Differences	117
6.6	Revised DMC Attitude Angle Differences	119
6.7	Results (Approximate Camera to Object Point Distance = 20 m) . .	120
6.8	Results (Approximate Camera to Object Point Distance = 40 m) . .	121
6.9	Effect of Including Control or Network Observations	122
6.10	L1/L2 Carrier Phase Differential GPS Position Differences - Test 1 .	127
6.11	L1/L2 Carrier Phase Differential GPS Position Differences - Test 2 .	127
6.12	L1/L2 Carrier Phase Differential GPS Position Differences - Test 3 .	128
6.13	DMC Attitude Angle Differences – Test 1	129
6.14	DMC Attitude Angle Differences – Test 2	130
6.15	DMC Attitude Angle Differences – Test 3	130
6.16	Results (Approximate Camera to Object Point Distance = 40 m) . .	131

List of Figures

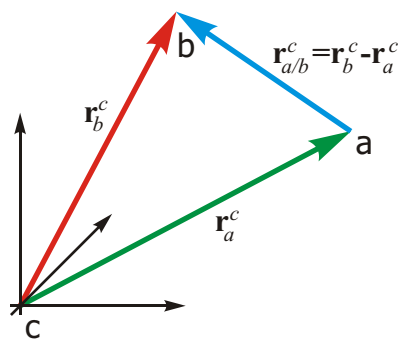
2.1	The Central Perspective Projection	16
2.2	Positive Digital Image	20
2.3	Focal Length	23
2.4	Principal Distance (after Moffit (1967))	24
2.5	Principal Point Offsets for a Digital Image	26
2.6	Symmetric Radial Distortion	28
2.7	Decentring Distortion	31
3.1	Relation between GPS antenna, camera, and object space point	48
3.2	Typical relationship between axes of orientation measuring device and camera	53
3.3	Monte Carlo simulation for angular error propagation	57
3.4	Distributions of roll, pitch, and yaw angles input into Monte Carlo simulation	57
3.5	Distributions ω , ϕ , and κ angles output from Monte Carlo simulation	58
4.1	Calculation of Roll and Pitch from the Gravity Vector	73
4.2	Capacitive-Based MEMs Accelerometer	74
5.1	Leica DMC-SX	81
5.2	Backpack MMS Logical Connections	84
5.3	Backpack MMS Schematic	85
5.4	Backpack MMS	86
5.5	Bundle Graphical User Interface (WinBundle)	91
5.6	Graphical Point Picker (GeoProject)	93
5.7	Photogrammetric Mark Interpolator	94
5.8	IMU Calibration Software	96
6.1	DC260 Symmetric Radial Distortion Profile	102
6.2	DMC-SX Accelerometer Measurements during Warm-Up	105
6.3	DMC-SX Angular Measurements during Warm-Up	107
6.4	DMC Angular Change During Cooling and Heating	108

6.5	First Test Field - Photo	111
6.6	First Test Field	112
6.7	DMC/Combined Adjustment Angle Differences	116
6.8	DMC/Combined Adjustment Angle Differences - Second Set of Far Images	118
6.9	Possible Result of Including Extra Constraints in Adjustment	122
6.10	Second Test Field - Photo	125
6.11	Second Test Field	126
6.12	Example of Poor Image Exposure	132

Notation

Convention

Vectors: Vectors are shown using bold lowercase letters and symbols. Position vectors, indicated by ' \mathbf{r} ', have both a superscript and a subscript. The former indicates which frame the vector is expressed in, and the latter indicates the start and end points of the vector, separated by '/'. If the start point of a vector is the same as the origin of the frame in which the vector is expressed, then it is not shown. For example, $\mathbf{r}_{a/b}^c$ is the position of 'a' with respect to 'b', expressed in the 'c' frame. The same position, relative to the origin of the 'c' frame, would be \mathbf{r}_a^c . Both vectors are shown below.



Position Vectors

Matrices: Matrices are shown using bold uppercase letters and symbols. Rotation matrices between co-ordinate systems, indicated by ' \mathbf{R} ', have a superscript and a subscript denoting the two co-ordinate frames. For example, \mathbf{R}_a^b is the matrix that rotates vectors in co-ordinate system ' a ' to vectors in co-ordinate system ' b '. The elementary rotation matrices, corresponding to rotations about the x , y and z axes, respectively, are indicated by \mathbf{R}_x , \mathbf{R}_y , and \mathbf{R}_z .

Symbols

Page is that on which symbol first occurs. Greek letters are listed as they are spelt in English.

A	design matrix	39
α	vector of angles	50
b	vector of GPS position biases	44
b_1, b_2	affinity and shear in-plane distortion terms	32
b_x, b_y, b_z	magnetic field measurements	75
bh_x, bh_y, bh_z	magnetic field measurements made by a level sensor	75
c	camera co-ordinate frame	16
c	principal distance	17
C	covariance matrix	40
CT	conventional terrestrial co-ordinate frame	65
d	vector of GPS position drifts	44
δ	vector of corrections to parameters	39
δr	symmetric radial lens distortion	28
$\Delta \mathbf{R}$	relative rotation matrix	61
$\delta x, \delta y$	corrections for lens and other image distortions	34
$\delta x_d, \delta y_d$	corrections for decentring lens distortion	28
δx_f	correction for affinity and shear in-plane distortion	32
$\delta x_r, \delta y_r$	corrections for symmetric radial lens distortion	29
$\Delta_x, \Delta_y, \Delta_z$	small angle rotations	59
e	exit angle for an image ray	23
g_x, g_y, g_z	gravity measurements	72
H	Helmert transformation matrix	67
i	incident angle for an image ray	23
i	image co-ordinate frame	24
k_i	coefficients of symmetric radial lens distortion	28
κ	rotation about the z-axis	17
l	vector of observations	39
λ	longitude	66
M	mapping/object co-ordinate frame	16
μ	scale between the camera frame and the mapping frame for a single image point	16
N	normal matrix	41
N, N'	front and rear nodal points	23
ω	rotation about the x-axis	17
p	point in camera frame	16

P	point in mapping frame	16
\mathbf{P}	weight matrix	40
p_1, p_2	coefficients of decentring lens distortion	30
$p(r)$	decentring lens distortion profile	30
ϕ	rotation about the y-axis	17
ϕ	latitude	65
ψ	yaw	52
r	radial distance from the principal point of best symmetry	28
\mathbf{r}	position vector	16
\mathbf{R}	rotation matrix	16
r_{ij}	elements of a rotation matrix	17
θ	pitch	52
\mathbf{u}	vector of constant terms	41
\mathbf{v}	vector of residuals	39
φ	roll	52
\mathbf{w}	vector of misclosures	40
\mathbf{x}	vector of parameters	39
\mathbf{x}^0	vector of parameter initial estimates	39
\bar{x}, \bar{y}	distance from principal point of best symmetry	28
X_c, Y_c, Z_c	elements of camera position vector in the mapping frame	17
x_o, y_o	principal point	24
x_p, y_p	image measurements of a point	17
X_P, Y_P, Z_P	elements of point position vector in the mapping frame	17
x_{pps}, y_{pps}	distances in image plane from principal point of best symmetry	28

Chapter 1

Introduction

The past 20 years have seen an explosive growth in the demand for geo-spatial data. This demand has numerous sources and takes many forms; however, the net effect is an ever-increasing thirst for data that is more accurate, has higher density, is produced more rapidly, and is acquired less expensively. For mapping and Geospatial Information Systems (GIS) projects this data has traditionally been collected using terrestrial surveying techniques or by aerial photogrammetric surveys. Unfortunately, the former technique is intrusive and not well suited for rapid or dense data collection, while the latter has large camera-to-object distances, does not provide complete coverage (i.e., only points visible from the air can be measured), and is highly weather-dependent. Both techniques are costly, and consequently are not well suited to frequent updating. More recently, point-wise GPS data collection systems have become popular. However, these systems – like traditional terrestrial surveys – still require each point of interest to be occupied, and therefore they do not significantly reduce either the cost or time requirements of data collection.

An alternative to both point-wise GPS and traditional techniques of data collection is the use of multi-sensor systems that integrate various navigation and remote sensing technologies together on a common aerial or land-based platform. These *Mobile Mapping Systems* (MMS) capitalise on the strengths of the individual technologies in order to increase the efficiency of data collection. The most important benefit of MMS is a reduction in both the time and cost of data collection; however, they also have a number of additional advantages. For example, both spatial and attribute information can be determined from the remotely sensed data. Furthermore, data can be archived and revisited, permitting additional data collection without additional field campaigns.

MMS can be air-based or land-based. Air-based MMS have the same limitations as traditional aerial photogrammetry – namely, its incomplete coverage and weather dependence. Consequently, for many projects, land-based MMS are the most effective system at overcoming the drawbacks of traditional data collection techniques. The remote sensors on land-based MMS enable less intrusive and more rapid data collection than other terrestrial techniques, and since the systems are land-based, they have smaller camera-to-object distances and can provide more complete coverage than aerial systems. Additionally, land-based MMS can operate in all but the most extreme weather conditions.

Of course, land-based MMS have their disadvantages. One key drawback of land systems is their inaccuracy at large camera-to-object distances. Another is that they may have difficulty with some imaging and point configurations. For many projects, however, the benefits of land-based MMS outweigh their drawbacks.

Table 1.1 shows a comparison of land-based MMS with alternative methods of

spatial data collection. Evident in this table is how multi-sensor systems combine the advantages of the individual alternative techniques.

Table 1.1: Comparison of Current Spatial Data Collection Techniques

Technique	Disadvantages	Advantages
Close-Range Photogrammetry	<i>Establishing sufficient control is difficult and expensive</i>	<i>Rapid data collection from images Data can be archived and revisited Less intrusive data collection</i>
Total Station Terrestrial surveying	<i>Labour intensive and slow Not suitable for dense data collection over a wide area Intrusive data collection</i>	<i>High relative accuracy</i>
Point-wise GPS	<i>Not suitable in urban centres or forested areas Not suitable for dense data collection over a wide area Intrusive data collection</i>	<i>Little skill required High relative and absolute accuracy accuracy</i>
Aerial Photogrammetric Surveys	<i>Establishing control is difficult and expensive Incomplete coverage - only points visible from the air can be collected Expensive data collection campaigns Weather-dependent</i>	<i>Rapid data collection from images Data collection can be partially automated Data can be archived and revisited Less intrusive data collection</i>
Land Based Mobile Mapping Systems	<i>High initial system cost Complex</i>	<i>Little or no control required Rapid and dense data collection over a wide area More cost-effective data acquisition Data can be archived and revisited Less-intrusive data collection</i>

Until now, land-based MMS have primarily used a van or truck as the platform on which they are mounted. Such systems obtain accuracies that are suitable for all but the most demanding cadastral and engineering applications. However, this accuracy does not come cheaply. As a consequence of the platform and navigation and mapping technologies used, even an “inexpensive” system costs well over 200,000 USD. Because of their high cost, the market for such van-based MMS is rather small, and such systems are typically “one-off” systems that are operated by the companies or institutions that build them. In effect, this means that while several companies are making a profit using MMS, few are making a profit manufacturing them. Additionally, the van-based systems are extremely complex, and many smaller survey or mapping firms do not have the expertise required to operate them. Therefore, the benefits of mobile mapping – in particular the lower costs and greater efficiency of

data collection – are not being enjoyed by a wide community.

The goal of the research contained within this thesis is the development of a portable MMS that will overcome the drawbacks of current land-based MMS. The system will compete with current systems in terms of accuracy, but will be smaller, less costly, and less complex. The development of a portable mobile mapping system is a continuation of MMS research and development at The University of Calgary which has focused on airborne (Mostafa and Schwarz, 1999; Škaloud and Schwarz, 2000) and van-mounted MMS systems (El-Sheimy and Schwarz, 1996).

1.1 Overview of Mobile Mapping Systems

MMS integrate navigation sensors and algorithms together with sensors that can be used to determine the positions of points remotely. All of the sensors are rigidly mounted together on a platform; the former sensors determine the position and orientation of the platform, and the latter sensors determine the position of points external to the platform. The sensors that are used for the remote position determination are predominantly photographic sensors and thus they are typically referred to as imaging sensors (El-Sheimy, 1999). However, additional sensors such as laser rangefinders (Reed et al., 1996; Li et al., 1999) or laser scanners (Li et al., 2001) are also used in MMS and therefore the more general terms of mapping sensors (Li, 1997) or relative sensors (Novak, 1995) may also be used when referring to the remote sensors. In the following, imaging, mapping, relative and remote sensors are used interchangeably. As said above, the platform that carries the sensors is typically a van or a truck. However, the use of other platforms such as trains (Blaho and Toth,

1995; Sternberg et al., 2001) and even people (Barker-Benfield, 2000) has also been investigated and implemented.

The strength of MMS lies in their ability to directly georeference their mapping sensors. A mapping sensor is georeferenced when its position and orientation relative to a mapping co-ordinate frame is known. Once georeferenced, the mapping sensor can be used to determine the positions of points external to the platform in the same mapping co-ordinate frame. In the direct georeferencing done by MMS the navigation sensors on the platform are used to determine its position and orientation. This is fundamentally different from traditional indirect georeferencing where the position and orientation of the platform are determined using measurements made to control points. These control points are established through a field survey prior to data acquisition and their establishment is typically expensive and time-consuming. Also, for many terrestrial surveys, the establishment of sufficient control points is virtually impossible – for example, consider the control requirements to map an entire city using close-range photogrammetry. Finally, for some mapping sensors – such as laser-scanners or push-broom CCD arrays – it is difficult or impossible to establish control. The use of these sensors is not practical unless direct-georeferencing is performed.

In addition to the reduction in cost and time of field surveys, MMS also have other advantages over traditional methods of spatial data acquisition. These include:

- Both spatial and attribute information can be determined from the remotely sensed data
- Data can be archived and revisited – permitting additional data collection without additional field campaigns

- Increased coverage capability and more rapid turnaround time
- Easier implementation of automatic object recognition
- Reduced computational requirements to extract co-ordinates from remote sensors

It should be noted that MMS are not necessarily more accurate than traditional mapping techniques such as point-wise terrestrial surveys or aerial triangulation using large-format metric cameras. Also, several authors have questioned the exclusive use of direct georeferencing in aerial applications because of perceived problems with the reliability of the approach and difficulties with calibration of the integrated system (Grejner-Brzezinska et al., 1999). For airborne systems the general agreement is that the directly observed georeferencing parameters should be used in conjunction with indirect georeferencing. For land-based systems issues of reliability appear to have been much less scrutinised. This is likely because there are less systems operating, and also because the costs of performing a re-survey are significantly less.

1.2 History of Land-Based MMS

The first operational land-based MMS was developed by the Centre for Mapping at the Ohio State University. Their system – called GPSVanTM – integrated a code-only GPS receiver, two digital CCD cameras, two colour video cameras and several dead-reckoning sensors (Goad, 1991; Novak, 1991). All components were mounted on a van – the GPS provided the position of the van and the images from the CCD cameras were used to determine the positions of points relative to the van. The dead reckoning

sensors, which consisted of two gyroscopes and an odometer (wheel counter) on each of the front wheels, were primarily used to bridge GPS signal outages. These sensors were also used to provide orientation information for the exposure stations; however, there is little – if any – published information that examines the orientation accuracy of the GPSVan’s dead-reckoning sensors and the poor accuracy of similar sensors suggests that the orientation information they provided would have been of marginal quality at best. The two video cameras were used solely for archival purposes and to aid attribute identification – no relative positioning was performed from the video imagery. Using bundle-adjustment techniques with relative-orientation constraints, the GPSVan was able to achieve relative object space accuracies of approximately 10 cm. Unfortunately, because only carrier-smoothed code-differential GPS was used, absolute object-space accuracies were limited to 1-3 m.

GPSVan successfully illustrated how land-based multi-sensor systems could improve the efficiency of GIS and mapping data collection; however, the absolute accuracy of the object space points was too poor for many applications – especially when compared with competing technologies. Also, the dead reckoning sensors in the GPSVan were not very suitable for bridging GPS outages. Therefore, further developments of land-based mobile mapping system focused on improving system reliability and increasing absolute object space accuracies. The obvious technique for improving absolute accuracy was to use carrier-phase differential GPS, while the obvious choice for a more accurate dead-reckoning sensor was a high precision Inertial Measurement Unit (IMU). The use of an IMU has an additional advantage over other types of dead-reckoning sensors in that it also provides high-accuracy orientation information for the exposure stations. Further developments of land-based

MMS based on GPSVan or involving the same researchers – including NAVSYS GPS/Inertial Mapping system (GIM) and LambdaTechs GPSVision – all used IMUs as their dead-reckoning sensors (Coetsee et al., 1994; He et al., 1996). Later independent implementations of land-based MMS added dual-frequency carrier-phase differential GPS, more accurate IMUs, and more sophisticated processing techniques. Examples of some later systems include the VISATTM system (Schwarz et al., 1993), KiSSTM (Hock et al., 1995), and GI-EYETM (Brown, 1998). The VISAT system, in its final form, was notable because of the large number of imaging sensors it employed. Where previous land-based MMS were simple stereovision systems employing only two forward facing cameras, VISAT had eight cameras that enabled more flexible data collection and better imaging geometry. VISAT also had absolute object space accuracies that had previously been unattainable.

While published results from VISAT and other MMS demonstrate the operational viability of multi-sensor systems; the commercial viability of land-based MMS is evident in the number of successful “spin-off” companies. For example, GPSVanTM and its research spawned two companies: Transmap Corp. and Lambda Tech International (Lambda Tech, 2001; Transmap, 2001). Analytical Surveying, Inc. is also successfully operating the VISAT van.

In one important aspect land-based MMS have largely led their airborne counterparts. Namely, from their inception land-based MMS have used digital cameras as their remote sensors. This was possible because of the much smaller camera-to-object distances in land-based MMS when compared to airborne systems. The poor resolution of CCD chips meant that they could not be used in aerial applications without an unacceptable decline in accuracy. Indeed, the resolution of CCD chips

has only recently improved to the level that they can be used in airborne mapping systems (and even this is debatable). The use of digital cameras is advantageous because they eliminate the requirement to scan photographs. Consequently, they substantially reduce the period from raw data collection to extracted data dissemination. Digital sensors also simplify automatic point and feature extraction, and allow for more flexible data storage possibilities – for example, the images can be stored in Multi-Media GIS (Novak, 1993).

A list of some land-based MMS is presented in Table 2. Not considered in the table are systems that merely mount single or multiple navigation sensors on a moving platform. Such systems have the same limitation as traditional land-based surveying systems; viz., each point of interest must be occupied. Furthermore, such systems are also significantly less appropriate for GIS data collection because of the requirement to manually record attribute information. Also not included are systems that merely use GPS with a video camera exclusively for archival purposes. Such systems do not use the imagery for positioning purposes, and are consequently not mobile “mapping” systems.

Finally, it should be noted that writing literature reviews of mobile mapping systems has become something of an industry unto itself. Examples of such publications include Novak (1995), Li (1997), Tao (1998), El-Sheimy (1999), and Grejner-Brzezinska (2001). Indeed, most of the material for this chapter was taken from the author’s own review (see Ellum and El-Sheimy, 2002).

Table 1.2: Implementations of Land-Based Multi-Sensor Systems

Name	Developers	Platform	Navigation Sensors	Mapping Sensors	Reference(s)
GPSVan TM	Ohio State University	Van, Train	GPS, 2 gyros 2 odometers (wheel counter)	2 monochrome CCD digital cameras, 2 colour VHS cameras (for archival purposes)	Novak (1990) Goad (1991) Novak (1991)
VISAT TM	University of Calgary	Van	Dual frequency GPS, navigation-grade IMU	8 monochrome CCD digital cameras, 1 colour VHS camera (for archival purposes)	Schwarz et al. (1993) El-Sheimy and Schwarz (1996)
GIM TM	NAVSYS Corp.	Truck	GPS, low-cost IMU	1 CCD digital camera, 1 VHS camera	Coctsee et al. (1994)
KISS TM	University of the Federal Armed Forces Munich	Van	GPS, 3 ring-laser gyros odometer, barometer inclinometer, compass	2 monochrome CCD digital cameras, colour VHS camera (for archival purposes)	Hock et al. (1995) Sternberg et al. (2001)
TruckMAP TM	John E. Chance and Associates, Inc.	Van	Dual-antenna GPS, digital attitude sensor	Reflectorless laser range-finder	Reed et al. (1996)
Gator Communicator TM	University of Florida	Person	GPS, digital compass inclinometer	2 CCD digital cameras	Alexander (1996)
Indoor MMS	National Research Council, Canada	Mobile Robotic Platform	Wheel encoders	8 CCD digital cameras, bi- iris laser scanner (also used for navigation)	Barker-Benfield (2000) El-Hakim et al. (1997)
GI-EYE TM	NAVSYS Corp.	Any Land- Based Vehicle	GPS, low-cost IMU	1 CCD digital camera	Brown (1998)
CDSS	Geodetic Institute Aachen	Van	GPS, 2 odometers barometer	2 monochrome CCD digital cameras	Benning and Aussems (1998)
WUMMS	Wuhan Technical University	Truck	GPS, unspecified dead- reckoning sensor	CCD digital camera, laser range finder	Li et al. (1999)
GPSVision TM	Lamda Tech Int. Inc.	Van	GPS, navigation-grade IMU	2 colour CCD digital cameras	Lambda Tech (2001)
ON-SIGHT TM	Transmap Corp.	Van	GPS, navigation-grade IMU	Up to 5 digital CCD cameras	Transmap (2001)
MoSES	University of the Federal Armed Forces Munich	Van	GPS, navigation-grade IMU, odometer, barometer, inclinometer	2 CCD digital cameras (possible laser scanner and colour video camera)	Graefe et al. (2001)
Laser scanner MMS	Wuhan Technical University	Truck	GPS	CCD digital camera, laser scanner	Li et al. (2001)

1.3 Research Objectives

The primary objective of the thesis contained in this thesis is the development of a backpack mobile mapping system. The system will overcome the drawbacks of current mobile mapping systems – namely their high cost, large size, and complexity – which have restricted their widespread adoption in the survey and mapping industries. The development of such a system will satisfy the demand for a mobile mapping system that can compete in both cost and in user friendliness with current survey systems used for GIS data acquisition. The desired horizontal and vertical accuracies of the system are 0.2 metres (RMS) and 0.3 metres (RMS), respectively, at a camera-to-object distance of approximately 30 metres. These accuracies are comparable to accuracies available using some of the high-end terrestrial MMS. They are also similar to the accuracies from single-frequency GPS systems that are used to perform much of the data acquisition for GIS.

If the desired accuracies can be achieved, then the applications of a backpack mobile mapping system are numerous. They include pipeline right-of-way mapping, facility mapping, urban GIS data acquisition, highway inventory, architectural reconstruction and small-scale topographic mapping.

1.4 Thesis Outline

The research contained within this thesis is centred around photogrammetry. Thus, in Chapter 2, a review is given of fundamental photogrammetric principles. In particular, the extended collinearity equations – the basis of analytical close-range photogrammetry – are systematically derived. Chapter 3 continues with the focus on

photogrammetry. The concept of a self-calibrating bundle adjustment is introduced and the theory behind the inclusion of position and orientation observations into such adjustments is covered. Some notes are also given regarding the inclusion of relative orientations in the adjustment.

In Chapter 4, the focus switches to the Navigation sensors. A brief review is given of GPS, digital compasses, and inclinometers. The review is brief, reflecting the focus of the thesis on photogrammetry.

The practical implementation of the backpack MMS is detailed in Chapters 5 and 6. Chapter 5 describes the components and configuration of prototype system. The software developed for the system is also described. Chapter 6 contains the results from system calibration and testing. Both the object-space mapping accuracies and the accuracies of the navigation sensors are examined.

Finally, Chapter 7 contains the conclusions from this research. Suggestions for further investigations are also given.

Chapter 2

Close-Range Photogrammetry

Photogrammetry can be divided into several broad categories. Criteria for these categories include:

- Where the camera is mounted
- The type of camera
- The type of media that the images are recorded on
- The operational range (distance between the camera and the objects recorded in the images)
- The orientation of the camera
- How the data in the images is extracted

For example, if the technique to process the data is used as the criteria, then the categories are *analogue stereophotogrammetry* and *analytical photogrammetry*. In the former technique, co-ordinates of points are determined using pairs of images and

a stereoscopic viewing device, while in the latter technique co-ordinates are determined by mathematical computations using measurements made on the individual images (Thompson, 1980). This and other criteria are listed below in Table 2.1. The listing is by no means complete, as even the major categories described can be further subdivided. In addition, the terminology may differ. For example, terrestrial photogrammetry may be termed ground photogrammetry, and space photogrammetry may be termed satellite photogrammetry.

Table 2.1: Categories of Photogrammetry

Criteria	Type	Description
Where camera is mounted	<i>Terrestrial photogrammetry</i> <i>Aerial photogrammetry</i> <i>Space photogrammetry</i>	Camera is located on the ground Camera is mounted on an airplane or other aerial platform Camera is mounted on a space vehicle
Type of camera	<i>Metric photogrammetry</i> <i>Non-metric photogrammetry</i>	Camera used is specifically designed for high-precision photogrammetry and has a very stable interior geometry Camera is not designed for photogrammetry, and may have an unstable interior geometry
Type of recording media	<i>Film-based photogrammetry</i> <i>Digital photogrammetry</i>	Images are recorded on film Images are recorded by a digital camera (CCD chip)
Distance between the camera and the objects being recorded	<i>Close-range photogrammetry</i> <i>Long-range photogrammetry</i>	Small distance (<100m) Large distance (>100m, typically >1000m)
Orientation of the camera	<i>Vertical photogrammetry</i> <i>Oblique photogrammetry</i>	Optical axis is intentionally kept nearly vertical Optical axis is not vertical
Data extraction technique	<i>Analogue stereophotogrammetry</i> <i>Analytical photogrammetry</i>	Co-ordinates are extracted using pairs of images and a stereoscopic viewing device Co-ordinates are extracted using mathematical computations and measurements made on the individual images

In the backpack MMS, the camera is a low-cost digital camera that captures oblique images of features within 20-30m. Co-ordinates are then extracted from the images using a photogrammetric network least-squares adjustment. This type of photogrammetry can best be described as *non-metric terrestrial digital close-range oblique analytical photogrammetry*. However, such a descriptor, while complete, is obviously unwieldy. Fortunately, nearly all close-range photogrammetry performed today is all of terrestrial, digital, oblique and analytical. Furthermore, virtually all digital cameras are non-metric, and the former term almost always implies the latter. Thus, the photogrammetry used with the backpack MMS can simply be termed close-range photogrammetry.

This chapter reviews the fundamentals of close-range photogrammetry. Particular focus is given to the inclusion of the navigation data from the GPS and orientation sensor into the photogrammetric adjustment.

2.1 The Central Perspective Projection

The foundation of analytical photogrammetry is the central perspective projection (Wolf, 1983). In this model, shown in Figure 2.1, the camera is assumed to be an ideal pinhole camera with an infinitesimally small lens. This lens permits a single reflected ray of light from every visible point in object-space to pass, and an inverted image of object space is produced on a projection plane that is orthogonal to the optical axis of the camera.

The central perspective projection, which is the “physical” basis of photogrammetry, leads in turn to the mathematical basis of photogrammetry. The funda-

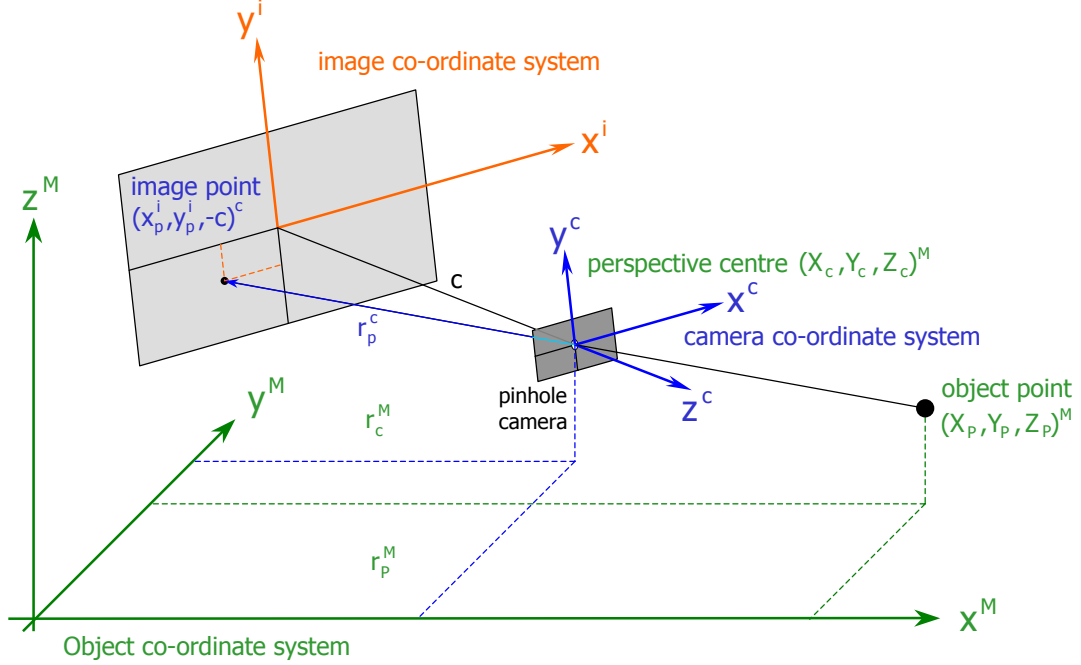


Figure 2.1: The Central Perspective Projection

mental equation in photogrammetry is a seven-parameter conformal transformation that relates camera co-ordinates of a point \mathbf{r}_p^c with its object (or *M*apping) space co-ordinates \mathbf{r}_P^M ,

$$\mathbf{r}_P^M = \mathbf{r}_c^M + \mu \mathbf{R}_c^M \mathbf{r}_p^c. \quad (2.1)$$

In Equation (2.1), \mathbf{r}_c^M is the position of the camera perspective center in the mapping frame and μ is the scale between the camera frame and the mapping frame for point *P*. \mathbf{R}_c^M is the rotation matrix between the camera co-ordinate frame and the mapping co-ordinate frame. In photogrammetry, the transpose of this matrix is normally formed using the angles κ , ϕ , and ω corresponding to a series of rotations

about the z, y, and x-axes, respectively. The angles are those required to rotate the object space axes to align with the camera axes. Explicitly, this is

$$\mathbf{R}_c^M = (\mathbf{R}_M^c)^T. \quad (2.2)$$

where

$$\mathbf{R}_M^c = \mathbf{R}_z(\kappa)\mathbf{R}_y(\phi)\mathbf{R}_x(\omega), \quad (2.3)$$

or,

$$\mathbf{R}_M^c = \begin{pmatrix} \cos(\kappa)\cos(\phi) & \sin(\kappa)\cos(\omega)+\cos(\kappa)\sin(\phi)\sin(\omega) & \sin(\kappa)\sin(\omega)-\cos(\kappa)\sin(\phi)\cos(\omega) \\ -\sin(\kappa)\cos(\phi) & \cos(\kappa)\cos(\omega)-\sin(\kappa)\sin(\phi)\sin(\omega) & \cos(\kappa)\sin(\omega)+\sin(\kappa)\sin(\phi)\cos(\omega) \\ \sin(\phi) & -\cos(\phi)\sin(\omega) & \cos(\phi)\cos(\omega) \end{pmatrix}. \quad (2.4)$$

By rearranging Equation (2.1), the reverse conformal transformation that relates object space co-ordinates with image co-ordinates is found to be

$$\mathbf{r}_p^c = \mu^{-1}\mathbf{R}_M^c (\mathbf{r}_P^M - \mathbf{r}_c^M). \quad (2.5)$$

Expressly, for the negative image depicted in Figure 2.1, this is

$$-\begin{pmatrix} x_p \\ y_p \\ -c \end{pmatrix}^c = \mu^{-1} \begin{pmatrix} r_{11} & r_{12} & r_{13} \\ r_{21} & r_{22} & r_{23} \\ r_{31} & r_{32} & r_{33} \end{pmatrix} \begin{pmatrix} X_P - X_c \\ Y_P - Y_c \\ Z_P - Z_c \end{pmatrix}^M, \quad (2.6)$$

where x_p and y_p are the image measurements of the point and c is the distance

– termed the *principal distance* – from the perspective centre of the camera to the projection plane. The terms r_{ij} ($i, j = 1, 2, 3$) are explicitly given in Equation (2.4). For convenience (and following convention) the superscripts denoting the coordinate frame have been dropped. Instead, co-ordinates in the camera system and co-ordinates in the mapping system are represented by lower-case and upper-case letters, respectively. The relation in Equation (2.5) can also be determined through inspection by examining Figure (2.1).

The third equation in (2.6) can be arranged so that

$$\mu^{-1} = \frac{c}{r_{31}(X_P - X_c) + r_{32}(Y_P - Y_c) + r_{33}(Z_P - Z_c)}. \quad (2.7)$$

When this is substituted into the first and second equations of (2.6), the result is

$$x_p = -c \frac{r_{11}(X_P - X_c) + r_{12}(Y_P - Y_c) + r_{13}(Z_P - Z_c)}{r_{31}(X_P - X_c) + r_{32}(Y_P - Y_c) + r_{33}(Z_P - Z_c)} \quad (2.8a)$$

$$y_p = -c \frac{r_{21}(X_P - X_c) + r_{22}(Y_P - Y_c) + r_{23}(Z_P - Z_c)}{r_{31}(X_P - X_c) + r_{32}(Y_P - Y_c) + r_{33}(Z_P - Z_c)}. \quad (2.8b)$$

These observation equations are perhaps the most powerful equations used in photogrammetry. They are termed the *collinearity equations* because the central perspective projection model from which they are derived assumes that each object space point, the corresponding image point, and the perspective center of the camera are collinear.

The collinearity equations are frequently simplified to

$$x_p = -c \frac{x_{c/p}}{z_{c/p}} \quad (2.9a)$$

$$y_p = -c \frac{y_{c/p}}{z_{c/p}}. \quad (2.9b)$$

where

$$\begin{pmatrix} x_{c/p} \\ y_{c/p} \\ z_{c/p} \end{pmatrix}^c = \mathbf{R}_M^c \begin{pmatrix} X_P - X_c \\ Y_P - Y_c \\ Z_P - Z_c \end{pmatrix}^M. \quad (2.10)$$

Again, the lower case letters indicate co-ordinates in the camera co-ordinate frame, and upper-case letters indicate co-ordinates in the mapping co-ordinate frame. The relationship in Equation (2.8) could also be directly deduced using similar triangles.

Both the image and camera axes may be defined differently than in the above derivation. Additionally, it is usually desirable to use positive images to make the image point measurements. Both changes are easily accomodated by modifying the \mathbf{r}_p^c term in Equation (2.5) and deriving new collinearity equations. As an example, consider the positive digital image depicted in Figure 2.2. In this case,

$$\mathbf{r}_p^c = \begin{pmatrix} -x_p^i & -y_p^i & c \end{pmatrix}^T \quad (2.11)$$

However,

$$\mathbf{r}_p^c = \begin{pmatrix} -x_p^i & -y_p^i & c \end{pmatrix}^T = - \begin{pmatrix} x_p^i & y_p^i & -c \end{pmatrix}^T, \quad (2.12)$$

which is equivalent to Equation (2.6). Consequently, the collinearity equations do not change. This is one advantage of deriving the collinearity equations in this manner – they are suitable for both regular negative images and positive digital images. It

should be noted that the definition of camera axes presented above differs from the definition commonly used in aerial photography where the positive 'z' axis is directed back from the perspective centre of the camera.

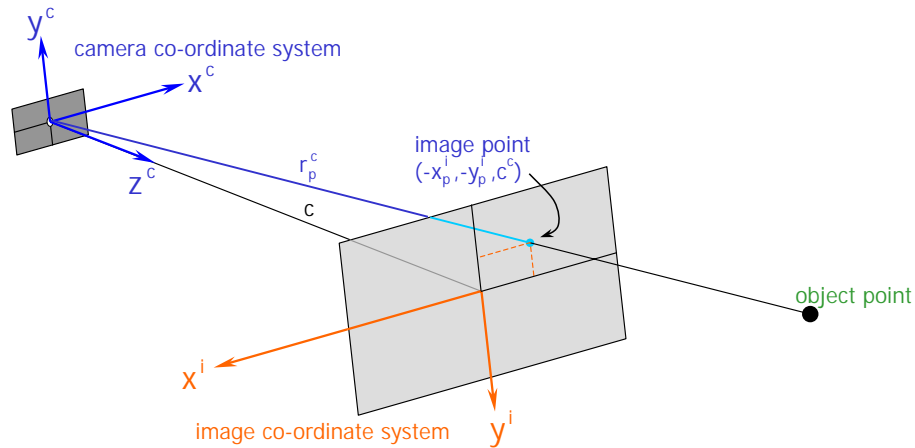


Figure 2.2: Positive Digital Image

The central perspective projection is, unfortunately, an idealisation. In reality, an imaging system that uses a pinhole camera is not feasible as the single rays of light reflected from objects would take an impossibly long period to expose the film or CCD chip. Thus, in a real camera the pinhole lens is replaced by a compound lens system. Also, imperfections in manufacturing result in the projection plane neither being perfectly orthogonal to the optical axis nor perfectly flat. Obviously, these and other departures from the ideal physical model cause departures from the ideal mathematical model. Fortunately, many of these departures can be modelled, and their parameters determined through calibration.

2.2 Geometric Camera Calibration

Camera calibration can be divided into two categories: geometric and radiometric. Geometric calibration attempts to model systematic geometric or physical deviations that affect the positions of image points on the film or CCD array. In other words, the departures from the ideal physical model that were introduced above. In contrast, radiometric calibration attempts to ascertain how accurately the grey values in the recorded image reflect the true reflectance values of features in the image. Of the two calibration categories, geometric calibration is by far the more significant to photogrammetrists. This is because geometric errors will virtually always affect the co-ordinates of object-space points derived from the images, while radiometric errors are much less likely to do the same. For this reason radiometric calibration will not be considered further, and the focus of the following will be on geometric calibration.

Geometric camera calibration has two goals. The first is that mentioned above – the determination of deviations from the ideal central perspective model. More specifically, the calibration determines the parameters of models that describe distortions caused by the camera’s compound lens system. The second goal of geometric calibration is the determination of a camera’s focal length and principal point offsets. Knowledge of both is required to fully determine the \mathbf{r}_p^c term in Equation (2.5). In particular, the focal length is the z component of that vector, and the principal point is required to determine the x and y components. Collectively, the lens distortions parameters, the focal length and the principal point offsets are known as the interior or inner orientation of a camera (some authors only refer to the latter two parameters sets when speaking of interior orientation – cf. Cooper and Robson (1996)).

2.2.1 Focal Length

Figure 2.3 shows a simple 4-element compound lens system. A ray of light that arrives at angle i with the optical axis will enter the lens system, be refracted by the lenses, and exit at a different angle e . Because the incident and emergent angles are not the same, the system obviously differs from the ideal central perspective model. However, the compound lens system can be treated as an ideal central perspective model by defining two “pseudo” perspective centres termed the front (or incident) and rear (or emergent) nodal points. These points, shown as N and N' respectively on Figure 2.3, are defined such that a ray of light directed at the front nodal point will appear to emerge from the rear nodal point at the same angle as it was incident (Moffit, 1967). If the incident light rays come from an object at an infinite distance from the camera, then they will arrive parallel to each other. The corresponding emergent light rays will come to focus at the *plane of infinite focus*. The distance between the rear nodal point and the plane of infinite focus is defined as the focal length of the camera, and can be treated equivalent to the focal length of a pinhole camera. If the image distance of the camera (distance from the rear nodal point to the image plane) is set equal to the focal length, then the camera is said to be focused at infinity.

The parameters of radial lens distortion and the focal length of a camera are inherently related. A change in one will effect a change in the other and vice versa. This property gives rise to an alternative definition of the focal length that is known as the *calibrated focal length*. The calibrated focal length, which can also be referred to as the *camera constant* or Gaussian focal length, can be defined in several different ways. It can either be the focal length that results in an overall mean distribution

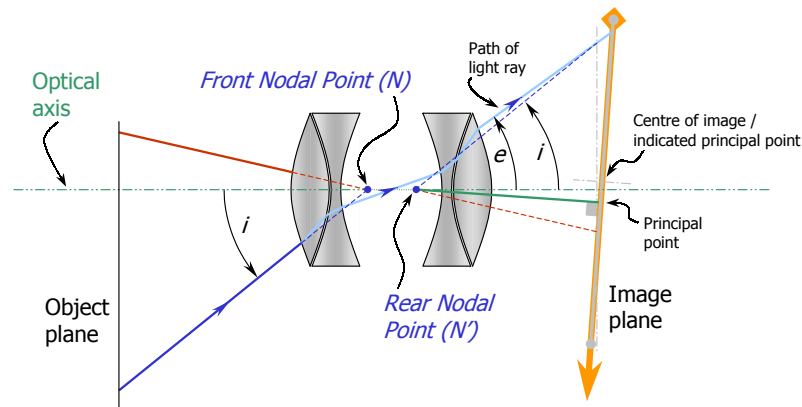


Figure 2.3: Focal Length

of the radial distortion (Wolf, 1983), equalizes the maximum positive and negative distortions (Moffit, 1967), or provides some other preferred balancing of the radial distortion curve (Livingston, 1980).

An additional value that is related to – and sometimes confused with – the focal length is the *principal distance*. The relationship between principal distance and focal length is shown in Figure 2.4. From this figure it can be seen that the principal distance is equal to the focal length scaled for any enlargement or reduction in the print that image measurements are made from, or scaled for any change in the location of the image plane from the plane of infinite focus. It follows that two conditions must be satisfied for the principal distance and focal length to be equivalent. First, the camera must be focused at infinity (Fryer, 1992). Second, the image must not be enlarged or reduced. In digital photogrammetry, the latter condition can be effectively satisfied by using pixels as units for both the image measurements and the focal length. If this is done, then – providing the first condition is met – the principal distance and focal length will be the same.

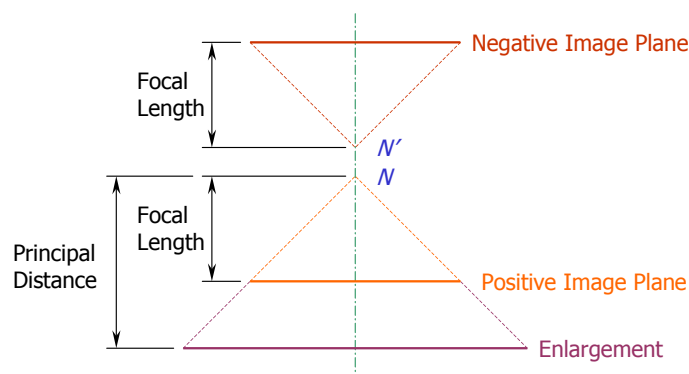


Figure 2.4: Principal Distance (after Moffit (1967))

2.2.2 Principal Point Offsets

In their simplest interpretation, the principal point offsets are the translations required to convert co-ordinates measured in the image co-ordinate system to the corresponding co-ordinates in the camera co-ordinate system. Expressely this is

$$x_p^c = x_p^i - x_o \quad (2.13a)$$

$$y_p^c = x_p^i - y_o, \quad (2.13b)$$

where the superscripts c and i indicate the camera and image co-ordinates, respectively, and x_o and y_o are the co-ordinates of the principal point.

For less precise applications it is possible to use the center of the image as the principal point. In this case, the principal point is known as the *indicated principal point*, fiducial centre, or centre of collimation (Livingston, 1980; Wolf, 1983; Fryer, 1996). In film-based photogrammetry both the center of the image and the origin of the image co-ordinate system are considered to lie coincident with the normal from the origin of the camera co-ordinate system. As a result the indicated principal

point offsets are zero. In digital photogrammetry, however, the origin of the image coordinate system is normally in a corner of the image and consequently the indicated principal point offsets are equal to half of the image dimensions.

Use of the indicated principal point is only suitable for low-precision applications. For more precise photogrammetry several other principal points are defined and used. The definition of the “true” principal point is the base of the perpendicular that connects the image plane to the perspective center (or more correctly to the rear nodal point) of the camera. This point differs from the indicated principal point because the centre of the lens system cannot be perfectly aligned with the centre of image. Unfortunately, imperfections in the alignment of the individual lenses means that the true principal point cannot exist. However, it is possible to determine the *principal point of autocollimation*, which is the point at which a ray of light normal to the image plane and coming from infinity intersects the image plane (Moffit, 1967). This point is normally determined using a collimator; hence its name. It is also possible to refer to the *principal point of best symmetry*. In this definition, the point is that around which the other lens distortions have the best symmetry or asymmetry. For most cameras, this point is effectively the point at which the optical axis intersects the image plane. The principal point of best symmetry is also called the *calibrated principal point*. This terminology, however, is misleading, as two of the calibration techniques – autocollimation and self-calibration – do not yield this point (for an explanation of this, see Burner, 1995). For most applications, including close-range photogrammetry, the principal point of autocollimation and the principal point of best symmetry are close enough to be considered the same. For more precise applications some authors advocate using the principal point to translate the image

points from image space to camera space, and the principal point of best symmetry to compute lens distortion (Burner, 1995). In practice, however, this is rarely, if ever, done.

Several definitions of the principal point are shown below in Figure 2.5. Also shown is a typical digital image co-ordinate system. For more details on the principal point, consult Clarke et al. (1998)

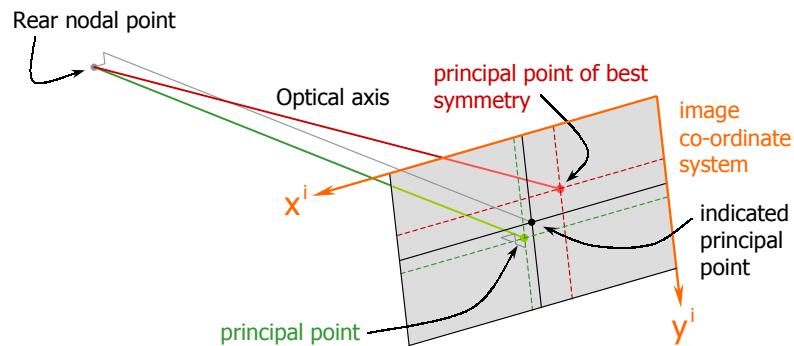


Figure 2.5: Principal Point Offsets for a Digital Image

2.2.3 Lens Distortion Parameters

When performing a camera calibration for lens distortions the goal is to determine the parameters of mathematical models that describe the errors caused by the distortions. The models can be divided into two categories: physical models and polynomial models. Physical models attempt to describe the actual deviations from an ideal model that light rays undergo as they pass through lenses of a camera. In contrast, polynomial models make almost no concession to reality. Instead, they are designed so that their parameters are as uncorrelated as possible. In photogrammetry the emphasis is nearly universally on physical models, as it is generally acknowledged

that such models provide superior accuracy to polynomial models (Murai et al., 1984; Faig and Shih, 1988). Consequently only the former will be considered here.

The two major types of lens distortions that photogrammetrists attempt to model are decentring distortion and symmetric radial distortion. Both, in reverse order, are described below. Most authors consider lens distortion to be a type of (Seidel) lens aberration, although some categorise it separately (see, for example, Wolf, 1983).

Symmetric Radial Lens Distortion: As its name suggests, radial lens distortion causes radial errors in the image point measurements. There are both symmetric and asymmetric radial distortions, although the magnitude of the former is typically much greater than that of the latter, and consequently the term “radial lens distortion” usually refers only to the symmetric distortions. Both types of radial distortion are the result of imperfections in the grinding of the camera lenses. Symmetric lens distortion, in particular, results from radially symmetric imperfections. These imperfections cause variations in lateral magnification with radial distance.

Symmetric radial distortion can change in both sign and magnitude depending on the radial distance from the centre of the image. Positive radial distortion, which is often termed pincushion distortion, causes points to be located closer to the centre of the image than they otherwise would be. Conversely, negative distortion, normally termed barrel distortion, causes points to be imaged farther from the centre. Both types of distortion are shown in Figure 2.6.

The model used to represent and correct for radial distortion is an odd-powered polynomial function of the radial distance:

$$\delta r = k_0 r + k_1 r^3 + k_2 r^5 + k_3 r^7 + \dots \quad (2.14)$$

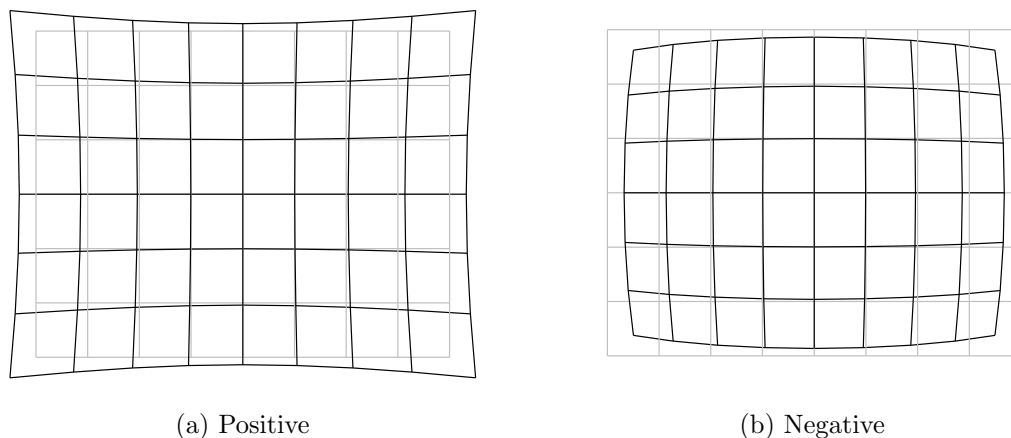


Figure 2.6: Symmetric Radial Distortion

In Equation (2.14), δr is the error resulting from the radial distortion, the k_i terms are the coefficients of radial distortion, and r is the radial distance from the principal point of best symmetry. The latter is given by

$$r = \sqrt{\bar{x}^2 + \bar{y}^2}, \quad (2.15)$$

where \bar{x} and \bar{y} are the distances from the principal point of best symmetry, calculated as $\bar{x} = x - x_{pps}$ and $\bar{y} = y - y_{pps}$, respectively.

Once the total radial error has been calculated the x and y image co-ordinates can be corrected for it using

$$\delta x_r = \frac{\bar{x}\delta r}{r} \quad (2.16a)$$

$$\delta y_r = \frac{\bar{y}\delta r}{r}. \quad (2.16b)$$

It is also possible to store values of radial distortion at discrete radial distances

in a lookup table, and to determine corrections by table lookup and interpolation (Mikhail et al., 2001). However, Equations (2.14) and (2.16) require minimal computation, and any speed gain from using a lookup table is negligible.

It is easily shown that the error resulting from the linear scale term k_0r can be equivalently modelled by a change in principal distance. Consequently the k_0r term is usually not included when calculating the radial distortion error and the principal distance is changed to compensate for its omission. The k_2 and higher terms are also commonly omitted, as the k_1 term alone will normally be sufficient for all but the highest accuracy applications. The radial distortion at a specific principal distance is termed Gaussian distortion (Fraser, 1997).

The radial distortion can be plotted as a function of radial distance. When this is done, the resulting plot is termed a radial distortion curve or profile. The radial distortion profile corresponding to a specific principal distance is termed the Gaussian distortion profile.

Decentring Distortion: Decentring distortion is caused by the misalignment of the axes of the individual lenses of a camera along a common axis, and by the misalignment of the normal from the image plane with the camera's optical axis. Since its primary influence is not the quality of the lenses, it is not, strictly speaking, a "lens" distortion. However, it is normally categorised as such, and hence its inclusion in this section.

The model that is universally accepted for describing and correcting decentring distortions is that formulated by Brown (1966). When higher order terms are ignored,

the correction equations due to this model are

$$\delta x_d = p_1(r^2 + 2\bar{x}^2) + 2p_2\bar{x}\bar{y} \quad (2.17a)$$

$$\delta y_d = p_2(r^2 + 2\bar{y}^2) + 2p_1\bar{x}\bar{y}, \quad (2.17b)$$

where p_1 and p_2 are the coefficients of decentring distortion, and r , \bar{x} , and \bar{y} are as were given previously. This model is often referred to as the Conrady-Brown model.

Decentring distortion is often mistakenly called tangential distortion (see, for instance, Cooper and Robson, 1996). However, it actually has both tangential and asymmetric radial effects. The maximum magnitudes of both can be determined using the profile function, which is approximated by

$$p(r) = (p_1^2 + p_2^2)^{\frac{1}{2}} r^2. \quad (2.18)$$

The maximum tangential effect is then given by this function, while the maximum radial effect is three times as large, or $3p(r)$. Both effects can be seen in Figure 2.7.

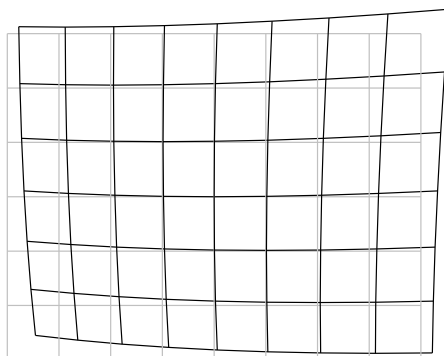


Figure 2.7: Decentring Distortion

It is often stated that the decentring distortion coefficients are highly correlated with the principal point offsets, and that a change in one can, to a large degree, be compensated for by a change in the other (Fryer, 1992; Fraser, 1997). It has also been stated that the decentring distortion terms are able to account for large misalignments of the lense system with the image plane (Burner, 1995). However, it was shown in Clarke et al. (1998) that it is the rotational parameters of the exterior orientation that are most highly correlated with the principal point offsets, and that shifts in the principal point are best compensated for by changes in the camera's orientation. The residual error that remains from this correlation can be further reduced by using the decentring distortion model, and it is this reduction that makes the decentring coefficients and principal point appear so highly correlated.

Finally, it should be noted that for most cameras, the effects of decentring distortion are much less than those for radial distortion and are often disregarded (Wolf, 1983; Mikhail et al., 2001).

2.2.4 Additional Parameters

In addition to decentring distortion and symmetric radial lens distortion, photogrammetrists often try to model additional departures from the ideal central perspective projection. The parameters of these models are termed additional parameters. These parameters and the models that use them are not required for most applications, including the medium accuracy photogrammetry used in the backpack mobile mapping system. However, for completeness they are briefly described below.

In-Plane Distortion: In-plane distortion refers to deformation effects in the plane of the image. In digital photogrammetry, the geometric integrity of the CCD chips is generally very high, and consequently true in-plane distortions are minimal (Shortis and Beyer, 1996; Fraser, 1997). Despite this, apparent in-plane distortions can occur in the process of capturing an image. At the University of Calgary, one effect – a differential scale between the horizontal and vertical axes – has been handled by adding a term that describes the scaling (or affinity) between axes (Lichti, 1996). It is also possible to add an additional term that describes the non-orthogonality (or shear) between axes (Fraser et al., 1995; Patias and Streilein, 1996).

The correction for affinity and shear needs to be applied to either the ordinates or abscissae of the image co-ordinates, but not both. For the latter case, the correction equation is

$$\delta x_f = b_1 \bar{x} + b_2 \bar{y}, \quad (2.19)$$

where δx_f is the in-plane distortion correction that must be applied to the x image co-ordinate, and b_1 & b_2 are the affinity and shear terms, respectively. A similar correction could alternatively be applied to the y co-ordinate.

Out-of-Plane Distortion: Out-of-plane distortion is a synonym for image plane unflatness. Deformations of the image plane that are radial in nature will partially be compensated by the radial lens distortion model (Fraser et al., 1995). The remaining effects can be modelled using low-order polynomials. Unfortunately, the recovery of such parameters using self-calibration techniques, as was done by Fraser et al. (1995), has not proven very successful.

Lens Distortion Variation: Radial lens distortion varies according to the distance from the camera to the object. This variation of distortion within the photographic field means that for a camera held at a fixed focus the radial distortion is different for points at different distances from the camera. This is true even if the points are at the same radial distance on the image from the principal point, and even if the camera is focused at infinity. Fortunately, the variation is small, and need only be compensated for in very close-range applications that require the highest accuracies. A larger variation of lens distortion occurs with a change in focus. This effect, however, is also generally ignored as cameras used in photogrammetry are typically held at a fixed focus. Fraser and Shortis (1992) and Shortis et al. (1998) provide good descriptions of both the variation of distortion within the photographic field and variation with focusing. The same papers also provide a method to correct for the effects. These formulas are based in part on work in Brown (1971) and Fryer and Brown (1986), which were in turn based on Magill (1955).

2.2.5 Calibration Techniques

In close-range digital photogrammetry, the technique almost always used for camera calibration is *self-calibration*. In this technique, the interior orientation parameters are included in a photogrammetric network adjustment as unknown parameters. These parameters are then solved for together with the other unknown parameters such as the camera's position and attitude. The self-calibration technique is popular because it requires neither specialised equipment nor specialised operators, and because it can be done quickly and repeatedly. More details about the approach are given in the following chapter, which deals with the adjustment of photogrammetric

networks.

Other methods of calibration do, of course, exist, and are occasionally used to calibrate cameras used in photogrammetry. These techniques, and details about them, are listed in Table 2.2. It should be noted that many of the elements of interior orientation, such as the focal length and the principal point of best symmetry, are abstractions that cannot be measured directly. Such parameters are determined indirectly using other measurements made during a camera calibration.

Table 2.2: Camera Calibration Methods

Method (Reference)	Description
Multicollimator (Wolf, 1983)	<i>Two orthogonal angular arrays of collimators project crosses through the lens of the camera. The calibration parameters are determined by comparing the resulting positions of the imaged crosses with their expected positions.</i>
Goniometer (Moffit and Mikhail, 1980)	<i>An illuminated grid is placed in the focal plane of the camera. A telescope on the opposite side of the lens is aligned (by autocollimation) with the camera's principal point of autocollimation (PPA). The angles between the grid marks and the PPA are then measured and compared with their expected values, and the calibration parameters determined from the differences.</i>
Stellar (Wolf, 1983)	<i>Stars with known position are imaged by the camera, and the calibration parameters calculated using the differences between the measured image positions of the stars and their expected positions (similar to the multicollimator method).</i>
Plumb-Line (Brown, 1971)	<i>Images of straight (and not necessarily plumb) lines in object space are captured by the camera. The calibration parameters are determined using the departures from linearity observed in the imaged lines (only the radial lens and dencentrig distortion can be recovered).</i>

2.3 Extended Collinearity Equations

The collinearity equations presented in Section 2.1 are for the ideal central perspective projection and the corresponding ideal pinhole camera. They are not suitable for use with measurements taken from images produced by the non-ideal cameras used in practice. However, once the parameters of interior orientation are known, the collinearity equations can be modified so that they can be used with images taken by “real” cameras. This modification, often termed image co-ordinate refinement, involves translating the observed image co-ordinates into the camera co-ordinate frame and correcting them for lens distortion and other departures from the ideal central perspective projection. Expressly, this is

$$x_p^c = x_p^i - x_o + \delta x \quad (2.20a)$$

$$y_p^c = y_p^i - y_o + \delta y, \quad (2.20b)$$

where x_p^c and y_p^c are the co-ordinates in the camera co-ordinate frame, x_p^i and y_p^i are the observed image co-ordinates, and δx and δy are the corrections for distortion and other effects. Using Equations (2.14), (2.16), (2.17) and (2.19), the correction terms can be expressed as

$$\begin{aligned} \delta x = \bar{x}r^2 [k_1 + r^2(k_2 + r^2k_3)] + p_1(r^2 + 2\bar{x}^2) + 2p_2\bar{x}\bar{y} \\ + b_1\bar{x} + b_2\bar{y} \end{aligned} \quad (2.21a)$$

$$\delta y = \bar{y}r^2 [k_1 + r^2(k_2 + r^2k_3)] + p_2(r^2 + 2\bar{y}^2) + 2p_1\bar{x}\bar{y}. \quad (2.21b)$$

Apart from the radial lens distortion terms, which have been re-arranged to reduce the number of computations, these expressions are the same as those in Fraser et al. (1995).

When Equation (2.20) is substituted into the standard collinearity equations given in Section 2.1, the result is

$$x_p = x_o - \delta x - c \frac{x_{c/p}}{z_{c/p}} \quad (2.22a)$$

$$y_p = y_o - \delta y - c \frac{y_{c/p}}{z_{c/p}}. \quad (2.22b)$$

These modified collinearity equations are known as the extended collinearity equations. They are the basis behind a self-calibrating bundle adjustment – the topic of the next chapter.

Chapter 3

Adjustment of Photogrammetric Networks

In photogrammetry, the process of determining object space co-ordinates from image point measurements is termed *triangulation*. Traditionally, this process had three distinct stages: first, image co-ordinates were corrected for systematic departures from the ideal central perspective model; second, a stereo-model was created using two overlapping images; and third, the stereo-model was transformed into an absolute co-ordinate frame. These three steps were known as *image refinement*, *relative orientation*, and *absolute orientation* respectively. A more accurate alternative to performing the steps independently is to implicitly combine them into a *bundle adjustment*. In this technique, all information – including image point measurements, parameter observations, and constraints between parameters – is input into a single least squares adjustment. The adjustment optimally combines the data and gives the most accurate estimates of the unknown parameters. The bundle adjustment,

known also as a simultaneous multiframe analytical calibration, is used almost universally in close-range photogrammetry for performing triangulation. In addition, it is also the most favoured technique for performing camera calibrations.

In this chapter, the bundle adjustment is introduced and briefly reviewed. Then, the inclusion of position and orientation measurements into the adjustment are discussed. Finally, some notes are made regarding relative orientations, inner constraints, and datum definition.

3.1 Bundle Adjustment

As stated above, triangulation in close-range photogrammetry is almost exclusively done using the bundle adjustment technique. No other method is able to match both the accuracy and flexibility of a bundle adjustment. In addition, no other method is as elegant or as rigorous.

The key concepts behind a bundle adjustment can be deduced from its title: “bundle” refers to the bundle of image rays emanating from the perspective centre of a camera, and “adjustment” refers to the technique of least squares that is used to estimate the unknown parameters. Putting both concepts together results in a simple, but complete, definition of what a bundle adjustment does – it uses least squares to adjust the bundles of image rays coming from each camera so as to arrive at the best possible estimate of the unknown parameters. An image ray, in this context, is the light ray that connects a point in object space, the perspective centre of a camera, and a point in an image. As detailed in Chapter 2, the equations that relate these three points are the collinearity equations, and it is from these equations

that the derivation of the bundle adjustment begins.

The extended collinearity equations were introduced in Section 2.3. In expanded form, these equations are

$$x_p = x_o - \delta x - c \frac{r_{11}(X_P - X_c) + r_{12}(Y_P - Y_c) + r_{13}(Z_P - Z_c)}{r_{31}(X_P - X_c) + r_{32}(Y_P - Y_c) + r_{33}(Z_P - Z_c)} \quad (3.1a)$$

$$y_p = y_o - \delta y - c \frac{r_{21}(X_P - X_c) + r_{22}(Y_P - Y_c) + r_{23}(Z_P - Z_c)}{r_{31}(X_P - X_c) + r_{32}(Y_P - Y_c) + r_{33}(Z_P - Z_c)}. \quad (3.1b)$$

These equations can be expressed in matrix form as

$$\mathbf{l} = \mathbf{f}(\mathbf{x}), \quad (3.2)$$

where \mathbf{l} is the vector of image point observations and \mathbf{x} is the vector of unknown parameters. Linearising Equation (3.2) using a first-order Taylor series expansion yields

$$\mathbf{l} + \mathbf{v} = \mathbf{f}(\mathbf{x}^0) + \mathbf{A}\boldsymbol{\delta}, \quad (3.3)$$

where $\mathbf{f}(\mathbf{x}^0)$ is the value of the collinearity equations evaluated at the point of linearisation, \mathbf{A} is the Jacobian of the same equations with respect to the parameters, and $\boldsymbol{\delta}$ is the vector of unknown differences between the estimated parameter values and their values at the point of linearisation. The \mathbf{v} term represents corrections, known as the *residuals*, that must be made to the measurements so that the functional model can be exactly satisfied (Cooper and Robson, 1996). The parameter values at the point of linearisation are known as the initial approximates of the adjustment.

Equation (3.3) is typically simplified to

$$\mathbf{v} = \mathbf{A}\boldsymbol{\delta} + \mathbf{w}, \quad (3.4)$$

where \mathbf{w} , which is known as the misclosure vector, is equal to $\mathbf{f}(\mathbf{x}^0) - \mathbf{l}$.

A least squares adjustment solves the system of equations in (3.3) subject to the condition that the sum of the squares of the weighted residuals is a minimum. This condition can be expressed as

$$\mathbf{v}^T \mathbf{P} \mathbf{v} \rightarrow \text{minimum}, \quad (3.5)$$

where \mathbf{P} is the weight matrix of the observations, which is simply the inverse of the covariance matrix of the observations \mathbf{C}_l , or

$$\mathbf{P} = \mathbf{C}_l^{-1}, \quad (3.6)$$

To be entirely accurate, the weight matrix is only the inverse of the covariance matrix when the *a priori variance factor* is unity; however, for the sake of convenience this distinction will be ignored.

The least squares solution to Equation (3.3) is found by solving the corresponding system of equations given by

$$(\mathbf{A}^T \mathbf{P} \mathbf{A}) \boldsymbol{\delta} = -\mathbf{A}^T \mathbf{P} \mathbf{w} \quad (3.7)$$

or

$$\mathbf{N}\boldsymbol{\delta} = -\mathbf{u}. \quad (3.8)$$

The coefficient matrix \mathbf{N} in Equation (3.8) is known as the *normal matrix*, and the \mathbf{u} vector is known as the normal vector or *vector of constant terms*. If the design matrix has full-rank then the normal matrix is both symmetric and positive definite. Consequently, $\boldsymbol{\delta}$ can be solved for by Cholesky decomposition and back-substitution (Press et al., 1992). The $\boldsymbol{\delta}$ correction terms are then added to the current estimates of the parameters, and the process is repeated – or iterated – until all the correction terms are below some threshold, at which point the adjustment is said to have converged. It should be noted that at no time during the iteration process is it necessary to invert the normal matrix. A full inversion, which is much more computationally expensive than simply solving the system of equations, is only necessary to compute the covariance of the estimated parameters at the end of the adjustment.

A side-effect of the least-squares method is that the sum of the residuals from an adjustment is zero. This, in turn, means that the mean of the residuals is zero, which is equivalent to saying that the least-squares estimates are unbiased. It should be noted, however, that the derivation of least-squares does not make explicit use of this property.

In the least squares developed above, the parameters are treated as being entirely unknown. However, it is often the case that some or all of the parameters are known, but not known exactly. In other words, existing estimates of the parameters are available, but these estimates have some uncertainty in them. Parameters such as

these can be included in the adjustment using *unified least squares* in conjunction with *parameter observations* (Mikhail, 1976). A parameter observation relates an adjustment's current estimate of a parameter with its known (but uncertain) value using equations of the form

$$\hat{\mathbf{x}} = \mathbf{x}^o; \quad \mathbf{C}_{x^o}. \quad (3.9)$$

In Equation (3.9), $\hat{\mathbf{x}}$ indicates the adjustment's current estimate of the parameter, \mathbf{x}^o is the parameter's observed value, and \mathbf{C}_x is the parameter observation's covariance. The parameter observations are added to the system of normal equations using

$$(\mathbf{N} + \mathbf{P}^o) \boldsymbol{\delta} = -(\mathbf{u} + \mathbf{P}^o \mathbf{w}^o), \quad (3.10)$$

where \mathbf{P}^o is the parameter observation's weight, which is the inverse of its covariance, and \mathbf{w}^o is the misclosure of the parameter observation, which is equal to $\hat{\mathbf{x}} - \mathbf{x}^o$.

An observed parameter lies somewhere in-between a constant and an unknown. Just where in-between is a function of the parameter observation's weight. A high weight means that a parameter will not be allowed to vary in the adjustment too much from its input value – i.e., it will be close to a constant. Conversely, a low weight means that a parameter will have more freedom to be adjusted – i.e., it will be close to an unknown.

The unknown parameters in a basic bundle adjustment are the positions and orientations of the cameras, and the co-ordinates of the object space points. However, it is also possible to include the parameters of interior orientation as unknown quantities. When this is done, the adjustment is known as a *self-calibrating bundle*

adjustment. In effect, the adjustment calibrates the camera(s) while simultaneously solving for the other unknown parameters. This is powerful extension to a normal adjustment, because it means that it is not necessary to use metric cameras with stable and precisely calibrated interior orientations. Instead, non-metric cameras can be used, and their interior orientations determined “on-the-job”. Care must be taken, however, with parameter correlations in the adjustment. Many of the correlations that exist between the elements of interior orientation were discussed in Chapter 2. Additional correlations also exist between the interior and exterior orientations of the camera. For example, the focal length is highly correlated with the camera’s position. Fortunately, much of the correlation that exists between parameters can be reduced or even eliminated with the judicious application of parameter observations, and by careful arrangement of the imaging geometry. For example, convergent imagery will decorrelate the focal length from the camera position, and rotating the camera along its optical axis will reduce the correlation between the principal point offsets and rotational parameters of exterior orientation.

Both the normal matrix and vector of constant terms can be subdivided into smaller units that correspond to specific parameter sets. In photogrammetry, the parameters are normally grouped into three categories: the unknown object space co-ordinates, the exterior orientations of the cameras, and the interior orientations of the cameras. If these parameter sets are indicated by the subscripts 1, 2, and 3,

respectively, then the normal equations can be expressed as

$$\begin{pmatrix} \mathbf{A}_1^T \mathbf{P} \mathbf{A}_1 + \mathbf{P}_1^o & \mathbf{A}_1^T \mathbf{P} \mathbf{A}_2 & \mathbf{A}_1^T \mathbf{P} \mathbf{A}_3 \\ \mathbf{A}_2^T \mathbf{P} \mathbf{A}_1 & \mathbf{A}_2^T \mathbf{P} \mathbf{A}_2 + \mathbf{P}_2^o & \mathbf{A}_2^T \mathbf{P} \mathbf{A}_3 \\ \mathbf{A}_3^T \mathbf{P} \mathbf{A}_1 & \mathbf{A}_3^T \mathbf{P} \mathbf{A}_2 & \mathbf{A}_3^T \mathbf{P} \mathbf{A}_3 + \mathbf{P}_3^o \end{pmatrix} \begin{pmatrix} \delta_1 \\ \delta_2 \\ \delta_3 \end{pmatrix} = - \begin{pmatrix} \mathbf{A}_1^T \mathbf{P} \mathbf{A}_1 + \mathbf{w}_1^o \\ \mathbf{A}_2^T \mathbf{P} \mathbf{A}_2 + \mathbf{w}_2^o \\ \mathbf{A}_3^T \mathbf{P} \mathbf{A}_3 + \mathbf{w}_3^o \end{pmatrix}. \quad (3.11)$$

Careful ordering of the parameters in the manner above enables special techniques to be used to solve the system of normal equations.

3.2 Inclusion of GPS Positions

Part of the attractiveness of the bundle adjustment is the ease with which additional non-photogrammetric observations can be included into the adjustment. In mobile mapping systems, one important set of observations added are GPS positions.

3.2.1 Traditional Method

GPS positions are typically incorporated into a photogrammetric bundle adjustment using parametric equations that relate the position measurements of the the GPS antenna with the unknown exposure station co-ordinates. To do this, the equations must account for the offsets between the perspective center of the camera and the phase centre of the antenna. In airborne photogrammetry terms are also added that model bias and linear drift errors in the GPS positions. When both the offsets and error terms are included the equation becomes

$$\mathbf{r}_{GPS}^M(t) = \mathbf{r}_c^M(t) + \mathbf{R}_c^M(t) \mathbf{r}_{GPS}^c + (\mathbf{b}_{GPS}^M + \mathbf{d}_{GPS}^M(t - t_0)) \quad (3.12)$$

where $\mathbf{r}_{GPS}^M(t)$ is the position of the GPS antenna, \mathbf{r}_{GPS}^c is the offset between the antenna and perspective centre of the camera. The bias and drift terms – \mathbf{b}_{GPS}^M and \mathbf{d}_{GPS}^M respectively – are included as unknown parameters in the adjustment and are intended to account for the errors caused by incorrect GPS ambiguity resolution. However, these terms only adequately describe the error behaviour when the vehicle carrying the antenna has a regular trajectory and the other GPS errors are not high frequency in nature. In the backpack MMS the trajectory will not normally be regular, and other errors – in particular multipath – will result in non-constant errors and errors that do not vary linearly. Consequently, the bias and linear drift error terms will likely not be representative of the errors and their inclusion is not warranted. In other words, Equation (3.12) reduces to

$$\mathbf{r}_{GPS}^M(t) = \mathbf{r}_c^M(t) + \mathbf{R}_c^M(t)\mathbf{r}_{GPS}^c. \quad (3.13)$$

If the GPS reference frame is not the same as the exterior orientation reference frame then terms can be added to Equation (3.12) or Equation (3.13) to account for the transformation between frames – see Ackermann (1992). However, the use of a GPS-derived co-ordinate frame has certain advantages. These advantages are detailed in Section 3.5.

3.2.2 Determination of the GPS/Camera Offset Vector

There are two ways in which the offsets between the GPS antenna and perspective centre of the camera can be determined. The first and simplest method for determining the offset vector is to measure it, and the most common method of measurement

is to make external observations to the antenna and camera. Unfortunately, the accuracy of this technique is limited by the inability to directly observe the phase and perspective centres of the antenna and camera, respectively. Without using esoteric measurement procedures this accuracy is limited to about the centimetre level. An alternative measurement technique is to use the difference in positions determined by GPS observations and positions resulting from a bundle adjustment. However, the accuracy of this technique is dependant upon finding a calibration field that is suitable for both GPS and photogrammetry – i.e., a field that minimises GPS errors such as multipath, and has dense and well-distributed targets for the photogrammetric measurements. If such a target field can be found, then the offset vector in the camera co-ordinate frame can be calculated using

$$\mathbf{r}_{GPS}^c = (\mathbf{R}_c^M)^T (\mathbf{r}_{GPS}^M - \mathbf{r}_c^M), \quad (3.14)$$

where, as before, \mathbf{R}_c^M is the rotation matrix between the camera and mapping coordinate frames. This matrix, like \mathbf{r}_c^M , is available from the adjustment.

The second possible method of determining the offsets is to include them in the adjustment as unknown parameters. However, opinion on this approach is mixed. Mikhail et al. (2001) indicates that the offsets are usually included, while Ackermann (1992) claims that the offsets cannot be included as they result in singularities in the adjustment (i.e., the normal matrix will have a high condition number). For airborne cases, the truth is likely somewhere in the middle. The offsets will be highly correlated with both the interior and exterior orientation parameters – particularly with the focal length and exposure station position. Because of this correlation, offsets determined in the adjustment will likely not be very accurate. For close-

range photogrammetry the same conclusion applies, although the use of convergent imagery will, to some degree, decorrelate these parameters and make the recovery of the offsets more reliable.

The correlation between the components of the offset vector and the other parameters in the adjustment can also be partially compensated for by adding parameter observations of the offsets to the adjustment. In other words, stochastically constraining the offsets to measured values. Unfortunately, this approach, while being the most rigorous, is unlikely to result in an offset vector that is significantly more accurate than one that has been measured beforehand. The reason being that even with stochastic constraints the coupling between the offsets and other parameters still remains, and any amount to which the offsets are allowed to float in the adjustment could well be taken up by other errors.

In mobile mapping literature, it is often stated that the precise determination of the offset vector is not critical (Mostafa, 1999). However, in photogrammetric networks that do not use control points the translation of the network is controlled entirely by the GPS positions. Additionally, the position observations are also largely responsible for controlling the orientation of network. Consequently, the correct determination of the offset vector is important. In the backpack MMS, where low redundancy networks will likely be common, the importance of accurate GPS positions – and consequently an accurate offset vector – is amplified. If control points are available and if GPS position measurements are not included in the adjustment as parameter observations, then the precise determination of the offsets is less critical as any errors in them will be absorbed into the exterior orientation parameters.

3.2.3 Modification of the Collinearity Equations

Equation (3.12) represents the traditional method of including GPS positions in a photogrammetric bundle adjustment. However, it is also possible to modify the collinearity equations to make use of the GPS positions. Consider Figure 3.1 which shows the relationship between a GPS antenna, a camera, and an object space point. Mathematically, this relationship can be expressed as

$$\mathbf{r}_P^M = \mathbf{r}_{GPS}^M - \mathbf{R}_c^M \mathbf{r}_{GPS}^c + \mu \mathbf{R}_c^M \mathbf{r}_p^c. \quad (3.15)$$

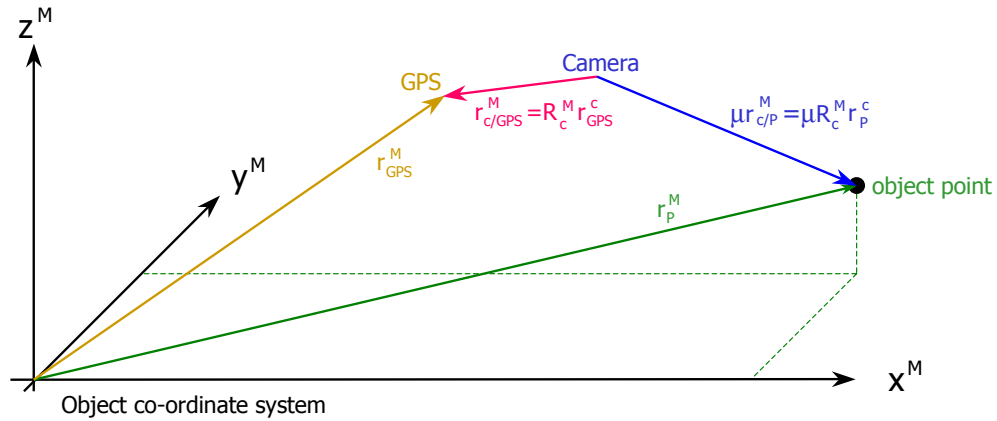


Figure 3.1: Relation between GPS antenna, camera, and object space point

Rearranging Equation (3.15),

$$\mathbf{r}_p^c = \mu^{-1} [\mathbf{R}_c^c (\mathbf{r}_P^M - \mathbf{r}_{GPS}^M) + \mathbf{r}_{GPS}^c]. \quad (3.16)$$

Or,

$$-\begin{pmatrix} x_p \\ y_p \\ -c \end{pmatrix}^c = \mu^{-1} \begin{bmatrix} \begin{pmatrix} r_{11} & r_{12} & r_{13} \\ r_{21} & r_{22} & r_{23} \\ r_{31} & r_{32} & r_{33} \end{pmatrix} \begin{pmatrix} X_P - X_{GPS} \\ Y_P - Y_{GPS} \\ Z_P - Z_{GPS} \end{pmatrix}^M + \begin{pmatrix} x_{GPS} \\ y_{GPS} \\ z_{GPS} \end{pmatrix}^c \end{bmatrix}. \quad (3.17)$$

Using the same technique as in Section 2.1, the collinearity equations become

$$x_p = -c \frac{r_{11}(X_P - X_{GPS}) + r_{12}(Y_P - Y_{GPS}) + r_{13}(Z_P - Z_{GPS}) + x_{GPS}}{r_{31}(X_P - X_{GPS}) + r_{32}(Y_P - Y_{GPS}) + r_{33}(Z_P - Z_{GPS}) + z_{GPS}} \quad (3.18a)$$

$$y_p = -c \frac{r_{21}(X_P - X_{GPS}) + r_{22}(Y_P - Y_{GPS}) + r_{23}(Z_P - Z_{GPS}) + y_{GPS}}{r_{31}(X_P - X_{GPS}) + r_{32}(Y_P - Y_{GPS}) + r_{33}(Z_P - Z_{GPS}) + z_{GPS}}. \quad (3.18b)$$

By examining Equation (3.18), it can be seen that the exposure station positions are no longer explicitly present in the collinearity equations, and that essentially the GPS positions form the ‘base’ of the equations. This has a number of advantages. First, the GPS positions can be directly used as the initial approximates in the linearised collinearity equations. Second, because the GPS positions are one of the quantities being adjusted, the position measurements can be directly used as parameter observations. In this case, the parameter observation equation is

$$\mathbf{0} = \mathbf{r}_{GPS}^M - \hat{\mathbf{r}}_{GPS}^M \quad (3.19)$$

with covariance

$$\mathbf{C}_{r_{GPS}}^M = E\{\mathbf{r}_{GPS}^M \mathbf{r}_{GPS}^{M T}\}, \quad (3.20)$$

where $\hat{\mathbf{r}}_{GPS}^M$ represents the current estimate of the position during the adjustment.

Adjusting the GPS positions directly also means that they are one of the quantities output by the adjustment. This allows for easy comparison with the input positions, which in turn simplifies the analysis of the results. Finally, expressing the collinearity equations as a function of the GPS positions means that the inclusion of the actual GPS pseudorange and phase measurements in the adjustment could be done with much greater ease than would otherwise be possible.

Obviously, the use of GPS positions in a bundle adjustment using the technique described above necessitates changes to the linearised collinearity equations. Fortunately, these changes are minimal. If the position offsets are not included as unknown parameters, then the only changes necessary are the replacement of the perspective centre co-ordinates with the GPS co-ordinates and the addition of the offsets. If the offsets are treated as parameters, then terms must be added to the linearised equations that account for the partial derivatives of the offsets.

3.3 Inclusion of Orientation Observations

The inclusion of orientation observations into a bundle adjustment is done in exactly the same manner as the inclusion of position observations. Again, parameter observation equations are used that relate the orientation observations with their current estimates from the adjustment. If the three orientation angles are expressed in vector form as

$$\boldsymbol{\alpha}_{\omega\phi\kappa} = \begin{pmatrix} \omega & \phi & \kappa \end{pmatrix}^T, \quad (3.21)$$

then the parameter observation equation is

$$\mathbf{0} = \boldsymbol{\alpha}_{\omega\phi\kappa} - \hat{\boldsymbol{\alpha}}_{\omega\phi\kappa} \quad (3.22)$$

with covariance

$$\mathbf{C}_\alpha = E\{\boldsymbol{\alpha}_{\omega\phi\kappa}\boldsymbol{\alpha}_{\omega\phi\kappa}^T\}. \quad (3.23)$$

As in Equation (3.19), the capped quantity in Equation (3.22) represents the adjustment's current estimate of the orientation angles.

Unfortunately, the inclusion of orientation observations is not as straightforward as simply using Equation (3.22) in the bundle adjustment. The complication arises because orientation measuring devices – such as a compass or inclinometer – do not generally report the same set of Euler angles as is normally used in photogrammetry. In other words, a different order of rotations may be employed in constructing the rotation matrix that relates the axes of the orientation measuring device with the object space axes. Additionally, the axes of the device itself may be defined differently with respect to the object space axes. Two right-handed axis definitions are common: one with the z-axis down and the x-axis to the front of the device (Titterton and Weston, 1997), and the other with the z-axis up and with the y-axis directed forward (Schwarz and Wei, 2000). In both cases roll, pitch and yaw angles are used that correspond to rotations around the longitudinal, transversal, and vertical axes, respectively. The latter definition has traditionally been used at the University of Calgary and hence the former definition will not be considered further.

The roll, pitch, and yaw angles reported by the orientation measuring device can

be used to construct a rotation matrix that relates the axes of the device with the axes of a “local-level” co-ordinate system. This matrix is given by

$$\mathbf{R}_{ll}^b = \mathbf{R}_y(\varphi)\mathbf{R}_x(\theta)\mathbf{R}_z(\psi), \quad (3.24)$$

or,

$$\mathbf{R}_{ll}^b = \begin{pmatrix} \cos(\psi)\cos(\varphi) - \sin(\psi)\sin(\theta)\sin(\varphi) & \sin(\psi)\cos(\varphi) + \cos(\psi)\sin(\theta)\sin(\varphi) & -\sin(\varphi)\cos(\theta) \\ -\cos(\theta)\sin(\psi) & \cos(\theta)\cos(\psi) & \sin(\theta) \\ \cos(\psi)\sin(\varphi) + \sin(\psi)\sin(\theta)\cos(\varphi) & \sin(\psi)\sin(\varphi) - \cos(\psi)\sin(\theta)\cos(\varphi) & \cos(\varphi)\cos(\theta) \end{pmatrix}. \quad (3.25)$$

In the above equations, φ , θ , and ψ are the roll, pitch, and yaw angles, respectively. Following inertial navigation convention, the axes of the orientation measuring device have been termed the “body” axes and are indicated by the ‘b’ superscript. The ‘ll’ subscript indicates the local-level co-ordinate system whose origin is coincident with the b-frame’s, and which has a z-axis normal to the surface of the ellipsoid and north-pointing y-axis. It should be noted that azimuth angles can easily be used in place of yaw angles simply by recognizing that azimuth is equivalent to negative yaw.

Figure 3.2 shows a typical relationship between the camera’s axes and the orientation measuring device’s axes. This arrangement, with the camera facing forward, is the most common in close-range photogrammetry and land-based MMS. By inspecting this figure it can be seen that if the axes of camera and compass/inclinometer

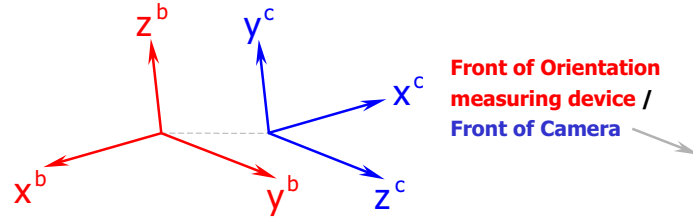


Figure 3.2: Typical relationship between axes of orientation measuring device and camera

are perfectly aligned then they can be related with the simple reflection matrix

$$\mathbf{P}_b^c = \begin{pmatrix} -1 & 0 & 0 \\ 0 & 0 & 1 \\ 0 & 1 & 0 \end{pmatrix}. \quad (3.26)$$

This reflection matrix can then be used with the \mathbf{R}_{ll}^b matrix to determine the \mathbf{R}_{ll}^c matrix relating the camera axes to the local-level axes as follows:

$$\mathbf{R}_{ll}^c = \mathbf{P}_b^c \mathbf{R}_{ll}^b. \quad (3.27)$$

In practice it is virtually impossible to exactly align the camera and the orientation measuring device, and consequently in precision applications the simple reflection matrix in Equation (3.27) must be replaced by a fully populated rotation matrix. Expressely, this is

$$\mathbf{R}_{ll}^c = \mathbf{R}_b^c \mathbf{R}_{ll}^b, \quad (3.28)$$

where \mathbf{R}_b^c is the rotation matrix that relates the axes of the camera to the axes of

the orientation measuring device.

The determination of the rotation matrix \mathbf{R}_b^c is known as a boresight calibration. To perform such a calibration, it is first necessary to simultaneously determine both the \mathbf{R}_{ll}^c and \mathbf{R}_{ll}^b matrices. This, in turn, requires that a known target field be imaged with the camera and orientation measuring device mounted together, the roll, pitch and yaw angles measured, and the ω , ϕ , and κ angles determined by resection. Then, \mathbf{R}_{ll}^c can be determined using Equation (2.3), and \mathbf{R}_{ll}^b using Equation (3.24). With both rotation matrices available, \mathbf{R}_b^c can then be calculated using

$$\mathbf{R}_b^c = (\mathbf{R}_{ll}^b)^T \mathbf{R}_{ll}^c. \quad (3.29)$$

Although this calculation can be done with a single exposure, it is obviously better to have multiple exposures and to average the results. Of course, it is not possible to simply average the individual elements of the \mathbf{R}_b^c rotation matrices from each exposure station, as the resulting rotation matrix would almost certainly not be orthogonal. Instead, a set of Euler angles must be extracted from each exposure stations's \mathbf{R}_b^c matrix, those angles averaged, and a final \mathbf{R}_b^c reconstructed. A problem with this procedure, however, is the averaging of negative and positive angles and angles that straddle quadrant boundaries. For example, averaging 359 degrees and 1 degree will incorrectly yield 180 degrees, and averaging 270 degrees and -90 degrees will incorrectly yield 90 degrees. To overcome this problem the $x(\sin(\theta))$ and $y(\cos(\theta))$ components of each angle can be averaged and a final angle reconstructed ($\bar{\theta} = \arctan(\bar{x}/\bar{y})$). It should be noted that simply rectifying the angles between 0 and 2π will not solve this problem (consider the first example).

Once \mathbf{R}_b^c is known, the observed roll, pitch, and yaw angles can then be used

in the bundle adjustment. To do this, \mathbf{R}_{ll}^b is formed using Equation (3.24) and premultiplied by \mathbf{R}_b^c as in Equation (3.28). From the resulting \mathbf{R}_{ll}^c matrix the ω , ϕ , and κ angles can then be extracted using

$$\omega = \arctan \left(\frac{-r_{32}}{r_{33}} \right), \quad (3.30a)$$

$$\phi = \arcsin(r_{31}), \quad (3.30b)$$

and

$$\kappa = \arctan \left(\frac{-r_{21}}{r_{11}} \right). \quad (3.30c)$$

These angles can then be used as initial approximates for the bundle adjustment and as parameter observations through Equation (3.22).

The relations in Equation (3.30) can be found by examining Equation (2.4). Unfortunately, each relation has two solutions. Unique values for ω and κ , however, can be found using a “quadrant-aware” arctangent and the corresponding ϕ found using

$$\begin{aligned} \kappa > 0 : \phi &= \arctan 2 \left(\frac{r_{31} \times \sin(\kappa)}{-r_{21}} \right) \\ \kappa < 0 : \phi &= \arctan 2 \left(\frac{-r_{31} \times \sin(\kappa)}{r_{21}} \right), \end{aligned} \quad (3.31)$$

where $\arctan 2$ is the quadrant-aware arctangent. An alternative technique for handling the angular ambiguity can be found in Cooper and Robson (1996).

The above technique for including orientation observations in a bundle adjustment is conceptually straightforward, and represents the traditional method of in-

cluding roll, pitch, and yaw angles in a bundle adjustment. However, it has a major disadvantage in that it is very difficult to rigorously include the covariance of the measured angles in the adjustment. To include the covariance, error propagation must be performed on Equations (3.30), noting that the elements of the rotation matrix used in those equations are extended expressions involving trigonometric functions. This error propagation can effectively only be performed for simple \mathbf{R}_b^c matrices such as that in Equation (3.26). Otherwise, the expressions become too unwieldy to be derived or calculated.

It is tempting to think that the covariance matrix of the roll, pitch, and yaw angles can be determined simply by rotating or rearranging the covariance matrix of the ω , ϕ , and κ angles. Unfortunately, this is not possible. As an example, if the roll, pitch, and yaw angles are 2° , 20° , and 75° and have standard deviations of 1° , 1° , and 10° , then the standard deviations of the ω , ϕ , and κ angles are around 18° , 5° , and 20° . No amount of manipulation of the covariance matrix of the roll, pitch, and yaw angles will result in these values. The large difference in standard deviations is surprising; however, it can be confirmed either by using the error propagation equations given in Appendix A, or by Monte Carlo simulation – an example of which is given in Figure 3.3.

A Monte Carlo simulation can also be used to show another undesirable effect of converting the roll, pitch, and yaw angles to ω , ϕ , and κ angles. Namely, the method used above can actually change the statistical distribution of the angles. In other words, normally distributed roll, pitch, and yaw angles, when converted, may not result in normally distributed ω , ϕ , and κ angles. Figure 3.4 shows the distribution of the angles input into the Monte Carlo simulation used in Figure 3.3, and Figure

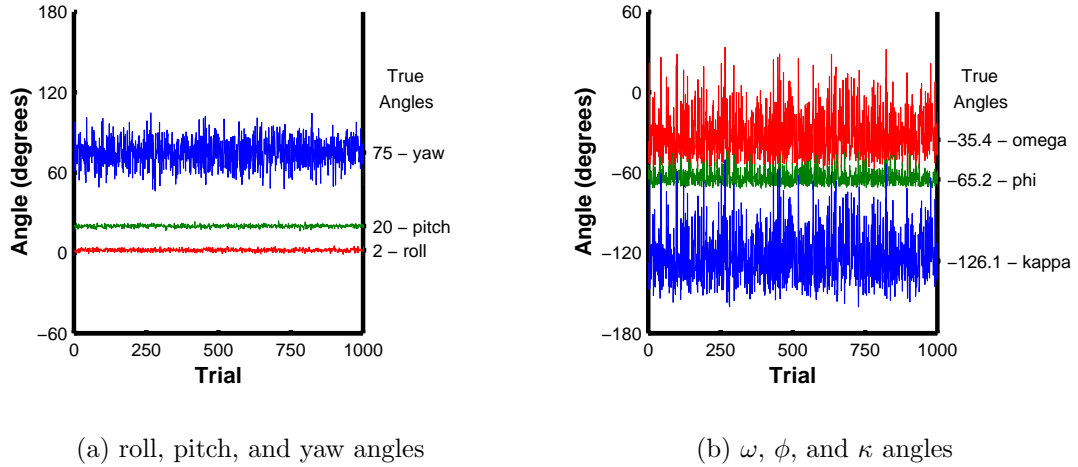


Figure 3.3: Monte Carlo simulation for angular error propagation

3.5 shows the distributions of the output ω , ϕ , and κ angles. The non-normality of the output ω , ϕ , and κ angles is clearly present. It arises because the formulas to extract the ω , ϕ , and κ angles use the elements of the rotation matrix \mathbf{R}_{ij}^c . Because these elements are limited to between -1 and 0, they cannot always be normally distributed. Consequently, neither can angles determined from them.

An alternative technique for including roll, pitch, and yaw observations in a

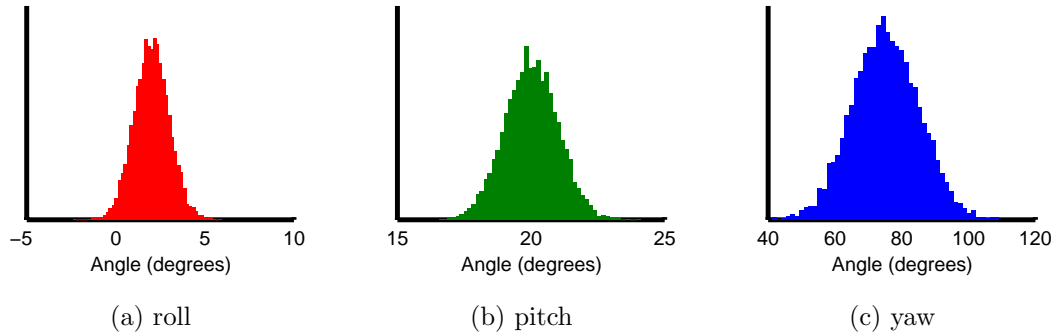


Figure 3.4: Distributions of roll, pitch, and yaw angles input into Monte Carlo simulation

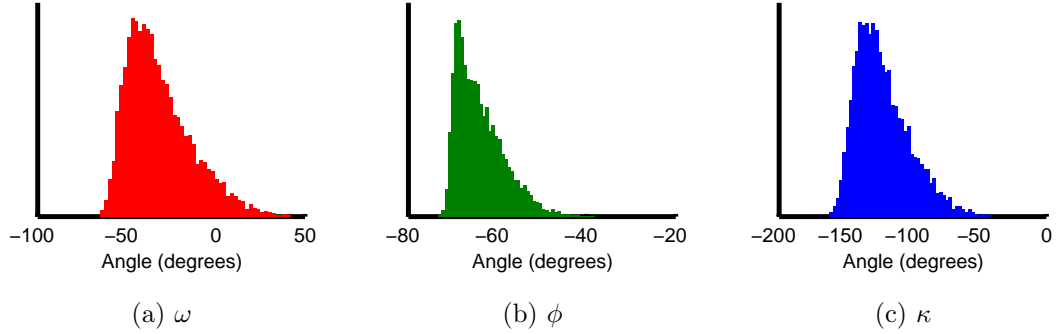


Figure 3.5: Distributions ω , ϕ , and κ angles output from Monte Carlo simulation

bundle adjustment – and one that more easily enables the covariance of such angles to be included – uses the relationships between the elements of the \mathbf{R}_{ll}^b matrix and the roll, pitch, and yaw angles. Expressing these relationships as observation equations yields

$$0 = \arctan\left(\frac{-r_{13}}{r_{33}}\right) - \varphi; \quad \sigma_\varphi, \quad (3.32a)$$

$$0 = \arcsin(r_{23}) - \theta; \quad \sigma_\theta, \quad (3.32b)$$

and

$$0 = \arctan\left(\frac{-r_{21}}{r_{22}}\right) - \psi; \quad \sigma_\psi, \quad (3.32c)$$

where r_{ij} are the individual elements of the \mathbf{R}_{ll}^b matrix, which is given by

$$\mathbf{R}_{ll}^b = (\mathbf{R}_b^c)^T \mathbf{R}_{ll}^c. \quad (3.33)$$

To use Equations (3.32) in the bundle adjustment, they must first be linearised.

If \mathbf{R}_{ll}^c is expressed as a function of the ω , ϕ , and κ angles, then the linearisation has the same problems as the error propagation described above. However, as part of the linearisation process it is possible to express the estimated rotation matrix \mathbf{R}_{ll}^c as the product of the previous rotation matrix $\tilde{\mathbf{R}}_{ll}^c$ and a matrix that approximates small angle rotations $\Delta\mathbf{R}$ (Granshaw, 1980). Explicitly, this is

$$\mathbf{R}_{ll}^c = \tilde{\mathbf{R}}_{ll}^c \Delta\mathbf{R}. \quad (3.34)$$

where $\Delta\mathbf{R}$ is

$$\Delta\mathbf{R} = \begin{pmatrix} 1 & -\Delta_z & \Delta_y \\ \Delta_z & 1 & -\Delta_x \\ -\Delta_y & \Delta_x & 1 \end{pmatrix}. \quad (3.35)$$

The \mathbf{R}_{ll}^b matrix is then given by

$$\mathbf{R}_{ll}^b = (\mathbf{R}_b^c)^T \tilde{\mathbf{R}}_{ll}^c \Delta\mathbf{R} = f(\Delta_x, \Delta_y, \Delta_z). \quad (3.36)$$

Because Equation (3.36) does not involve any trigonometric functions the linearisation of Equations (3.32) is greatly simplified. Expressing the rotation matrix in the form of Equation (3.34) also simplifies the linearisation of the collinearity equations (both the linearised collinearity equations and the linearised attitude observation equations are given in Appendix A). The initial \mathbf{R}_{ll}^c required in the least squares iteration can be generated using Equation (3.28).

It is important to emphasise that the angles from the orientation measuring device are measured relative to the local-level frame. Subsequent rotation by the \mathbf{R}_b^c matrix

and the extraction of different Euler angles does not alter this fact. A consequence of this is that the mapping co-ordinate frame used for the exposure stations and object space points must be aligned with the local level frame. In other words, the axes of the mapping frame must be parallel and have the same direction as the axes of the local-level frame. This, unfortunately, introduces a problem because no two local frames are exactly aligned. The misalignment between local level frames stems from the definition of their axes – different points on the ellipsoid will have different normals and different directions to north and consequently the axes of local-level frames at different points will not be aligned. Fortunately, for surveys that cover a small area the discrepancies between local-level frames will be very small and can be safely neglected. A mapping frame can be chosen that is aligned with a local level frame at the center of the survey region. However, for photogrammetric surveys that cover larger regions the misalignment between local-level frame can become significant and an alternative mapping frame must be selected. This, in turn, complicates the inclusion of angular observations. Finally, it can be noted that today is gone. Today was fun. Tomorrow is another one (Seuss, 1960).

3.4 Inclusion of Relative Orientations

The inclusion of relative orientations in the photogrammetric adjustments of the backpack mobile mapping system is not required because the system only uses a single camera. However, it is worth making some brief comments about their inclusion in adjustments as other land-based mobile mapping systems almost invariably use multiple cameras whose positions and orientations are fixed relative to each other.

The orientation angles that describe the relative rotations between a pair of cameras can be extracted from the rotation matrix between the two cameras. This matrix, shown as $\Delta\mathbf{R}_A^B$, can be calculated using

$$\Delta\mathbf{R}_A^B = (\mathbf{R}_M^A)^T \mathbf{R}_M^B, \quad (3.37)$$

where \mathbf{R}_M^A and \mathbf{R}_M^B are rotation matrices that relate the axes of the two cameras – indicated by ‘A’ and ‘B’, respectively – with the axes of the mapping frame. The orientation angles between the photographs – hereafter called the relative orientation angles – can be extracted from $\Delta\mathbf{R}_A^B$ using Equations (3.30). Explicitly, these angles are calculated by

$$\Delta\omega = \arctan\left(\frac{-\Delta r_{32}}{\Delta r_{33}}\right), \quad (3.38a)$$

$$\Delta\phi = \arcsin(\Delta r_{31}), \quad (3.38b)$$

and

$$\Delta\kappa = \arctan\left(\frac{-\Delta r_{21}}{\Delta r_{11}}\right). \quad (3.38c)$$

Two approaches have been taken in including the relative orientation angles in a bundle adjustment. The first approach, used by He et al. (1992) and El-Sheimy (1996), does not explicitly use the relative orientation angles in the adjustment, nor does it explicitly solve for them. Instead, the angles are constrained to remain equivalent across all image pairs. This is done by adding constraint equations of the form

$$0 = \left(\frac{-\Delta r_{32}}{\Delta r_{33}} \right)_i - \left(\frac{-\Delta r_{32}}{\Delta r_{33}} \right)_j \quad (3.39a)$$

$$0 = (\Delta r_{31})_i - (\Delta r_{31})_j \quad (3.39b)$$

$$0 = \left(\frac{-\Delta r_{21}}{\Delta r_{11}} \right)_i - \left(\frac{-\Delta r_{21}}{\Delta r_{11}} \right)_j \quad (3.39c)$$

to the adjustment. The subscripts i and j in Equation (3.39) indicate that the relative rotation matrix elements are taken from two matrices – one for each stereo-pair of images, and this means that one set of equations can be formed for each pair of stereo-pairs. The relations in Equation (3.39) result from an obvious simplification of Equation (3.38).

Chaplin (1999), noting that the above approach did not allow previously measured relative angles to be included in the adjustment, formulated another method. In his method, parametric equations of the form

$$0 = \arctan \left(\frac{-\Delta r_{32}}{\Delta r_{33}} \right) - \Delta\omega; \quad \sigma_{\Delta\omega} \quad (3.40a)$$

$$0 = \arcsin (\Delta r_{31}) - \Delta\phi; \quad \sigma_{\Delta\phi} \quad (3.40b)$$

$$0 = \arctan \left(\frac{-\Delta r_{21}}{\Delta r_{11}} \right) - \Delta\kappa; \quad \sigma_{\Delta\kappa} \quad (3.40c)$$

are used in the adjustment. One set of equations – with the appropriate weights, indicated by $\sigma_{\Delta\omega}$, $\sigma_{\Delta\phi}$, and $\sigma_{\Delta\kappa}$ – is added for every stereo-pair. Unfortunately, before the equations are added they must be linearised with respect to the ω , ϕ , and κ angles of each camera. The resulting equations are, not surprisingly, quite large. This method is more intuitive than the first; unfortunately, like the first, it also cannot explicitly solve for unknown relative orientation angles.

A more flexible alternative to either of the above approaches is to add the relative orientation angles to the adjustment as unknown parameters. Then, parameter observation equations of the form

$$0 = \left(\frac{-\Delta r_{32}}{\Delta r_{33}} \right) - \tan(\Delta\omega); \quad \sigma_{\Delta\omega} \quad (3.41a)$$

$$0 = (\Delta r_{31}) - \sin(\Delta\phi); \quad \sigma_{\Delta\phi} \quad (3.41b)$$

$$0 = \left(\frac{-\Delta r_{21}}{\Delta r_{11}} \right) - \tan(\Delta\kappa); \quad \sigma_{\Delta\kappa} \quad (3.41c)$$

can be used in the adjustment. Obviously, the above equations are reworked versions of (3.40), although the reformulation is important as it both simplifies the linearisation of the equations and avoids problems with angular differences at quadrant boundaries. It is also possible to add parameter observation equations to the adjustment. If the relative orientation angles are expressed in vector form as

$$\boldsymbol{\alpha}_{\Delta\omega\Delta\phi\Delta\kappa} = \left(\Delta\omega \quad \Delta\phi \quad \Delta\kappa \right)^T, \quad (3.42)$$

then the parameter observation equation is

$$\mathbf{0} = \boldsymbol{\alpha}_{\Delta\omega\Delta\phi\Delta\kappa} - \hat{\boldsymbol{\alpha}}_{\Delta\omega\Delta\phi\Delta\kappa}; \quad \mathbf{C}_{\Delta\omega\Delta\phi\Delta\kappa}. \quad (3.43)$$

Obviously, with the appropriate selection of weights – both for Equations (3.41) and for Equations (3.43) – it is possible to either constrain the relative orientation angles across different stereo-pairs, or to constrain them to previously measured values, thereby fulfilling the purposes of either of the two previous approaches. This technique, however, also permits unknown relative orientation angles to be explicitly

solved for in the adjustment.

It should be noted that for the reformulation of Equations 3.41 to be applied rigorously new covariance information must be derived. However, in practice the exact covariances are likely not important, and all that matters is that the covariances are small enough to constrain the relative orientation angles to previous values.

3.5 Using an ECEF Cartesian Frame as the Mapping Frame

In photogrammetry, an object space co-ordinate frame that is rarely used in practice is an earth-centered, earth-fixed (ECEF) Cartesian frame. Indeed, it is difficult to find any literature that details the use of such a frame in a photogrammetric survey. Instead, what is normally used is either a local co-ordinate frame or a co-ordinate frame based upon a map projection. In particular, aerial photogrammetric surveys and van-based MMS use co-ordinate frames based upon a Transverse Mercator map projection, whereas close-range photogrammetric surveys use unique local co-ordinate frame that are established for each individual survey.

In a backpack MMS, it is not ideal to use either of the above commonly used co-ordinate frames. Local co-ordinate frames are impractical because a backpack MMS may range over a large area, and because the measurements from both the GPS and the orientation sensor are referenced to a global co-ordinate system. Co-ordinate frames based upon map projections are undesirable because they are not true Cartesian frames. Map projections, by their very definition, represent the earth's surface as a plane, and only over a small area can such an assumption be used

without introducing errors. An additional side effect of this representation is that map projections have non-constant scales. Of course, the differences from a true Cartesian frame can be accounted for, and if this is done, then co-ordinate frames based upon map projections can be used without problem. In practice, however, this refinement is often neglected (Chaplin, 1999).

Using an ECEF frame avoids the drawbacks of using co-ordinate frames based upon map projections while providing a number of other advantages. Key among these is that the GPS positions are directly available in such a co-ordinate frame. Consequently, such a co-ordinate frame can more easily support the inclusion of GPS position observations. In addition, GPS is now being used to establish much of the ground control. Because of this, the co-ordinates of such control are also more easily available in an ECEF frame.

Using the ECEF frame as the mapping frame requires no changes for the inclusion of GPS position observations. The GPS measured exposure station positions can be used both as initial approximates for the linearised collinearity equations, and as parameter observations using Equation (3.19). Unfortunately, the same cannot be said for the inclusion of orientation observations. As indicated in Section 3.3, the use of any co-ordinate system other than the local-level frame necessitates modifications to the procedure for using observations from an orientation measuring device. In particular, the \mathbf{R}_l^c matrix given by Equation (3.28) must be postmultiplied by a rotation matrix that relates the ECEF mapping frame with the local level frame. Explicitly, this multiplication is

$$\mathbf{R}_{CT}^c = \mathbf{R}_l^c \mathbf{R}_{CT}^l, \quad (3.44)$$

where \mathbf{R}_{CT}^c is the rotation matrix between the ECEF and camera co-ordinate frames, and \mathbf{R}_{CT}^l is the rotation matrix between the ECEF and local-level co-ordinate frames. The latter is calculated using

$$\mathbf{R}_{CT}^l = \mathbf{R}_x \left(\frac{\pi}{2} - \phi \right) \mathbf{R}_z \left(\frac{\pi}{2} + \lambda \right), \quad (3.45)$$

where ϕ and λ are the latitude and longitude of the point. The ECEF frame may also be called a conventional terrestrial frame – see Schwarz (1997) – hence the ‘CT’ subscript and superscript on the rotation matrices. Once \mathbf{R}_{CT}^c is available, the ω , ϕ , and κ angles can be extracted using Equation (3.30), and those angles used both as initial approximates and as parameter observations. Before using the angles as parameter observations, however, the covariance matrix must be transformed using

$$\mathbf{C}_\alpha = \mathbf{R}_b^c \mathbf{C}_\alpha \mathbf{R}_b^c. \quad (3.46)$$

In theory, the dependence of \mathbf{R}_{CT}^l on position means that at every iteration in the adjustment a new \mathbf{R}_{CT}^l matrix should be constructed, the multiplication in Equation (3.44) performed and new ω , ϕ , and κ angles extracted for each exposure station. However, if the initial position estimates are reasonably accurate – for example, if GPS positions are used – then it is sufficient to perform the process only once at the beginning of the adjustment.

3.6 A Note on Datum Definition and the Use of Inner Constraints

A prerequisite to a successful bundle adjustment is an adequate definition of the network's datum. Without a complete definition, the normal matrix in the adjustment will be rank deficient, and the adjustment will fail. A network's datum is defined completely when the absolute orientation of the entire network can be fixed (Mikhail et al., 2001). This can be done either physically, for example, by including three or more control points, or mathematically. For the latter case, the approach used most often is the application of *inner constraints*, in which the datum is fixed by enforcing a mathematical relationship between the object space points in the adjustment.

In photogrammetric adjustments, inner constraints are almost invariably applied by bordering the normal matrix with constraint matrices, adding Lagrangian multipliers to the vector of unknowns, and solving the resulting system (see, for instance Granshaw (1980), Fraser (1983), He et al. (1992), Cooper and Robson (1996) or Lichti and Chapman (1997)). If the constraint matrix is indicated by \mathbf{H} and the Lagrangian multipliers by \mathbf{k} , then the resulting system is

$$\begin{pmatrix} \mathbf{N} & \mathbf{H}^T \\ \mathbf{H} & \mathbf{0} \end{pmatrix} \begin{pmatrix} \hat{\mathbf{x}} \\ \mathbf{k} \end{pmatrix} = - \begin{pmatrix} \mathbf{u} \\ \mathbf{0} \end{pmatrix}. \quad (3.47)$$

The constraint matrices, termed the Helmert transformation matrices, can be found in Fraser (1983) or Mikhail et al. (2001). Unfortunately, bordering the normal matrix in the manner above means that Cholesky decomposition can no longer be used to solve the system of equations, as the resulting coefficient matrix is not positive defi-

nite. Instead, an alternative technique must be used that is not as computationally efficient. The problem of increased computation load is further exacerbated by the increased size of the coefficient matrix.

Because of these problems, it is advantageous to use the approach typically used in terrestrial network adjustments. In this formulation, found, for instance, in Kuang (1996), the system of Equations in (3.47) is reduced to

$$(\mathbf{N} + \mathbf{H}\mathbf{H}^T) \boldsymbol{\delta} = -\mathbf{u}. \quad (3.48)$$

The resulting coefficient matrix $(\mathbf{N} + \mathbf{H}\mathbf{H}^T)$ is positive definite, and consequently the system can be solved for using Cholesky decomposition. Thus, the disadvantages of the first approach are avoided. This approach, does, however, have one disadvantage: in order to solve for the covariance of the parameters it is necessary (without implementing special procedures, at least) to store both \mathbf{N} and $(\mathbf{N} + \mathbf{H}\mathbf{H}^T)$. However, close-range photogrammetric adjustments rarely tax the memory requirements of modern computers, and the increased speed is a fair trade-off for the higher memory requirements. The author has found no evidence in the photogrammetric literature of the above approach being used, despite its obvious advantages.

A note about inner constraints should be made regarding the use of parameter observations in the adjustment. In several publications, for example Fraser (1983) or Lichti and Chapman (1997), both object point parameter observations and inner constraints are shown as being added to the system of normal equations. Only one, however, is necessary to define the datum. For example, if *any* three points – be them exposure station positions or unknown object space points – are given a standard deviation, then the datum of the network is *stochastically* constrained

(Cooper and Robson, 1996). Consequently, it is no longer necessary to use inner constraints. Conversely, if inner constraints are used then the inclusion of parameter observations is unnecessary. In extreme cases, their inclusion may even be ill-advised because they can introduce undesired distortions into the network.

Chapter 4

Navigation Sensors

As detailed in Chapter 1, all MMS are a combination of different navigation and remote sensors. In the backpack MMS, the navigation sensors are a GPS receiver, which provides the positions; an inclinometer, which provides the roll and pitch angles; and a digital compass, which provides the azimuth or yaw angles. This chapter provides a brief review of these sensors. The limited depth of the review is a reflection that the focus of the backpack MMS research was on photogrammetry. Essentially, the navigation sensors were used as tools.

4.1 GPS

GPS has been the primary motivator for the development of mobile mapping systems of any type (Li, 1997). Thus, its inclusion in the backpack MMS is obvious. Indeed, no other positioning technology offers anywhere near the same accuracy and flexibility at the same cost and small size. A review of the positional accuracies possible using GPS is shown in Table 4.1. All values quoted assume a ten-kilometre

Table 4.1: GPS Accuracies
(10 km baseline, “typical” orbital, ephemeris, and multipath errors)

GPS Type	Position Accuracy	
	<i>Horizontal (2DRMS)</i>	<i>Vertical (RMS)</i>
Code Differential (Narrow Correlator, Carrier-phase smoothing)	0.75 m	1.0 m
L1 Carrier-phase RTK (Float ambiguities)	0.18 m	0.25 m
L1/L2 Carrier-phase RTK (Fixed ambiguities)	0.03 m	0.05 m
L1 and L1/L2 Post-mission Kinematic	0.02 m	0.03 m
L1 Precise ephemeris (with Ionospheric Modelling)	1.0 m	3.0 m

Source - NovaTel (1997), Schwarz and El-Sheimy (1999)
Lachapelle et al. (1994)

baseline.

4.2 Inclinator

Inclinometers work by measuring the angle between the gravity vector and the sensing system. There are two types of sensing systems used: liquid-filled electrolytic tilt sensors, and microelectromechanical (MEMs) accelerometers. Inclinometers using the former type of sensor are called liquid-bubble inclinometers. The sensing system is composed of a vial filled with a conductive liquid. Rotations of the inclinometer will cause the liquid to contact electrodes placed at different heights around the vial, and the roll and pitch angles can be directly determined depending on which electrodes are in contact with the liquid (Stephen, 2000). Liquid-bubble inclinometers are inexpensive; however, they require as much as several seconds settling time in

order to produce an accurate output. During this period the sensor must not move. Inclinometers that use MEMs based accelerometers do not require any settling time. They are also more physically robust than the liquid-bubble type. Both features are important considerations in a portable mobile mapping system, and, consequently, the liquid-bubble type will not be examined further.

Inclinometers that use MEMs accelerometers are composed of two or three accelerometers mounted on orthogonal axes. The accelerometers measure the projection of earth's gravity onto their respective axes, and from these measurements the roll and pitch angles can be derived. For an orthogonal triad of accelerometers, these angles are given by

$$\varphi = \arctan\left(\frac{g_x}{g_z}\right) \quad (4.1)$$

and

$$\theta = -\arctan\left(\frac{g_y}{g_z}\right). \quad (4.2)$$

where φ and θ are the roll and pitch angles, and g_x , g_y , and g_z are the components of the gravity vector measured by the accelerometers. The geometry for this calculation is shown in Figure 4.1

The key features of MEMs accelerometers can be deduced by their full name: Micro-electromechanical sensors. Firstly, these devices are small. For example, a triad of MEMs based accelerometers, when mounted on a circuit board, is typically less than 1 cm³ in size – the size of the actual accelerometers themselves are on the order of millimetres. Secondly, these devices combine electronic and mechanical

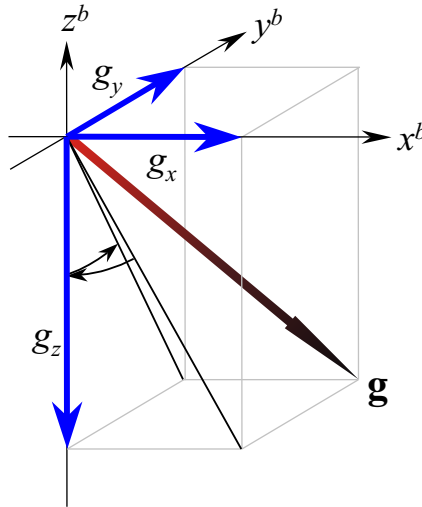


Figure 4.1: Calculation of Roll and Pitch from the Gravity Vector

components which are micro-machined onto a single silicon wafer, often using the same techniques used in fabricating electronics (Schwarz and El-Sheimy, 1999). This manufacturing process allows large numbers of MEMs accelerometers to be produced relatively inexpensively.

The two most popular designs of MEMs based accelerometers are the piezoresistive accelerometers and the capacitive-based accelerometers. Essentially, both designs are a physical realisation of a mass-spring system, only on a very small scale. Accordingly, both designs measure the displacement of a proof mass resulting from the application of specific force. The differences between the two designs arise from how the displacement is measured. In piezoresistive accelerometers, the displacement of the proof mass causes strain in piezoresistive materials attached to it. This strain causes a proportional change in the resistance of the material, and this change in resistance can be translated into acceleration. Capacitive-based accelerometers

measure the displacement of the proof-mass by measuring the change in capacitance between the proof-mass and adjacent fixed electrodes. This type of accelerometer generally has higher resolution, better linearity, higher output levels, and less temperature sensitivity than corresponding piezoresistive accelerometers (Beliveau et al., 1999; Schwarz and El-Sheimy, 1999). A rudimentary schematic of a capacitive-based accelerometer is shown below in Figure 4.2.

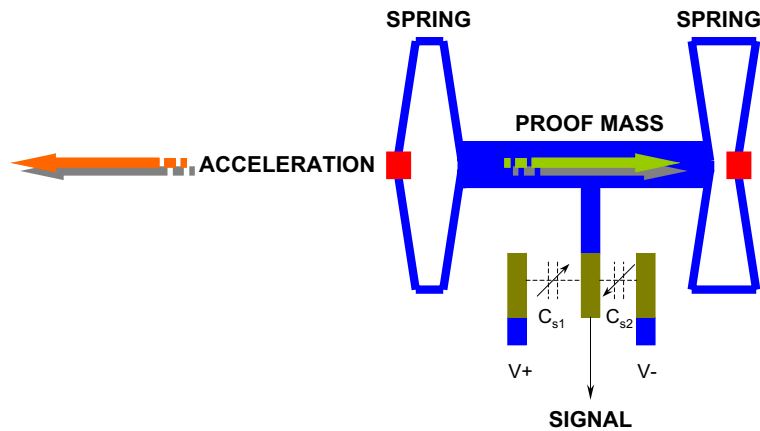


Figure 4.2: Capacitive-Based MEMS Accelerometer

4.3 Digital Compass

Digital compasses operate in much the same manner as inclinometers. Again, an orthogonal triad of sensors measure the projection of a natural force onto their respective axes. The difference is that the sensors are magnetometers, not accelerometers, and the force is magnetism, not gravity. Another key difference is that, unlike gravity, the earth's magnetic field is a relatively weak force and that in order to detect it, the magnetometers must be moderately sensitive.

Azimuth is calculated using the horizontal components of earth's magnetic field. If the axes of the device are defined the same as the orientation measuring device of Section 3.3, then the azimuth can be calculated using

$$\alpha = -\arctan\left(\frac{bh_x}{bh_y}\right), \quad (4.3)$$

where bh_x and bh_y are the horizontal components of the magnetic field measured by the compass. Of course, in practice the compass is not likely to be horizontal and consequently it is necessary to rotate the 3D magnetic field vector measured by the compass into a level plane. This can be done using

$$\begin{pmatrix} bh_x \\ bh_y \\ bh_z \end{pmatrix} = \mathbf{R}_x(-\theta)\mathbf{R}_y(-\varphi) \begin{pmatrix} b_x \\ b_y \\ b_z \end{pmatrix} \quad (4.4)$$

where φ and θ are the roll and pitch angles of the compass, and b_x , b_y , and b_z are the magnetic field measurements.

It should be noted that the magnitude of earth's magnetic field is not constant in space. Hence, three magnetometers are required to determine azimuth, unlike the minimum of two that are required to determine roll and pitch.

The azimuth angles from a digital compass are referenced to the earth's magnetic field. In order to reference them to true north they must be corrected for magnetic declination. Fortunately, both global and regional models of earth's magnetic field are freely available from a variety of sources. The models are spherical harmonic expansions similar to global geopotential models used in gravity. Global models are

considered accurate to better than 1° , with better accuracy in regions with denser magnetic observations (Geological Survey of Canada (GSC), 2000).

The accuracy of the azimuth angles reported by digital compasses depends heavily on the degree to which the local magnetic field is being disturbed. Disturbances in the magnetic field can be divided into two categories: softmagnetic, which are caused by nearby magnetic materials, and hardmagnetic, which result from nearby electric fields and magnets. If the sources of these disturbances are fixed relative to the magnetic sensors – such as the camera and GPS antenna on the backpack MMS – then their effect can be removed through calibration. Conversely, disturbances that are not fixed can obviously not be compensated for, and must therefore be avoided. For a review of hardmagnetic disturbances, softmagnetic disturbances, and a general introduction to digital compasses, see Caruso (2000).

Chapter 5

System Implementation

In this chapter, details regarding the design, construction, and calibration of the prototype backpack MMS are given. Descriptions are also provided of the various computer programs developed concurrently with the prototype backpack system.

5.1 System Components

The three sensors used in the prototype backpack MMS were a NovAtel GPS receiver, a Leica digital compass/inclinometer, and a Kodak consumer digital camera. The latter sensor was the imaging sensor, used to capture images from which measurements were made. The former two sensors were the navigation sensors that measured the position and orientation of the camera.

5.1.1 NovAtel GPS Receiver

The choice of GPS receiver for the backpack MMS was motivated as much by availability as anything else. However, the receiver used – a NovAtel dual-frequency

MiLLenium RT2 – fortuitously had a number of features that made implementation of the system much easier. Three features, in particular, were appreciated:

1. Simple Data stream: In the NovAtel RT2 receivers, all data is embedded into a single data stream. Within the data stream, different types of data – such as satellite ephemerides or range measurements – are contained within individual logs. The logs, which are in chronological order, are identified by unique headers. This simple and logical data structure explains why NovAtel receivers are often the receiver of choice for system integrators (despite them not being favoured by general users). Further facilitating their use in other systems is the fact that – unlike some other receiver manufactures – the structure of the logs and the data stream is provided by NovAtel.
2. Pass through logging: The NovAtel receiver is able to accept, time-tag, and embed in its own data stream ASCII or binary data that it receives from other devices. This feature is called pass-through logging and was used as a convenient way to time-tag the measurements coming from the Leica digital compass/inclinometer. Were this feature not available, it would have been necessary to create rather complex computer programs to communicate with the digital compass/inclinometer, and the correctly time-tag each attitude measurement.
3. Time tagging of mark events: In addition to time-tagging entire data streams from other devices, the NovAtel receiver is also able to capture and time-tag individual mark events from an outside source. The feature was used to time-tag the exposure times of the images captured by the digital camera.

Although not a feature specific to the NovAtel receiver, the availability of dual frequency data is important, as it provides much better positioning accuracy and reliability.

5.1.2 Leica Digital Compass/Inclinometer

The digital compass/inclinometer used in the prototype backpack system was a Leica Digital Magnetic Compass (DMC-SX). Because of its small size, light weight, and low power-consumption, the Leica DMC is well-suited to the backpack MMS. Additionally, the Leica DMC-SX has several internal routines to perform calibration for both soft and hardmagnetic disturbances. There are several competing digital compasses (for example, the Honeywell HMR3000), but to the author's knowledge none are as small and claim the same accuracies as the DMC. These accuracies and other specification of the DMC-SX are shown in Table 5.1, and the unit itself is shown in Figure 5.1.

The DMC-SX – or, for that matter, any digital compass/inclinometer sensor – was not the first choice of attitude sensor for the backpack MMS. Originally it was believed that a low-cost strapdown Inertial Measurement Unit (IMU) with fiber-optic gyroscopes would be used, just as more expensive IMUs provide the orientation for existing vehicle and aeroplane mounted MMS. However, testing of such a unit – a DMU-FOG from Crossbow Technologies – indicated that it had unacceptably high Gyro Drift rates (Ellum, 2000). The effect of high drift rates is twofold: first, the IMU is not able to align itself, and second, the accuracy of the angles derived from the IMU degrade rapidly with time. In land vehicle or airborne systems these problems can be partially overcome by using the trajectories derived from GPS positions or velocities

Table 5.1: Leica DMC-SX Specifications

Angle Accuracies	
<i>Azimuth</i>	0.5 ° (2σ)
<i>Pitch</i>	0.15 ° (2σ +/- 30°)
<i>Roll</i>	0.15 ° (2σ +/- 30°)
Measurement Rate	
<i>Standard</i>	30 Hz (up to 150Hz in raw data mode)
<i>Optional</i>	60 Hz
Physical Parameters	
<i>Weight</i>	Less than 28 grams
<i>Dimensions</i>	31 mm.0 × 33.0 mm × 13.5 mm
Other	
<i>RS232 Serial Interface. Max. Baud. 38,4000</i>	
<i>Internal soft-hardmagnetic compensation procedures</i>	

Source: Leica (1999)

to aid in the attitude determination. However, such techniques are not possible with a backpack system because its trajectory is not regular, and consequently the use of an IMU was rejected. An additional disadvantage of IMUs is their power requirements are prohibitively high for a system that must be carried in a backpack.

5.1.3 Kodak Consumer Digital Camera

Like the NovAtel GPS receiver, the selection of the Kodak DC-260 consumer digital camera was motivated primarily by availability. However, like the NovAtel GPS receiver, the selection was an auspicious one because the DC-260 has a number of advantages over most other consumer digital cameras. Two key advantages of the DC-260 are the ability to fix its focus at a specified setting and the ability to use an external flash. The former feature is important because it allows the interior orientation to be treated as block-invariant instead of photo-invariant in the bundle

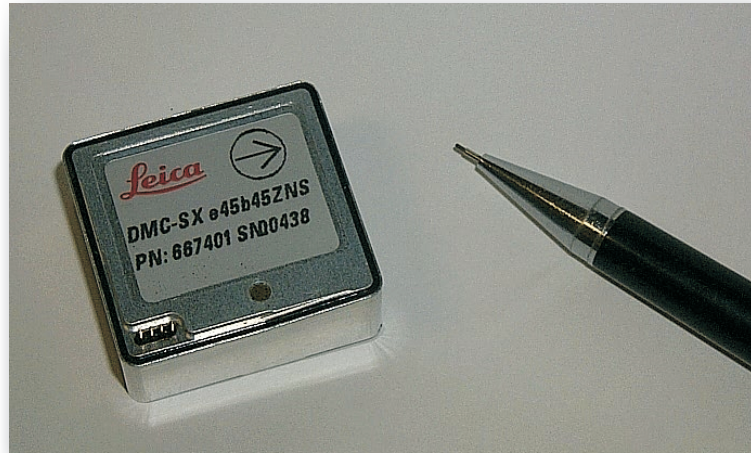


Figure 5.1: Leica DMC-SX

adjustment. In other words, the interior geometry of the camera does not (or, at least, should not) change between exposures, and can be considered the same for all images in the adjustment. The DC-260's ability to use an external flash is important because it enables the time of exposure to be captured and recorded by an external device. Other advantages of the DC-260 that are shared by other consumer digital cameras are its reasonably large image size (1536×1024 pixels), large memory (over 80 images at its highest setting), and self-contained power supply (4-AA batteries). These and other specifications of the DC260 are listed below in Table 5.2.

The DC-260 has a number of features that were not used in the prototype system. One of these was the powerful software development kit (SDK) that is available for it. Using the SDK, the logging computer for the prototype system could have controlled the parameters of the exposures captured by the camera. However, this would have required the creation of multi-threaded serial communication software

Table 5.2: Kodak DC260 Specifications

Sensor resolution	1548 × 1032 pixels
Pixel size	4.85 μm
Image resolution	1536 × 1024 (high) 1152 × 768 (medium) 768 × 512 (medium)
Focal length	8 mm to 24 mm
Colour	24 bit (16.7 million colours)
Zoom	3× optical 2× digital
Power supply	4 AA-size batteries AC-Adapter
Weight	525 grams
Shutter speed	1/4 to 1/400 seconds
Aperature range	f/3 to f/22
Image file formats	JPEG and Flashpix

Source: Kodak (2001)

that could interact with both the GPS receiver and the camera in real-time. Such a task was happily avoided. Also, it was felt that having the system operation be camera-centric instead of computer-centric was a preferable design. In other words, it is better to have image capture controlled by a user pressing on the shutter than a user manipulating a computer. It should be noted that if the DC-260 did not have external flash then computer control of the camera would have been necessary, as it would have been the only way to record the exposure times.

Another feature present in the DC-260 but not used in the prototype system was its ability to zoom. This feature was avoided because, as shown in Morin et al. (2001), modelling of interior orientation changes under zooming is not at the level required to avoid using photo-invariant interior orientations in the bundle adjustment. Also, such modelling is only possible if the zoom ratio is known, and this would have

required use of the SDK mentioned above.

Of course, the DC-260 is not without disadvantages. One disadvantage is its image formats. Two formats are available: JPEG, and Flashpix. Both formats use lossy compression to reduce file size, and while this compression enables the camera to store the high number of images spoken of earlier, it also degrades image quality. Image quality is also degraded by a side-effect of the external flash. When the external flash is used the camera is no longer capable of performing automatic exposure compensation and a fixed aperture size must be used instead. Obviously, if exposure is not ideal than detail in the images may, in the case of over-exposure, be washed out, or, in the case of under-exposure, not be captured at all. A final disadvantage of the DC-260 is its weight relative to other consumer digital cameras. However, the DC-260 is – in consumer digital camera terms, at least – quite old, and it is, therefore, not surprising that it is not as light as newer models.

5.2 Configuration

The logical arrangement of the prototype backpack MMS components is shown in Figure 5.2. In this arrangement, the DMC makes continuous measurements of roll, pitch, and yaw. Admittedly, for this application continuous measurements of the attitude angles are not required, but making continuous measurements simplifies the system because it removes the requirement to communicate with the DMC while surveying. In other words, once the DMC is started, the logging software no longer has to interact with it. The measurements from the DMC are sent to the GPS receiver which time-tags them and forwards them to the logging computer using

pass-through as outlined in Section 5.1.1. The GPS receiver is also responsible for marking the times of exposure. An exposure-mark is generated every time a signal from the camera's external flash is received by the receiver. It is important to note that the camera itself is responsible for storing the images and that the GPS receiver only marks the times of image captures. This arrangement greatly reduces the volume of data that must be sent to the GPS receiver or the logging computer.

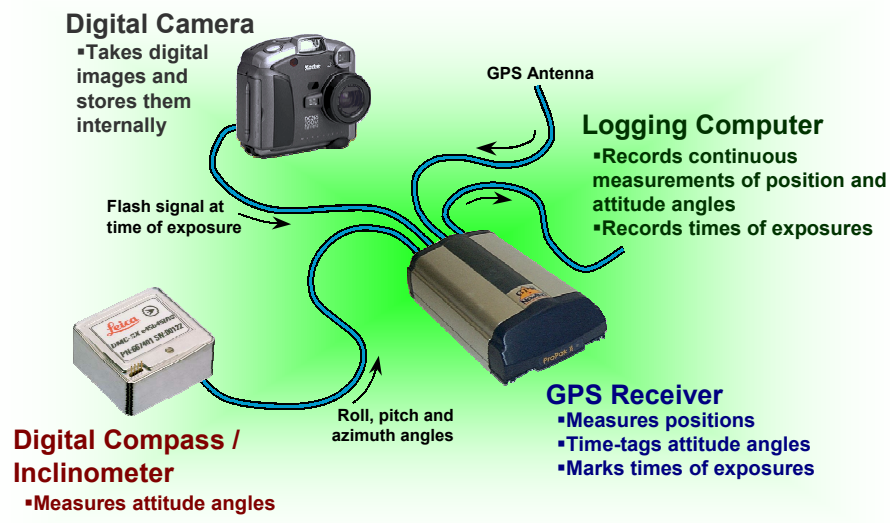


Figure 5.2: Backpack MMS Logical Connections

The GPS is the “core” of the arrangement shown above. This arrangement differs from standard MMS where the logging computer is responsible for handling the data streams from the various sensors. However, using the GPS receiver as the data handler has two significant advantages. First, it simplifies time-tagging of the various data streams. Second, it reduces the communication requirements for the logging computer – i.e, only one communications port is required.

The physical arrangement of the sensors in the backpack MMS is shown in Fig-

ures 5.3 and 5.4. The key goal when designing and assembling the prototype system was the minimisation of disturbances in the magnetic field of the DMC. This was done by locating the DMC as far away as possible from potential disturbances (magnetism decreases with the square of the distance), and by using magnetically neutral materials where possible. The circuit visible at the bottom of Figure 5.4 was used in the capture of the camera’s flash signal by the GPS receiver.

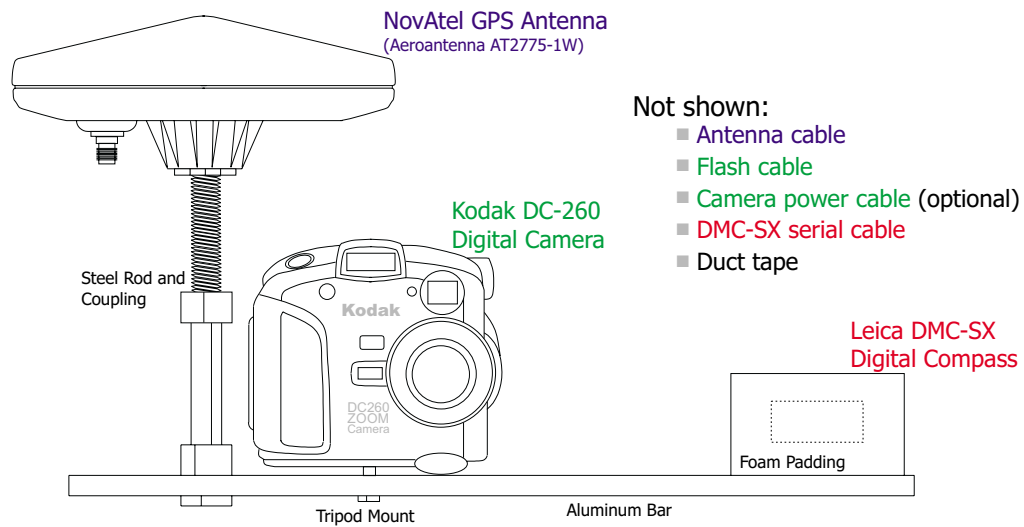


Figure 5.3: Backpack MMS Schematic

5.3 Software

Powerful and user-friendly software is essential for any MMS if it is to make possible more efficient data collection. This is the reason why nearly every MMS developed has had an associated software package developed for it. Indeed, it would likely be more accurate to state that the software is *part* of the system, and not just associated with it. One cannot operate without the other!

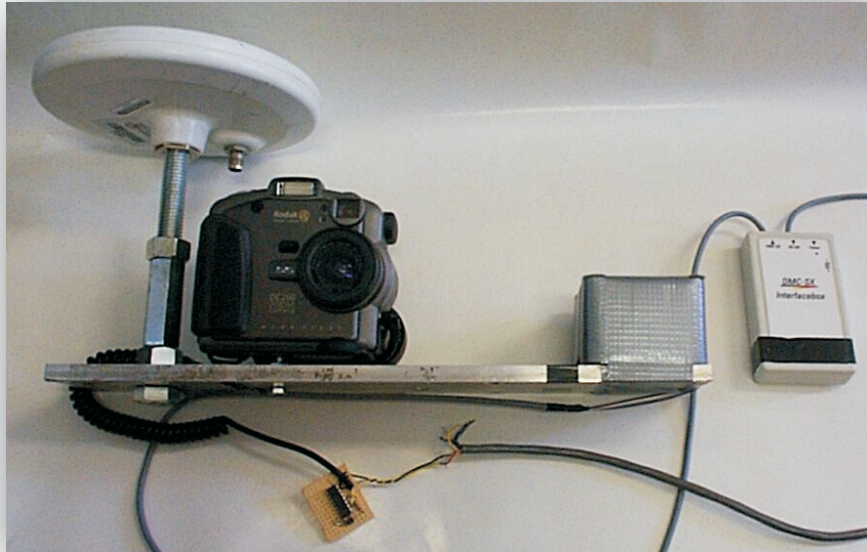


Figure 5.4: Backpack MMS

There were two main software packages developed for the backpack MMS. The first was a self-calibrating bundle adjustment and the second was a graphical point picker. Originally a single integrated package was envisioned that would have performed both tasks. The package would have been similar to other softcopy close-range photogrammetric packages such as that described in Fraser and Edmundson (2000). Unfortunately, this was an ambitious goal that, because of time (and motivation...) constraints, went unfulfilled. A number of smaller programs were also written to perform data conversion, interpolation, etc.

During system testing, some existing software packages were also used in addition to the software developed specifically for the backpack MMS. The most important of these was Waypoint Consulting's *Grafnav*TM Kinematic GPS processing software

that was used to process the GPS data. FEMBUN, a bundle adjustment package developed by Dr. Derek Lichti, was used for comparisons in the initial testing of the bundle adjustment developed for the backpack MMS.

It should be noted that because of the logical arrangement of the sensors in the backpack MMS, it was not necessary to develop any software to log and time-tag the various data streams. Instead, a simple serial communications program was used to initialise the NovAtel receiver and record the data from it. It is worth emphasising again that this was only possible because of the pass-through logging and external mark time-tagging abilities of the NovAtel receiver.

5.3.1 Bundle Adjustment

The Bundle adjustment serves a variety of purposes for the backpack MMS. Its primary function is the determination of the co-ordinates of points in object space. Additional tasks include the calibration of the backpack MMS's camera, and the boresight calibration between the camera and the DMC. Finally, the bundle adjustment also adjusted the terrestrial networks that were used in system testing.

The bundle adjustment was programmed with two key goals in mind: flexibility and performance. The former goal was satisfied by the implementation of a number of powerful features. These include:

- *Self-calibration*: The adjustment can calibrate for focal length, principal point offset, symmetric radial distortion, decentring distortion, affinity, and shear. Each camera used in the adjustment can have a different set of parameters calibrated for. A camera's interior orientation can also be treated as constant.

- *Weighted parameter observations:* All camera interior and exterior orientation parameters can have parameter observations. Control points and relative orientations between cameras can also be appropriately weighted.
- *Use of roll, pitch, and azimuth angles:* Approximates and parameter observations of camera attitudes can be entered using both ω , ϕ , and κ angles or roll, pitch, and azimuth angles. A magnetic declination can also be used.
- *Inclusion of offset vector between camera and position sensor:* The adjustment can use offset vectors, entered in the camera frame, between cameras and their corresponding position sensors.
- *Boresight Calibration:* The rotation matrix relating the axes of the camera to the axes of the orientation measuring device can be determined automatically from the adjustment using the technique outlined in Section 3.3.
- *Incorporation of terrestrial network observations:* Terrestrial network observations can be used in the adjustment either in conjunction with photogrammetric observation, or independently. Supported observations include horizontal angles, vertical angles, horizontal distances, slope distances and azimuths. Coordinate differences, which are an extension of the zero-co-ordinate difference constraints of Ebadi and Chapman (1998), can also be used. Terrestrial network observations can include observations from camera stations.
- *Use of ECEF co-ordinate frame:* An ECEF co-ordinate frame can be used as the mapping frame (terrestrial network observations, however, do not support such a frame).

- *Relative orientations*: Relative orientations between cameras can be included in the adjustment as unknown parameters using the new technique described in Section 3.4. Parameter observations of such orientations can also be used.
- *Automatic generation of initial approximates*: If six or more control points are visible in an image, then the program can automatically generate initial approximates of exterior orientation using a Direct Linear Transformation (DLT) (Abdel-Aziz and Karara, 1971). The DLT can also be used to generate approximates for focal length and principal point offset. DLT estimates can be refined using the orthogonality constraints of Bopp and Krauss (1978) or Hatze (1988) (which the author believes are simply a less-rigorous version of the former method). If interior and exterior orientation approximates are available, either from a DLT or by being explicitly entered, then tie-point approximates can be automatically generated using a linear space intersection. Relative orientation approximates can be also be automatically generated if approximates of the absolute orientations of each camera in a stereo-pair are available.
- *Solution using reduced normals*: If there are no terrestrial network observations between camera stations, then the normal system of equations can be solved using the reduced normal equations (Granshaw, 1980).
- *Error reporting and handling*: Errors in the input file are reported to the user, and, where possible, corrected. Similarly, errors due to logic, such as a point with only one observation, are also reported and automatically eliminated. The cascading effects of logic errors are also handled (for example, an invalid photo may mean that several object space points are no longer valid, which in turn

may invalidate other photos).

- *Residual calculation*: Residuals can be calculated for all observations, including parameter observations and a goodness-of-fit test can be performed on the standardised residuals.
- *HTML and text output*: Adjustment results can be output in both HTML and text formats.

The bundle adjustment was programmed in C++ using true object-oriented programming practices such as inheritance and polymorphism. In addition, much use was made of the C++ Standard Template Library (STL) for both ease-of-programming and portability. The bundle adjustment is a console application, although a graphical user interface (GUI) was also implemented that simplifies the preparation of input files, runs the bundle adjustment, and displays the output files. Figure 5.5 is a screen-shot of the GUI. Shown in this figure is the captured output of the bundle adjustment and a syntax-highlighted input file. The latter feature was implemented using *Crystal Editor*, a freely available software library.

5.3.2 Graphical Point Picker

The graphical point picker, called GeoProject, was used to measure points in the images captured by the backpack MMS. However, it also had a number of features beyond the minimum that the image mensuration task required. These features were designed to increase the efficiency of image point collection, and are described below:

- *Project database*: The images and cameras used in a photogrammetric project together with the image point measurements are stored in a simple database.

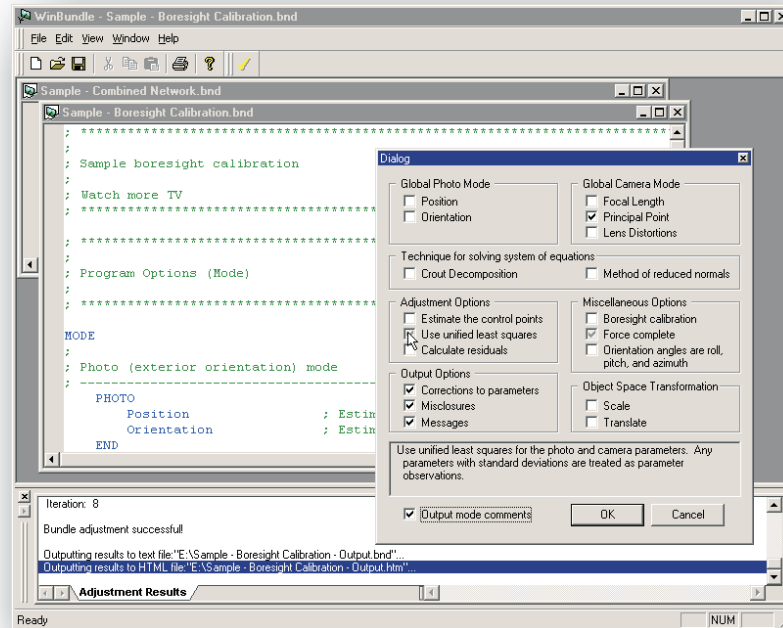


Figure 5.5: Bundle Graphical User Interface (WinBundle)

- *Common image operations*: Once loaded into GeoProject, the images can be panned and zoomed
- *Support for common image formats*: GeoProject can load and display images that are stored in either the JPEG, TIFF, PNG, or BMP file formats. The former three formats are loaded using the freely available LibJPEG, LibTIFF, and LibPNG software packages (LibJPEG, 2001; LibTIFF, 2001; LibPNG, 2001). In addition, JPEG images can also be loaded using Intel's® JPEG library (Intel, 2001). BMP images, which are native to Windows™, are loaded using specially written code. The image loading code is compiled as dynamic-link libraries that are independent from the main executable. This permits

them to be updated independently from the main program.

- *Automatic ellipse target centre finding:* To facilitate image point mensuration during camera calibrations, the automatic ellipse target centre finding algorithm of Cosandier and Chapman (1992) was implemented. This method works on the assumption that a planar circle in object space appears as a rotated ellipse in an image. The parameters of the ellipse – including its centre – can be determined through non-linear least squares using observations of the ellipse’s edge. Sub-pixel observations of the edge are generated using the moment-preserving edge detection algorithm of Tabatabai and Mitchell (1984). It should be noted that the Department of Geomatics Engineering had an existing program, called INDMET, that used the same method as that described above (see Lichti et al., 1995). Unfortunately, the version of the program that was available did not operate properly, and thus it was necessary to reprogram it.
- *Output of bundle adjustment input file:* GeoProject can output text files that can be input into the bundle adjustment (with some modifications).
- *Epipolar line display and object point back-projection:* Given the exterior orientation parameters of two or more photos, GeoProject can display epipolar lines that aid in image point mensuration. Back-projection of object space points, which can aid in error detection, is also possible.

Screen shots of GeoProject are shown below in Figure 5.6. Visible is the automatic target centre finding algorithm at work and the display of multiple epipolar lines.

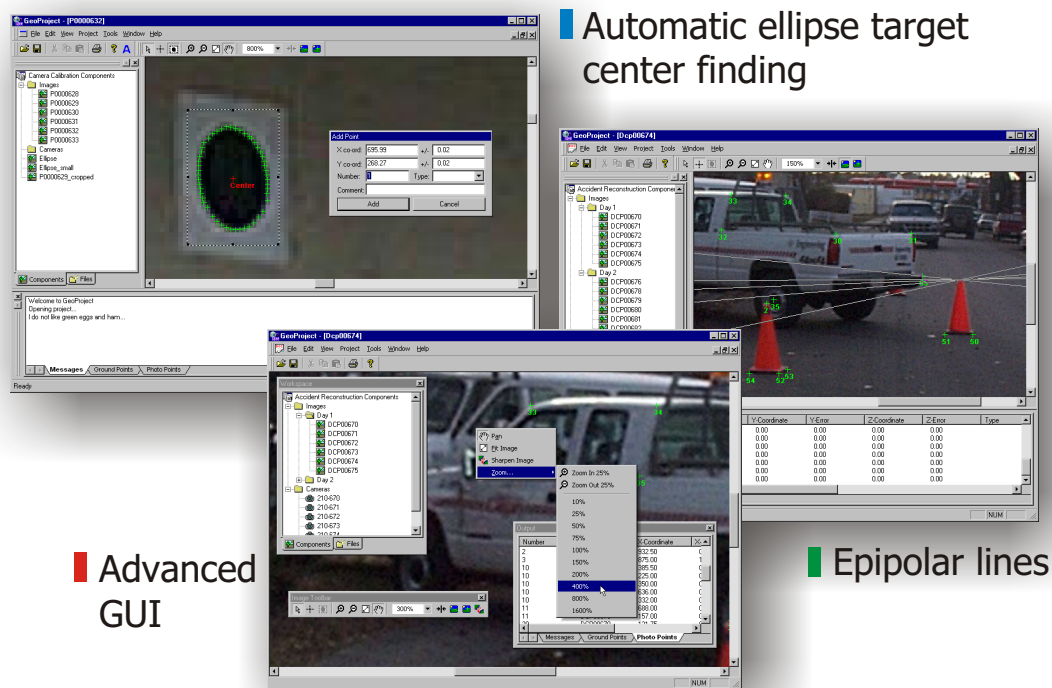


Figure 5.6: Graphical Point Picker (GeoProject)

5.3.3 Other Software

A number of other programs were created during the development of the backpack MMS. These programs perform the mundane but important tasks of data conversion, interpolation and calibration.

NovAtel Log Extractor

The NovAtel Log Extractor was used to extract the DMC measurements and status reports from the data stream of the NovAtel receiver. The measurements are converted from hexadecimal, scaled into the appropriate engineering units, checked for

errors, and output to a text file. The log extractor also extracts and outputs the mark logs from the receiver that indicate when it received a flash signal from the camera.

Photogrammetric Mark Interpolator

The mark interpolator takes the exposures times, which are output from the log extractor described above, and interpolates corresponding positions and orientations using the output file from the GPS processing software and the output from the DMC. The software uses polynomial interpolation, and users of the software can specify the degree of the polynomial, the number of points used to determine the polynomial, and the position in the points that the point of interpolation lies. Obviously, a polynomial of degree n requires at least $n + 1$ points. However, more points than the minimum can also be used, in which case the software is effectively filtering the input data before interpolation. A screen shot of the interpolation program is shown in Figure 5.7.

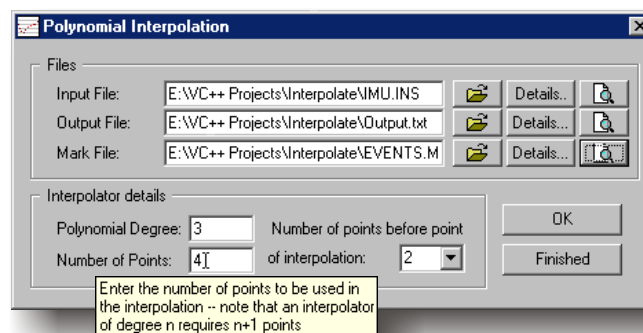


Figure 5.7: Photogrammetric Mark Interpolator

As an aside, the interpolation program can interpolate any quantity from any text

input file. Also, the format of the text files (i.e., the number of columns, starting row, etc.) can be specified for the input file and the file containing the times of interpolation.

IMU Calibration Software

The IMU calibration software, shown in Figure 5.8, was used to calibrate the accelerometers in the DMC-SX. In order to perform a calibration, the IMU must be put through a series of orthogonal rotations where each axis is approximately aligned with the gravity vector in both the up and down positions. From the data collected during these rotations the IMU calibration program automatically determines the alignment periods for each axis, corrects for misalignments of the axes with the gravity vector, and uses the corrected measurements to calibrate for the accelerometers' bias and scale errors. An iterative approach to calibration is adopted, where the biases and scale factors from one iteration are used to correct the measurements in the following iteration, and the process repeated until the change in biases is below a specified level. The IMU calibration software can also calibrate gyroscopes; however, because the DMC does not contain these sensors this functionality was not used.

To the author's knowledge, the iterative calibration algorithm that corrects for misalignment with the gravity vector has not been used before. Consequently, testing using simulated data was performed to verify that the technique resulted in accurate estimates of the bias and scale errors. The simulated data reflected what would be output from an IMU if it were put through the rotations required by the algorithm. The effect of misalignments of the IMU axes with the gravity vector were also simulated, and, for greater realism, the simulated data included second-order errors that

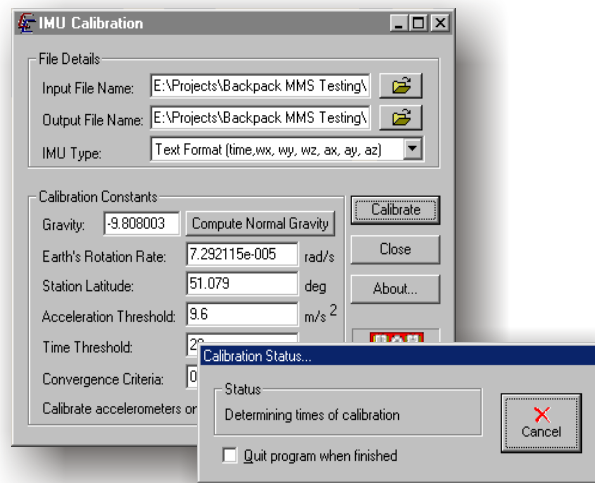


Figure 5.8: IMU Calibration Software

the algorithm cannot calibrate for.

The results from two tests using simulated data are shown in Table 5.3. In both tests the simulated bias and scale errors are representative of the errors that a good-quality MEMS-based accelerometer could be expected to have. In the first test, the simulated second-order errors cause errors between 10-30 mGal under an acceleration equal to gravity, while in the second test they cause errors between 100-200 mGal. The results from both tests confirm that the calibration algorithm is extremely effective. The bias and scale errors reported by the method are within 2% of their simulated values. Also worthy of note is that the standard deviations reported by the method are reasonable (the standard deviations are determined using full error propagation, including the effect of uncertain misalignment angles).

Table 5.3: IMU Calibration Software Testing

Axis	Simulated Values			Calibrated Values			
	<i>Bias</i> (<i>mGal</i>)	<i>Scale</i> (<i>ppm</i>)	<i>2nd order</i> ($\times 10^{-6}$)	<i>Bias</i> (<i>mGal</i>)	σ_b (<i>mGal</i>)	<i>Scale</i> (<i>ppm</i>)	σ_s (<i>ppm</i>)
<i>Noise:</i>	Normally distributed with a standard deviation of 100 mGal						
<i>x</i>	600.0	500.0	2.0	598.4	5.1	498.6	5.2
<i>y</i>	1200.0	200.0	3.0	1205.2	4.7	197.4	4.8
<i>z</i>	300.0	300.0	1.0	303.5	3.1	296.5	3.1
<i>Noise:</i>	Normally distributed with a standard deviation of 1000 mGal						
<i>x</i>	8600.0	1500.0	22.0	8653.9	25.2	1512.8	25.7
<i>y</i>	11200.0	3200.0	53.0	11254.1	23.2	3204.1	23.6
<i>z</i>	20300.0	1300.0	37.0	20339.9	15.5	1312.6	15.8

5.4 System Operation

Using the prototype backpack system, the steps required to obtain mapping space co-ordinates are as follows:

- Collect the field data – including images, GPS data, and attitude angles – using the prototype system.
- Process the GPS data using Grafnav to obtain georeferenced positions.
- Extract DMC attitude angles from the GPS data using the NovAtel log extractor.
- Interpolate positions and attitudes corresponding to the exposure times using the mark interpolator and the positions and attitude angles from the above steps
- Collect image measurements using the graphical point picker. The point picker

will output files suitable for input into the bundle adjustment, although the positions and orientations from the above steps must be manually added.

- Adjust the data using the bundle adjustment. The adjustment will output 3-D georeferenced co-ordinates.

These steps are essentially the same that a “production” backpack system would have, except that a commercial product would require the data flow to be more automated.

Chapter 6

Testing and Results

This chapter contains the results of tests done for and with the backpack MMS. The results of tests done on the individual system components are presented first, followed by the results of tests performed with the system itself.

6.1 Sensor Testing

Each sensor in the backpack MMS contributes to the overall error in the co-ordinates of the object-space points measured by the system. Consequently, it is necessary to examine the performance of each sensor in detail in order to have an appreciation of the effect of each on total system accuracy. The stability of the calibration parameters of each sensor is particularly important, as stable and systematic sensor errors can be calibrated for and eliminated.

6.1.1 Camera Calibration

An important consideration in the performance of the backpack MMS is the stability of the camera's interior orientation. Similar testing of a Kodak DC265 (a small development of the DC260) by Shortis et al. (2001) had indicated that the interior orientation stability was quite good, even under environmental stress. However, it does not necessarily follow that similar cameras, even of the same model, share the same characteristic.

The interior orientation stability of the DC260 used the backpack MMS was tested by comparing the results from three independent calibrations. The calibrations were conducted over a period of several months and in different environmental conditions. Image mensuration was performed in three different ways: twice manually by two different operators and once automatically using the ellipse target centre algorithm described in Section 5.3.2. The result of the calibrations, shown in Table 6.1, indicate the DC260 had quite good interior orientation stability. These results are particularly encouraging, given the time period between calibrations.

Table 6.1: Kodak DC-260 Interior Orientation Stability

Test Condition	Focal Length	Principal point offset		Radial distortion	
	(pixels, <i>mm</i>)	x_p (pixels, <i>mm</i>)	y_p (pixels, <i>mm</i>)	k_1 (pixels ⁻³)	k_2 (pixels ⁻⁵)
Outdoors, winter	1702.4 <i>8.26</i>	765.2 <i>3.71</i>	509.8 <i>2.47</i>	3.74×10^{-8}	-2.53×10^{-14}
Indoors	1701.9 <i>8.25</i>	768.6 <i>3.73</i>	510.9 <i>2.48</i>	2.75×10^{-8}	-1.48×10^{-14}
Outdoors, summer	1700.2 <i>8.25</i>	767.4 <i>3.72</i>	509.7 <i>2.47</i>	4.25×10^{-8}	-3.03×10^{-14}

The results of the stability testing has several consequences for the backpack MMS. The most obvious is that it confirms that the interior orientation parameters

can be held fixed in the adjustments without contributing a significant error to the co-ordinates of the object space points. For example, the radial difference in image co-ordinates that results from using the different principal point offsets and radial distortion parameters in Table 6.1 is less than 2 pixels at the edge of the image format. At an camera-to-object distance of 30 m this corresponds to a pointing error of less than 2 cm, which is an order of magnitude less than the desired accuracy of the backpack MMS. An alternative to the above approach of holding the interior orientation parameters fixed is to treat them as parameters with the appropriate parameter observations. If such an approach is followed, then the differences between similar parameters in Table 6.1 can give an idea of both the values and weights of the parameter observations.

It is also interesting to compare the interior orientation of the DC260 used in the backpack MMS with the interior orientations of another DC260. Results from another DC260 were available from the website of ISPRS Working Group V/2. Their DC260 had a focal length of 8.42 mm and principal point offsets of 3.90 mm and 2.57 mm in the x and y directions, respectively (El-Hakim, 2001). These results are somewhat in agreement with the results in Table 6.1. Nevertheless, the differences are large enough to suggest that different DC260 cameras could not use the same calibration parameters. It should be noted that the DC260 of Working Group V/2 was also calibrated for decentring distortion, affinity and shear, and the addition of these parameters may partially explain the difference in the principal point offsets. However, the inclusion of these parameters cannot explain the difference in focal lengths.

In addition to examining the stability of the DC260's interior orientation, it is

worth commenting on the individual parameters of interior orientation. In particular, the closeness of the calibrated principal point with the indicated principal point (i.e., the centre of the image) is surprising. Indeed, the maximum difference between the two points is under 4 pixels, and for the desired accuracies of the backpack MMS it is arguable whether it is necessary to use the calibrated principal point at all. The same, however, cannot be said of the radial distortion parameters. Figure 6.1 is the radial distortion curve of the DC260. From this figure it can be seen that the radial error in image co-ordinates can exceed 10 pixels at the edge of the image. This error is too large to safely ignore – especially if the indicated principal point is used in place of the calibrated principal point.

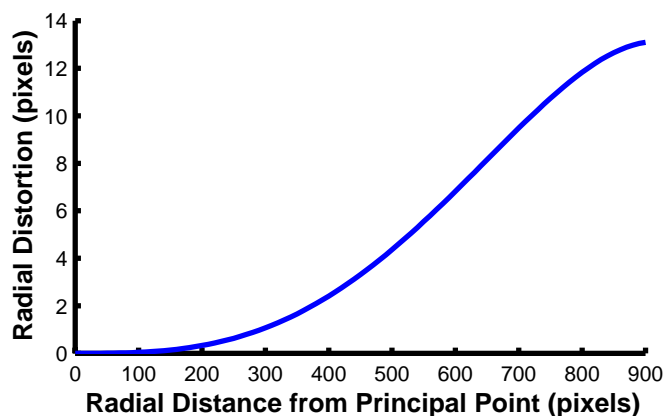


Figure 6.1: DC260 Symmetric Radial Distortion Profile

6.1.2 DMC Accelerometer Testing

For the Leica DMC-SX, testing was only performed after the prototype backpack MMS had been tested and disassembled. Consequently, the results of the testing

were not used to improve the performance of the system. Additionally, testing was performed exclusively on the DMC's accelerometers. Testing of the DMC's magnetometers was not performed because of the difficulties in devising a suitable test. Essentially, it is impossible to test the device indoors because of the inevitable presence of magnetic disturbances. Testing the azimuth performance of the DMC by comparing its output with the output from another device is also difficult because the other device almost certainly has its own electrical and magnetic fields that disturb the magnetic field.

The effect of erroneous accelerometer measurements on the roll and pitch angles can be determined by performing an error analysis on Equations (4.1) and (4.2). If the accelerometer is level, then the angular error resulting from incorrect x and y -axis measurements can be approximated by

$$\delta\theta = \frac{\delta f}{f_z}, \quad (6.1)$$

where $\delta\theta$ is the angular error in radians, and δf is the error on either the x or y -axes. Similarly, the angular error because of erroneous z -axis measurements is approximately

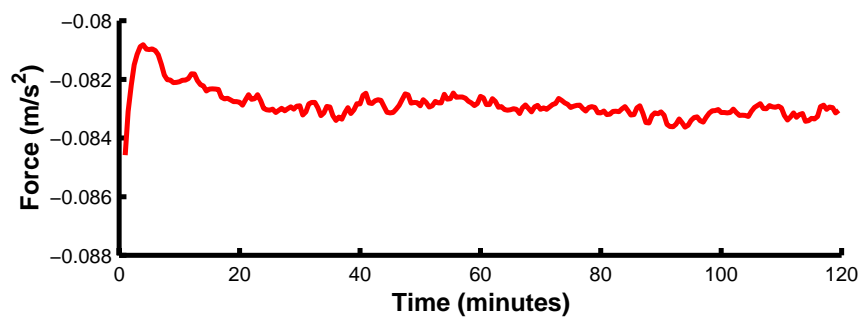
$$\delta\theta = -\frac{\delta f_z}{f_z^2}. \quad (6.2)$$

The first characteristic of the DMC's accelerometers that was tested was the dependance of their output on temperature. The relation between accelerometer performance and temperature is well-known, and previous testing of similar MEMS-based accelerometers by the author had shown that even the internal heat generated

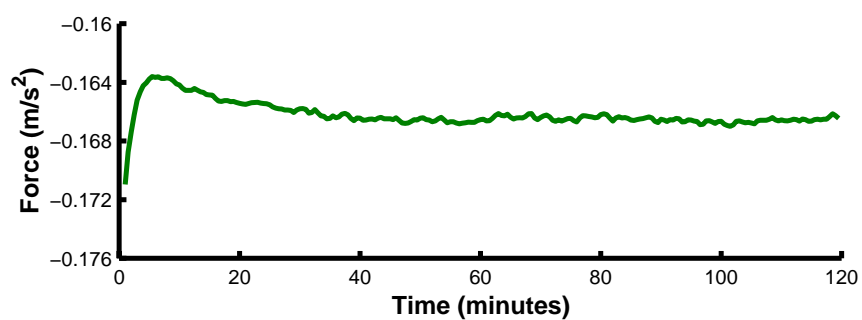
by the device around the accelerometers could cause significant changes in their measurements (Ellum, 2000). Consequently, it was expected that the same effect would be observed in the DMC.

The dependence of accelerometer output on temperature was confirmed by observing the output from the DMC during a two-hour static warm-up test. Figure 6.2, shows the change in accelerometer measurements of the DMC during this test. One minute averages of the data, which was collected at 5 Hz, have been used. For the x and y -axis accelerometers a ramp in the output of about 200 mGal can clearly be seen in the initial 5 or 10 minutes after the power is applied to the device. After this increase, there is a slight “bounce-back” until, at approximately 30 minutes, the output has stabilised. For the z -axis accelerometer, the opposite effect can be seen. The output for the z -axis accelerometer shows a much more gradual change, but one that does not stabilise until about 90 minutes after power-up. In addition, the absolute change in the z -axis accelerometer measurements is an order magnitude greater than that of the x and y -axis accelerometers – nearly 2000 mGal in this test.

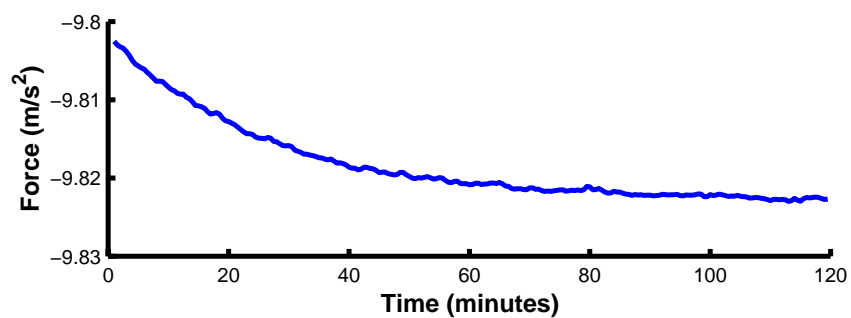
During the initial period of large output changes in the x -axis and y -axis accelerometers, the temperature of the DMC – measured by its internal thermometer – increased by approximately 2 degrees from 23°C to 25°C. This confirms the effect of temperature changes on the DMC’s accelerometers and suggests that the device should be allowed to warm-up for a period of at least 30 minutes before it is used. The more gradual change witnessed in the z -axis accelerometer’s measurements after the initial temperature increase is also likely due to temperature changes. Unfortunately, the internal temperature sensor of the DMC only has a resolution of 1 degree; consequently, it was not possible to detect temperature changes after the initial 30



(a) x-axis



(b) y-axis



(c) z-axis

Figure 6.2: DMC-SX Accelerometer Measurements during Warm-Up

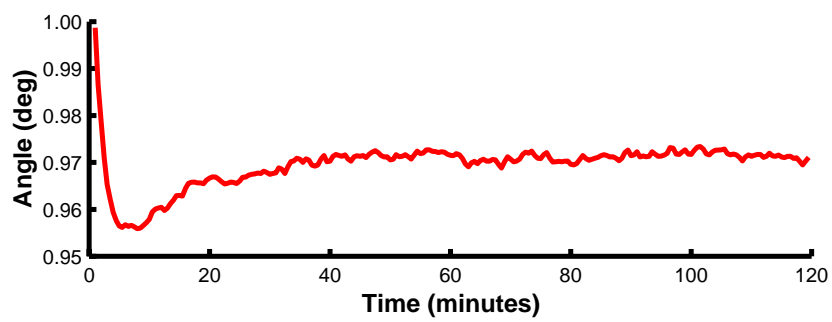
minutes.

It should be noted that multiple warm-up tests were performed, and the results – including the initial ramp in output and subsequent bounce-back – in all cases agreed with the results in Figure 6.2.

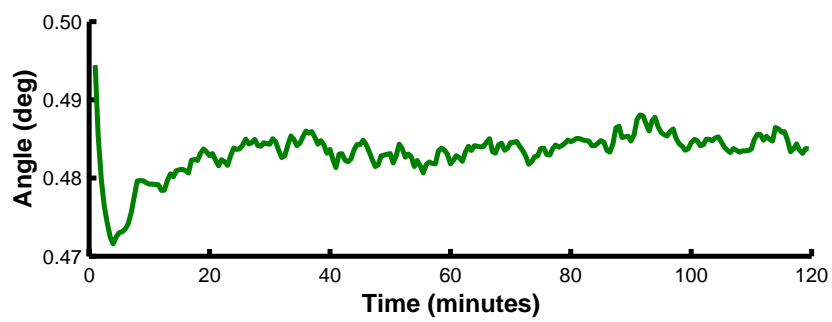
Temperature-dependant changes in the output from the individual accelerometers do not necessarily result in changes in the derived roll and pitch angles. If the ratio of the changes is unity, then the angle calculation of Equations (4.1) and (4.2) will be unaffected. However, in order to have no change in the ratio of the accelerometer measurements, temperature must have an equivalent effect on the scale errors of each accelerometer. Also, it must not change the accelerometer biases. Unfortunately, the different trends in visible in Figure 6.2 mean that in the DMC, one or both of these conditions is not met.

Figure 6.3 shows the change in the roll and pitch angles output by the DMC during the same period as that shown in Figure 6.2. During the initial 20 minutes the roll and pitch angles change by over 0.4° and 0.2° , respectively. In addition to confirming the change in the ratio of accelerometer outputs, this angular change also confirms that either the DMC doesn't perform temperature compensation on its measurements, or that the temperature compensation is ineffective. In either case, Figure 6.3 reaffirms that the data from the DMC should not be used until after an initial warm-up period of 30 minutes.

An even more vivid demonstration of the effect of temperature on the angles measured by the DMC is visible in Figure 6.4. The data in this figure was collected while the DMC was being rapidly cooled and rapidly heated. A clear (although not necessarily linear) link between the changes in temperature and changes in the



(a) Roll



(b) Pitch

Figure 6.3: DMC-SX Angular Measurements during Warm-Up

angular measurements is visible.

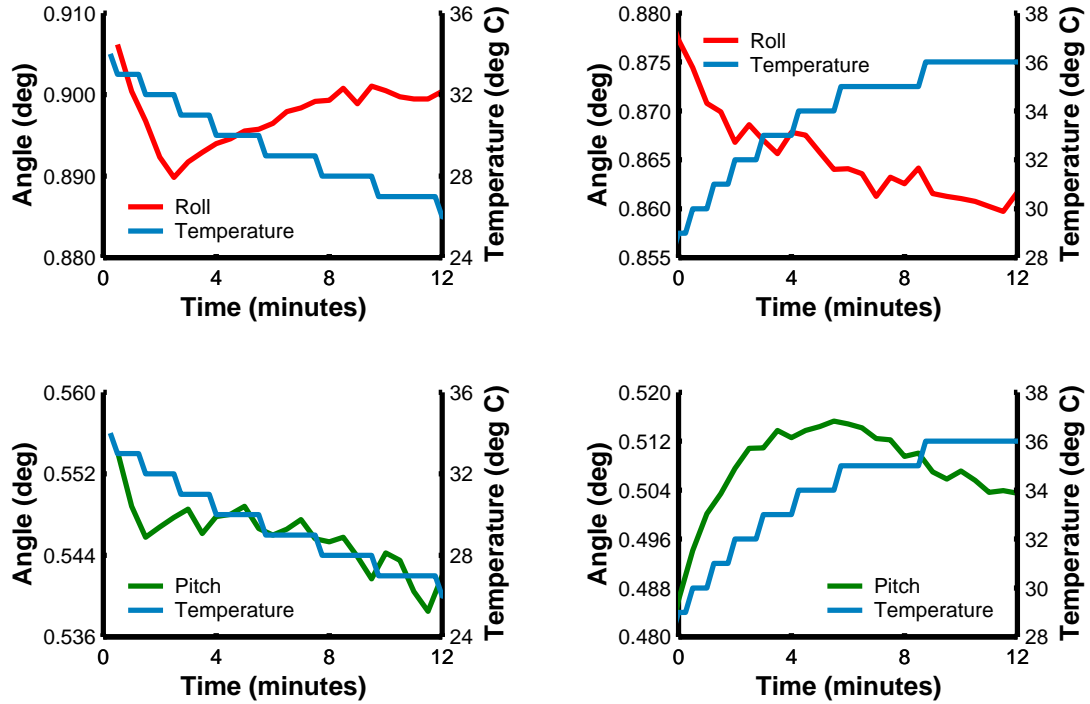


Figure 6.4: DMC Angular Change During Cooling and Heating

The second characteristic of the DMC's accelerometers that was examined was their bias and scale errors. This was done by performing repeated accelerometer calibrations using the IMU calibration software described in Section 5.3.3 over a period of approximately a month and a half. The results of these calibrations are shown in Table 6.2. At first glance, the size of both the bias and scale errors is alarming – particularly for the z -axis accelerometer. However, if the DMC is approximately level then the bias and scale errors will nearly entirely cancel each other out on the z -axis. Consequently, ignoring these errors will result in a measurement error of only about 2000 mGal. Using Equation (6.2) it can be seen that this would cause errors

in roll and pitch of less than 0.02° , which can safely be ignored. The error caused by ignoring the x and y -axis bias and scale errors is an order of magnitude larger than this – approximately 0.2° – but even this could likely be ignored in the backpack MMS providing the angular measurements are appropriately weighted in the bundle adjustment. As a note, the errors on the x and y -axis accelerometers essentially indicate that the 0.15° accuracies in roll and pitch claimed by Leica are somewhat optimistic.

Table 6.2: DMC Accelerometer Calibration

Date of Calibration	x-axis		y-axis		z-axis	
	<i>bias</i>	<i>scale</i>	<i>bias</i>	<i>scale</i>	<i>bias</i>	<i>scale</i>
<i>Dec. 9, 2001</i>	528.60	-343.56	1466.13	255.66	-32436.28	-31943.01
<i>Nov. 20, 2000</i>	649.43	-293.95	1592.67	599.60	-36444.45	-35462.15
<i>Nov. 20, 2000</i>	654.50	-253.54	1602.40	562.56	-35757.41	-34791.35
<i>Nov. 21, 2000</i>	916.97	-385.73	1579.14	524.07	-34008.61	-33118.32
<i>Nov. 22, 2000</i>	1047.91	-319.07	1958.92	532.07	-35196.59	-34147.12
<i>Average</i>	759.48	-319.17	1639.85	494.79	-34768.67	-33892.39
<i>Std Dev</i>	214.73	49.92	186.61	136.94	1580.09	1390.72
<i>Max</i>	1047.91	-253.54	1958.92	599.60	-32436.28	-31943.01
<i>Min</i>	528.60	-385.73	1466.13	255.66	-36444.45	-35462.15
<i>Range</i>	519.31	132.19	492.79	343.94	4008.17	3519.14

Units: *bias* – mGal (10^{-5} m/s²) *scale* – ppm

In spite of the conclusions above it is obviously better when possible to correct the accelerometer measurements for bias and scale errors. The information in Table 6.2 indicates that for the accelerometers in the DMC neither error is particularly stable. However, even using mean values of the errors would reduce the angular error to less than 0.05° .

As an aside the large scale error in the z -axis accelerometer puts into doubt the assumption that there are no significant second-order and higher errors. Unfortu-

nately, the presence of these errors could not be tested for by using the algorithm in the IMU calibration software.

6.2 Proof-of-concept Testing

The proof-of-concept testing was performed to verify that a backpack MMS could attain the desired 0.2 metre (RMS) horizontal and 0.2 metre (RMS) vertical accuracies. Because the testing was very preliminary time tagging of the various data streams was done by hand.

6.2.1 Test Field

Testing of the backpack MMS necessitated the establishment of a suitable target field that would simulate a “typical” urban environment in which the system would be expected to operate. The field that was established, shown in Figure 6.5, was approximately 30 metres wide and 10 metres in depth. For ease of calculation, a local level co-ordinate frame was established. In this co-ordinate system, the easting axis was roughly aligned with the depth of the target field, and the northing axis was roughly aligned with the width of the target field. The target field had nearby vertical structures, pavement, and foliage – in short, somewhat of a “worst-case” environment for GPS (excepting complete satellite masking, of course). It also had nearby metal buildings and light standards that could influence the azimuth reported by the DMC.

The target field was initially surveyed and adjusted using GPS baselines, EDM distances, and horizontal & vertical angles. However, to further increase the accuracy

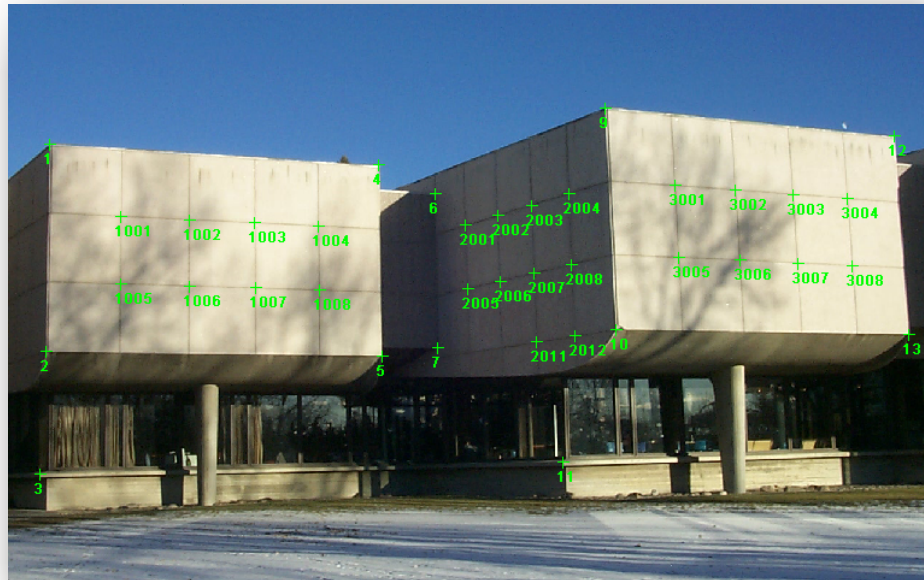


Figure 6.5: First Test Field - Photo

of the surveyed points, and to most accurately determine the exterior orientations of the test images, the measurements from all the images used in the tests were also included in an combined photogrammetric/terrestrial adjustment. Additionally, the interior orientation and lens distortion parameters of the camera were calibrated simultaneously, although results from a previous calibration were included as weighted parameters. The combined network, shown in Figure 6.6, had a redundancy of over 1500, and the reported standard deviations for the object space co-ordinates of both the target points and exposure station positions were under a millimetre. The attitudes of the exposure stations had standard deviations that were largely under $1'$. The positions and orientations calculated in the combined photogrammetric/terrestrial adjustment were treated as the “true” quantities in all

the comparisons in the following sections. The residual error that remains was neglected, as its relative magnitude was below the centimetre level that the results were compared at. The initial terrestrial network adjustment, the combined adjustment, and the individual photogrammetric adjustments done for the tests were all performed using the bundle adjustment package described in Section 5.3.1.

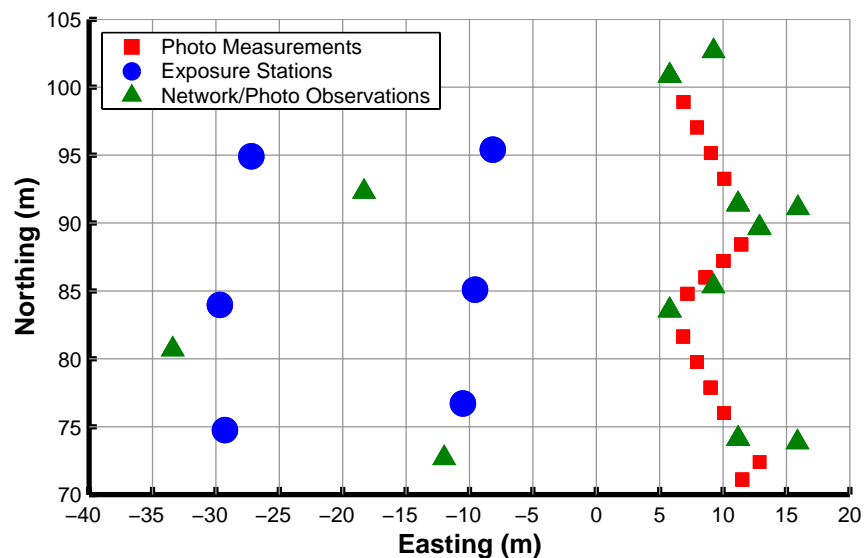


Figure 6.6: First Test Field

The images for the tests were taken at object to camera distances of approximately 20m and 40m – hereafter referred to as the “near” and “far” images, respectively. Initially, two images were captured at each of six image stations - 3 near and 3 far. In the description of the tests, images 1 through 6 are the near images and images 7 through 12 are the far images. In all cases, the azimuths from the DMC have first been corrected for magnetic declination using the Geological Survey of Canada’s Magnetic Information Retrieval Program (MIRP) (Geological Survey of Canada (GSC), 2000).

6.2.2 Navigation Sensor Accuracy

Tables 6.3 and 6.4 shows the agreement between the measured GPS positions and the camera positions determined from the combined photogrammetric/terrestrial adjustment. The results show that the test environment was indeed sub-optimal, as the results are significantly worse than expected – especially considering that the master to remote separation never exceeded 150m and the number of satellites never fell below 6. It is believed that multipath off the nearby buildings is the cause of the poor accuracies. Carrier phase results for images 4 through 6 are significantly worse than the others because of a loss of satellite lock after the second image; thus, these differences were not included in the statistics. This loss of lock illustrates that – for urban environments, at least – Real-Time Kinematic (RTK) GPS may be more of a necessity than a luxury. This is because despite the extreme care taken during these tests to avoid losing lock, loss of lock still occurred. Such an occurrence would likely befall any user in a similar environment, and only with RTK could the approximate accuracies be reliably maintained. It is also worth noting that in the environment that the test was performed in a code differential solution is clearly far too inadequate for even the crudest mapping applications.

The differences between the attitude angles measured by the DMC and the true attitude angles are shown in Figure 6.7 and Table 6.5. For this test, the DMC attitude angles were collected at approximately 10 Hz. At this sampling frequency, the measurements are moderately noisy – particularly the azimuth, which can vary over several degrees. Therefore, to remove some of this noise one-second averages of the DMC data were used. This improved the RMSE of the roll and pitch angles by approximately 8 arc-minutes, and the azimuth angles by over half a degree. It is

Table 6.3: L1/L2 Carrier Phase Differential GPS Position Differences
(Proof-of-Concept Test)

Exposure Number	Co-ordinate Differences (m)			Distance Differences (m)
	<i>Easting</i>	<i>Northing</i>	<i>Elevation</i>	
1	-0.025	0.065	0.024	0.074
2	-0.022	0.079	0.005	0.082
3*	-0.600	-0.895	-2.699	2.906
4*	-0.185	0.451	-1.871	1.934
5*	-0.723	-0.621	-1.870	2.099
6*	-0.695	-1.052	-1.617	2.050
7	-0.075	-0.090	0.045	0.126
8	-0.071	-0.031	0.061	0.099
9	-0.111	-0.002	0.049	0.121
10	-0.071	-0.084	0.019	0.112
11	-0.106	0.010	0.054	0.119
12	-0.073	0.073	0.041	0.111
Average	<i>-0.069</i>	<i>0.002</i>	<i>0.037</i>	<i>0.105</i>
RMSE	<i>0.075</i>	<i>0.060</i>	<i>0.041</i>	<i>0.107</i>

* - Satellite lock lost, not included in carrier phase averages

felt that this is a reasonable time period, as the backpack MMS must be held steady for at least this period in order to capture the image. The results in Table 6.5 are the differences after the mean has been removed from the differences between the DMC angles and the true angles. This was done because the proof-of-concept testing did not require a full calibration of the integrated system, and the average angular differences were used as an estimate of the misalignment between the camera axes and the DMC axes. Of course, simply removing the mean will result in an overly-optimistic estimate of the angular errors – particularly for the azimuth as it will also compensate for both deficiencies in the magnetic declination model and local variations of the magnetic field; however, it provides a good idea of what sort of accuracies can be achieved in the most favourable case (although the mean of the

Table 6.4: C/A Code Differential GPS Position Differences
(Proof-of-Concept Test)

Exposure Number	Co-ordinate Differences (m)			Distance Differences (m)
	<i>Easting</i>	<i>Northing</i>	<i>Elevation</i>	
1	0.919	-0.685	-0.624	1.305
2	0.884	-2.528	-4.429	5.176
3	-1.288	-1.421	-3.284	3.803
4	-0.972	-2.134	-6.286	6.709
5	-1.185	-0.537	-2.003	2.388
6	-0.497	-0.761	-1.131	1.450
7	-4.245	-1.476	-8.128	9.288
8	-0.406	-0.261	2.478	2.524
9	0.075	-2.291	-2.033	3.064
10	0.693	-0.057	-2.636	2.727
11	1.125	-0.268	-0.800	1.407
12	1.889	1.038	-2.049	2.974
Average	<i>0.117</i>	<i>-0.816</i>	<i>-2.278</i>	<i>3.558</i>
RMSE	<i>1.504</i>	<i>1.348</i>	<i>3.605</i>	<i>4.194</i>

azimuth differences was the smallest of the three angles prior to removal). Finally, it should be noted that the DMC was not calibrated for either hardmagnetic or softmagnetic disturbances, and the azimuth angle results in Table 6.5 would certainly be improved by either such calibration.

The agreement between the measured angles and the true angles in Table 6.5 is generally good. However, there is a notable and surprising decline in accuracy for the azimuths of the final four exposure stations. A possible explanation was the proximity of a nearby electric light standard and metal building, but it was felt that these objects could not disturb the magnetic field to the extent visible in Table 6.5. Thus, the results were checked by capturing additional images at approximately the same positions as the final six images from the first data set (i.e., the far images).

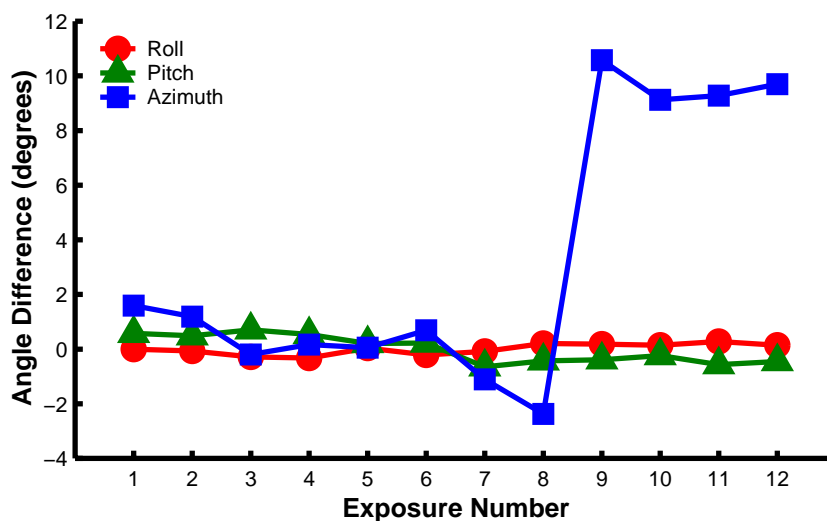


Figure 6.7: DMC/Combined Adjustment Angle Differences

For this second set of images the internal data integration time of the DMC was changed so that measurements were collected at 1 Hz. Unfortunately, GPS was not available for these images, and because the DMC was remounted, new angular difference averages were calculated and again used in lieu of a rigorous calibration.

The azimuth differences for the new photos – shown in Figure 6.8 and Table 6.6 – are significantly smaller than the differences for the previous photographs taken at the exposure stations. The cause of the azimuth errors in the first set of images is unknown; however, one possibility may be that the power cable for the camera was allowed to come too close to the DMC.

6.2.3 Mapping Accuracy

Because of the loss of satellite lock discussed in Section 6.2.2, it was not possible to use the differential carrier phase GPS positions for the final four exposures of

Table 6.5: DMC Attitude Angle Differences
(Proof-of-Concept Test)

Exposure Number	Angle Differences (°)		
	<i>Roll</i>	<i>Pitch</i>	<i>Azimuth</i>
1	-0.006	0.580	1.591
2	-0.067	0.490	1.185
3	-0.290	0.704	-0.201
4	-0.326	0.534	0.166
5	0.040	0.202	0.054
6	-0.211	0.224	0.690
7	-0.083	-0.648	-1.109
8	0.202	-0.433	-2.376
9	0.181	-0.394	10.574
10	0.138	-0.240	9.125
11	0.280	-0.564	9.279
12	0.142	-0.455	9.693
RMSE	<i>0.191</i>	<i>0.482</i>	<i>5.675</i>

the near exposure stations. Therefore, the positions from the combined photogrammetric/terrestrial adjustment were used instead. To simulate the effect of positional errors, the co-ordinate errors from the equivalent far stations were added to the exposure station positions. Also, the erroneous DMC angles for the initial far images meant that no adjustment would converge for these images. Thus, the second set of far images – with the correct DMC angles – were used instead. Like the near stations, positional errors were simulated by adding the co-ordinate errors from the first set of far stations. For all of the following tests the interior orientation parameters determined in the combined terrestrial/photogrammetric adjustment were used.

The object space accuracies when the near images were used are shown in Table 6.7. For the first two tests in the table the six close images were divided into two sets of three images – set ‘A’ was composed of images 1, 3, and 5, while set ‘B’

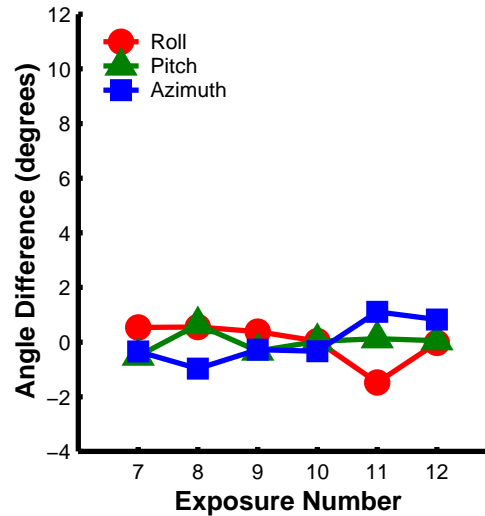


Figure 6.8: DMC/Combined Adjustment Angle Differences - Second Set of Far Images

was composed of images 2, 4, and 6. Not surprisingly, the most obvious trend in Table 6.7 is an increase in absolute object space accuracy as the number of image points included in the bundle adjustment increases. However, even with as few as five points, accuracies are comparable with typical L1 carrier phase GPS accuracies. As stated in the research objectives, this accuracy was something of a benchmark, as such single frequency receivers are widely used for GIS data collection. Of course, the backpack MMS is able to achieve this accuracy with a much greater data collection efficiency.

Unfortunately, the encouraging results for the near images are somewhat offset by disappointing results for the far images. These results, shown in Table 6.8, indicate absolute object space accuracies at the metre level. This degradation in performance for the far images has two sources:

- *Poor imaging geometry* – Due to an unfortunate oversight, the exposure sta-

Table 6.6: Revised DMC Attitude Angle Differences
(Proof-of-Concept Test)

Exposure Number	Angle Differences (°)		
	<i>Roll</i>	<i>Pitch</i>	<i>Azimuth</i>
7	0.533	-0.510	-0.346
8	0.555	0.637	-0.973
9	0.383	-0.328	-0.277
10	0.035	0.026	-0.333
11	-1.474	0.122	1.105
12	-0.031	0.053	0.824
RMSE	<i>0.697</i>	<i>0.363</i>	<i>0.725</i>

tions for this test were nearly collinear. In this arrangement, the entire network is essentially free to swing about the axis formed by the exposure stations with only the roll and pitch angles from the DMC constraining the rotation. The poor imaging geometry also explains why the elevation accuracy does not improve as more points are added to the adjustment – unlike the horizontal accuracy.

- *Poor image point measurements* – At the larger camera-to-object distances, the resolution of the images was not high enough to permit very accurate image point measurements. This problem was compounded by the poor contrast in the areas where the points were being selected.

The potential existence of poor image measurements highlights an additional problem – that of blunder detection. Obviously, in photogrammetric networks as redundancy decreases this becomes progressively more difficult. For some users of the backpack MMS, low redundancy will be the norm and not the exception. In these cases, the graphical image measurement software can help in both the prevention and detection

Table 6.7: Results (Approximate Camera to Object Point Distance = 20 m)

	Image measure- ments	Statistics of Co-ordinate Differences (m)					
		Horizontal			Vertical		
		<i>Mean</i>	<i>Std. Dev.</i>	<i>RMSE</i>	<i>Mean</i>	<i>Std. Dev.</i>	<i>RMSE</i>
Three Images (“A” <i>images</i>)	1	0.42	-	0.42	-0.07	-	0.07
	2	0.14	0.07	0.15	-0.04	0.02	0.04
	5	0.10	0.03	0.10	-0.06	0.02	0.06
	10	0.10	0.02	0.10	-0.06	0.03	0.07
Three Images (“B” <i>images</i>)	1	0.04	-	0.04	-0.15	-	0.15
	2	0.12	0.10	0.14	-0.14	0.07	0.15
	5	0.04	0.03	0.05	-0.15	0.03	0.15
	10	0.06	0.03	0.07	-0.16	0.04	0.16
Six Images	1	0.21	-	0.21	-0.11	-	0.11
	2	0.08	0.03	0.08	-0.09	0.05	0.10
	5	0.05	0.01	0.05	-0.11	0.03	0.11
	10	0.05	0.01	0.05	-0.11	0.03	0.11

of errors. For example, the display of epipolar lines will help prevent blunders during image point mensuration, while the back-projection of the adjusted object-space points will help in the detection of any poor measurements.

For both the near and the far images, it can be observed that the mean of the differences is nearly as large as the RMS error. This indicates that the relative accuracy of the object points is much better than their absolute accuracy. This is confirmed by the standard deviations of the co-ordinate errors, which indicate that the internal agreement of the object space co-ordinates is at approximately 5 cm for the near images and 10 cm for the far images. It is acknowledge that absolute accuracies are of primary importance for most mapping and GIS applications. However, relative accuracies still have importance in cadastral and engineering surveys - examples include small-scale facilities mapping and surveys for earthwork volume

Table 6.8: Results (Approximate Camera to Object Point Distance = 40 m)

	Image measure- ments	Statistics of Co-ordinate Differences (m)					
		Horizontal			Vertical		
		<i>Mean</i>	<i>Std. Dev.</i>	<i>RMSE</i>	<i>Mean</i>	<i>Std. Dev.</i>	<i>RMSE</i>
Three Images	1	2.57	-	2.57	0.34	-	0.34
	2	1.89	0.24	1.90	0.76	0.44	0.82
	5	0.68	0.14	0.69	0.77	0.12	0.78
	10	0.33	0.11	0.35	0.78	0.08	0.78
	20	0.29	0.09	0.30	0.79	0.06	0.79
	30	0.30	0.08	0.31	0.80	0.06	0.80
Six Images	1	2.85	-	2.85	0.08	-	0.08
	2	2.13	0.37	2.15	0.58	0.49	0.68
	5	0.68	0.12	0.69	0.58	0.12	0.59
	10	0.37	0.09	0.38	0.58	0.09	0.59
	20	0.32	0.07	0.32	0.59	0.07	0.59
	30	0.31	0.06	0.31	0.59	0.06	0.59

computations.

The objective of the backpack MMS is to produce co-ordinates without any external measurements – i.e., with no control points. However, this does not preclude the use of additional information that may be available in the images such as objects of known dimension or a known geometry between points. The former information – in the form of distance constraints – should improve the scale of the photogrammetric networks measured from the backpack MMS’s images. Similarly, the latter information – in the form of vertical line constraints or zero-height constraints – should help with the orientation of the networks. Unfortunately, for the backpack MMS, the effects of including such information were not always positive. Indeed, for the tests in Table 6.9 the additional information was equally as likely to degrade the solution as it was to improve it. A possible explanation is that the additional information improves the internal consistency of the network, but it also causes the

entire network to shift. An exaggerated example of this effect is shown in Figure 6.9.

Table 6.9: Effect of Including Control or Network Observations
(3 images, 10 image points, far images)

Type of Information Added	Statistics of Co-ordinate Differences (m)					
	Horizontal			Vertical		
	Mean	Std. Dev.	RMSE	Mean	Std. Dev.	RMSE
None	0.33	0.11	0.35	0.78	0.08	0.78
Horizontal Distance	0.42	0.12	0.44	0.75	0.06	0.76
Vertical Distance	0.29	0.11	0.31	0.76	0.06	0.76
Height Constraints	0.30	0.08	0.31	0.44	0.05	0.44
One Control Point	0.12	0.07	0.14	0.28	0.04	0.29

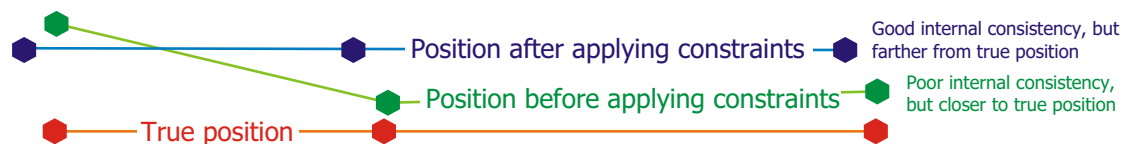


Figure 6.9: Possible Result of Including Extra Constraints in Adjustment

It should be noted that the results from this system are not indicative of the value of additional information. In general, including additional information in an adjustment – providing the information is “good” – will improve results.

Table 6.9 also demonstrates the obvious improvement in both absolute and relative accuracy that results from including a control point in the adjustment. One potential mode of operation of the backpack MMS is to have it mounted on a survey stick. In this case, using the GPS the MMS itself could be used to establish control points in a region. These points, in turn, could then be used in the adjustment to improve absolute accuracy. In other words, a user would occupy points with the survey stick mounted MMS, and then include those GPS points in the adjustment – providing, of course, that the points appear in the images.

6.3 Prototype System Testing

The proof-of-concept testing had demonstrated that a backpack MMS could achieve the desired accuracies. However, because of the problems encountered during the test (i.e., loss of satellite lock, poor DMC angles) another test was required. This second test took place with the fully assembled prototype system.

Three tests were performed with the prototype testing. Unfortunately, the testing, like the proof-of-concept testing, was plagued with problems. The most significant problem was that the camera had been rotated (primarily along its vertical axis) with respect to the DMC between the first and second tests. This movement was not discovered until after the completion of the testing. This problem could have been overcome had boresight calibrations been performed before and after the tests. However, a suitable target field could be found for performing such a test. An attempt was made to perform such a test using a target field in the loading bay at the rear of the Engineering complex. Unfortunately, the large magnetic disturbances in the region meant a successful calibration was impossible.

6.3.1 Test Field

The target field used in the proof-of-concept testing was not available for the second test. Consequently, it was necessary to establish and measure a second target field. Again, an area was selected that would simulate a typical urban environment, and again the target field was surveyed using a combination of GPS baselines, EDM distances, and horizontal & vertical angles. The image measurements from the three tests of the prototype backpack MMS were also included, as were weighted parameter

observations of the DC260's interior orientation. The complete adjustment of the target field had a redundancy of close to 500, and the reported standard deviations of the target co-ordinates were around 1 cm. The exterior orientations of the cameras resulting from the adjustment are used in the comparisons of Section 6.3.2.

At one point during the prototype testing, it was suspected that there could be errors in the target field co-ordinates. To ensure that this was not the case the co-ordinates of the target field were checked in two different ways. First, new measurements were taken that provided a direct check on several of the target co-ordinates. Second, the adjustment with the original data was performed using another program. Both checks agreed with the co-ordinates from the original adjustment with the original set of measurements.

The target field for the prototype testing is shown below in Figures 6.10 and 6.11. The total field is approximately 35 metres wide and 15 metres in depth, although the portion that was used during testing was approximately two thirds of these dimensions. For all tests the average distance between the exposure stations and object space points was approximately 40 metres.

6.3.2 Navigation Sensor Accuracy

Tables 6.10 through 6.12 show the difference between the measured GPS positions and the camera positions determined from the combined photogrammetric/terrestrial adjustment. The most notable observation from these tables is the similarities between the mean co-ordinate differences. An obvious source of these biases is erroneous target field co-ordinates. However, as stated in Section 6.3.1 this possibility was examined and rejected. Other possible sources include an incorrectly measured offset



Figure 6.10: Second Test Field - Photo

to the GPS antenna or the incorrect inclusion of the offset in the bundle adjustment. Both possibilities were also checked and rejected.

Another possible reason for the biases was an inaccurate interior orientation in the target field adjustment used to generate the reference exterior orientations. This possibility is more difficult to reject. Essentially, the only way to check the interior orientation parameters is to treat them as unknown in the target field adjustment. When this was done, however, the resulting RMS errors were as large as the previous errors, and the parameters of the DC260's interior orientation output by the adjustment did not agree with previously determined values. Given the apparent stability of DC260's interior orientation it was felt that the new parameters of interior orientation were not realistic. Rather, they were the result of projective compensation

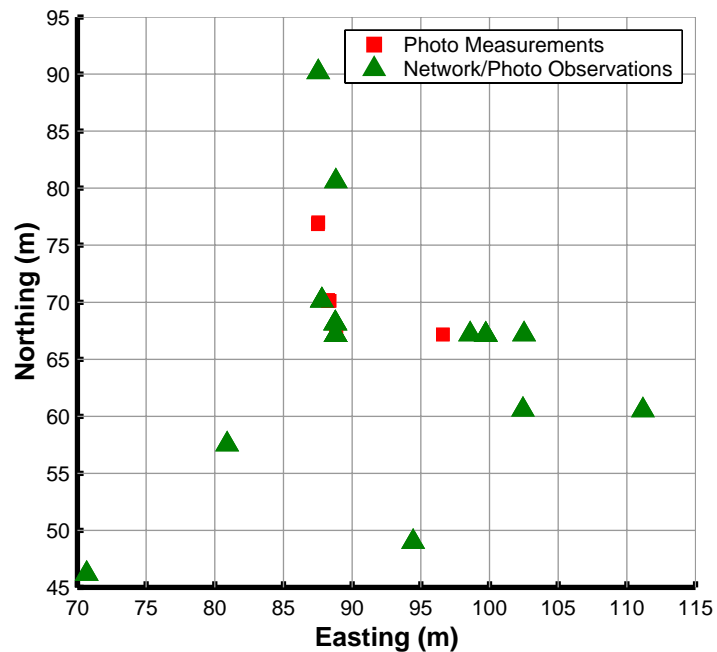


Figure 6.11: Second Test Field

with the parameters of exterior orientation.

In light of the above examinations, all that can be said is that the source of the biases is not known. Its presence, however, suggests that the RMS errors in Tables 6.10 through 6.12 may not entirely be representative of the GPS accuracies.

The dominant source of error in the GPS positions is almost certainly multipath. The short baseline between the base GPS station and the backpack MMS means that virtually all atmospheric errors are cancelled out when the GPS measurements are differenced.

The differences between the attitude angles measured by the DMC and the reference attitude are shown in Tables 6.13 through 6.14. As explained in Section 6.3 the camera was mistakenly rotated with respect to the DMC between the first and sec-

Table 6.10: L1/L2 Carrier Phase Differential GPS Position Differences - Test 1
(Prototype System Testing)

Exposure Number	Co-ordinate Differences (m)			Distance Differences (m)
	<i>Easting</i>	<i>Northing</i>	<i>Elevation</i>	
1	0.015	0.070	-0.017	0.074
2	0.069	-0.040	-0.075	0.109
3	0.039	0.072	-0.113	0.140
4	0.021	0.041	-0.073	0.086
5	0.068	-0.032	0.038	0.084
Average	<i>0.042</i>	<i>0.022</i>	<i>-0.048</i>	<i>0.099</i>
Std. dev.	<i>0.025</i>	<i>0.055</i>	<i>0.059</i>	<i>0.026</i>
RMSE	<i>0.048</i>	<i>0.054</i>	<i>0.071</i>	<i>0.101</i>

Table 6.11: L1/L2 Carrier Phase Differential GPS Position Differences - Test 2
(Prototype System Testing)

Exposure Number	Co-ordinate Differences (m)			Distance Differences (m)
	<i>Easting</i>	<i>Northing</i>	<i>Elevation</i>	
1	0.058	0.051	-0.037	0.086
2	0.028	0.052	0.017	0.061
3	0.062	0.008	-0.010	0.063
4	0.156	-0.017	-0.010	0.157
5	0.106	0.088	-0.072	0.155
6	0.054	0.072	-0.002	0.090
7	0.058	0.053	-0.078	0.111
Average	<i>0.075</i>	<i>0.044</i>	<i>-0.027</i>	<i>0.103</i>
Std. dev.	<i>0.039</i>	<i>0.034</i>	<i>0.034</i>	<i>0.037</i>
RMSE	<i>0.083</i>	<i>0.054</i>	<i>0.042</i>	<i>0.109</i>

Table 6.12: L1/L2 Carrier Phase Differential GPS Position Differences - Test 3
(Prototype System Testing)

Exposure Number	Co-ordinate Differences (m)			Distance Differences (m)
	<i>Easting</i>	<i>Northing</i>	<i>Elevation</i>	
1	0.094	0.057	-0.045	0.119
2	0.031	0.069	0.006	0.076
3	0.061	0.091	-0.015	0.111
4	0.059	0.010	-0.005	0.060
5	0.053	0.048	-0.004	0.072
6	0.151	0.047	-0.101	0.188
7	0.014	0.086	-0.073	0.114
8	0.085	-0.025	-0.035	0.095
9	0.001	0.015	0.054	0.056
10	0.054	0.087	-0.030	0.107
11	0.046	0.062	-0.018	0.079
12	0.087	0.002	0.005	0.087
Average	<i>0.061</i>	<i>0.046</i>	<i>-0.022</i>	<i>0.097</i>
Std. dev.	<i>0.040</i>	<i>0.037</i>	<i>0.040</i>	<i>0.035</i>
RMSE	<i>0.072</i>	<i>0.058</i>	<i>0.044</i>	<i>0.103</i>

ond tests. This rotation resulted in the large mean azimuth difference for the second and third tests, and this large mean difference means that the RMS errors in Tables 6.13 through 6.14 are not a true reflection of the DMC's performance. Rather, the standard deviations give a more accurate idea of the accuracies of the DMC's angles.

The standard deviations in Tables 6.13 through 6.14 do not agree with the accuracies stated by the manufacturer of the DMC (see Table 5.2). However, the claimed angular accuracies are likely for lengthy integration times (several seconds) and very benign environments.

Table 6.13: DMC Attitude Angle Differences – Test 1
(Prototype System Testing)

Exposure Number	Angle Differences (°)		
	<i>Roll</i>	<i>Pitch</i>	<i>Azimuth</i>
1	-1.201	-1.147	-1.282
2	-1.949	-0.902	-1.321
3	-1.937	-1.930	-0.112
4	-1.800	-0.892	-2.013
5	-1.713	-1.085	-0.235
Average	<i>-1.720</i>	<i>-1.191</i>	<i>-0.992</i>
Std. dev.	<i>0.306</i>	<i>0.428</i>	<i>0.803</i>
RMSE	<i>1.742</i>	<i>1.251</i>	<i>1.225</i>

6.3.3 Mapping Accuracy

For all the tests of the prototype system it was observed that including the DMC angles as weighted parameter observations in the adjustment degraded the accuracy of the object-space co-ordinates. Consequently, none of the tests used the DMC angles as observations in the adjustment. Of course, this raises the question as to whether the DMC is required in the backpack MMS at all. If the sole purpose of

Table 6.14: DMC Attitude Angle Differences – Test 2
(Prototype System Testing)

Exposure Number	Angle Differences (°)		
	<i>Roll</i>	<i>Pitch</i>	<i>Azimuth</i>
1	0.454	-0.807	8.634
2	1.336	-1.444	9.054
3	1.385	-1.014	10.032
4	0.332	-0.697	8.124
5	0.648	-1.619	9.018
6	2.416	-1.143	10.944
7	0.580	-1.050	9.674
Average	<i>1.022</i>	<i>-1.111</i>	<i>9.354</i>
Std. dev.	<i>0.688</i>	<i>0.304</i>	<i>0.872</i>
RMSE	<i>1.207</i>	<i>1.146</i>	<i>9.390</i>

Table 6.15: DMC Attitude Angle Differences – Test 3
(Prototype System Testing)

Exposure Number	Angle Differences (°)		
	<i>Roll</i>	<i>Pitch</i>	<i>Azimuth</i>
1	0.238	-1.412	7.650
2	2.153	-0.793	9.139
3	1.097	-0.855	8.862
4	1.454	-0.812	10.295
5	0.824	-0.859	7.700
6	0.171	-1.074	7.439
7	0.744	-0.836	9.236
8	0.898	-1.444	8.932
9	1.832	-0.709	10.015
10	0.214	-2.862	12.113
11	0.875	-0.631	9.469
12	1.320	-1.930	8.971
Average	<i>0.985</i>	<i>-1.185</i>	<i>9.152</i>
Std. dev.	<i>0.628</i>	<i>0.651</i>	<i>1.293</i>
RMSE	<i>1.154</i>	<i>1.339</i>	<i>9.235</i>

Table 6.16: Results (Approximate Camera to Object Point Distance = 40 m)

	Statistics of Co-ordinate Differences (m)					
	Horizontal			Vertical		
	<i>Mean</i>	<i>Std. Dev.</i>	<i>RMSE</i>	<i>Mean</i>	<i>Std. Dev.</i>	<i>RMSE</i>
<i>Test 1 – 5 images, 14 points</i>	0.14	0.11	0.17	-0.22	0.07	0.23
<i>Test 2 – 7 images, 12 points</i>	0.07	0.05	0.09	-0.03	0.02	0.04
<i>Test 3 – 12 images, 13 points</i>	0.13	0.04	0.13	0.09	0.02	0.09

the DMC was to provide orientation observations then the answer would be that it is not required. However, the DMC also provides the initial estimates for the bundle adjustment. Practically speaking, a user of the backpack MMS could not be expected to know their attitude at all times, and consequently the DMC – or another attitude sensing device – is still required to provide these estimates.

The best possible mapping accuracies for the prototype system are shown in Table 6.16. Generally, the desired accuracies are achieved, although the large values for the first test are borderline. For all tests, it can be observed that much of the error is a bias. Because of this, the relative error – particularly in height – is much better than the absolute error. This is not surprising, as the relative error depends on the internal strength of the photogrammetric network. Conversely, the absolute error depends on the how well the GPS positions define the datum, and it has already been shown that these positions have a bias in them.

As with the proof-of-concept testing, a likely source of error in the prototype system testing was inaccurate image measurements. Again, the resolution of the camera, combined with the distance to the points-of-interest, were the cause. In ad-

dition, to use the external flash signal of the DC260 – as was done in the prototype system – it is necessary to set the aperture of the camera at a fixed setting. Consequently, the camera no longer performs automatic exposure compensation, and as a result the images are not ideally exposed. Both over-exposure and under-exposure will “wash-out” detail in the images. The problem of correct exposure was further exacerbated by the difference in intensities between portions of the target field that were in shadow and those in direct sunlight. An example of the problems faced in identifying target in poorly exposed areas can be seen in Figure 6.12.



Figure 6.12: Example of Poor Image Exposure

During testing it was observed that if the collinearity equations were linearised using the small-angle approximation of Section 3.3, then the RMS error of the check

points increased by 1 or 2 centimetres. The reason is that the matrix constructed using the small-angles is not orthogonal. Consequently, when it is used to update the (initially orthogonal) rotation matrices in the adjustment it causes them to become non-orthogonal. The farther the initial approximates of the attitude angles are from their true values, the larger the small angle corrections must be, and the worse the non-orthogonalities in the rotation matrices become. In the case of the DMC, the estimated angles were not particularly close to their true values, and consequently the small angle approximation did not perform well. It was thought that the problem with the non-orthogonal rotation matrices could be overcome by “re-orthogonalising” them between iterations using a technique similar to one of those described in Mortensen (1995). Unfortunately, testing indicated that this approach offered little improvement. If the re-orthogonalisation took place on every iteration, then it essentially undid the small-angle corrections. If it was done less frequently then the RMS improvement was insignificant.

Chapter 7

Conclusions

In this thesis, research for the development of a backpack MMS was described. The development was undertaken because the benefits of current land-based mobile mapping systems are not being taken advantage of by a wide group of users. For the use of land-based MMS to become more wide-spread, they must be cheaper, smaller, and less complex than current systems, while still providing similar accuracies. The backpack MMS satisfies all of these criteria.

7.1 Conclusions

The problems encountered during testing of the backpack MMS make it difficult to draw extensive conclusions regarding the operation of the system. However, a number of key conclusions can be made. These are summarised below.

- **Navigation sensor accuracies:** In all tests the navigation sensors performed worse than expected. Position accuracies around 2 centimetres were expected

from the post-mission dual-frequency GPS data used in testing. Instead, the observed values were three times larger. Because the GPS positions are used to define the datum of the photogrammetric networks measured by the backpack MMS, any error in them will be directly reflected in the accuracy of the derived object space co-ordinates. The analysis of the DMC accelerometers showed that the claimed roll and pitch accuracies were almost certainly optimistic, and the navigation sensor tests confirmed this.

- **Absolute mapping accuracies:** In both the proof-of-concept testing and the prototype testing, absolute object space accuracies of less than 0.2 metres (RMS) in horizontal and 0.3 m (RMS) in height were achieved. These accuracies were the same as the desired accuracies stated in the research objectives and, consequently, it is fair to say that the research objective was successfully met. With the latter testing, these accuracies were achieved at an average camera-to-object distance of 40 metres.

In spite of the research goal being successfully achieved, the object space accuracies are somewhat disappointing. If the GPS positions and DMC angles would have been as accurate as anticipated then absolute object space accuracies of less than half of the research objectives could realistically have been expected.

- **Relative mapping accuracies:** Much of the mapping error is a bias. Consequently, the relative accuracy of the backpack MMS is much better than its absolute accuracy. This is not surprising, as the relative accuracies are largely dependant on the internal strength of the photogrammetric network.

7.2 Specific Contributions

All of the contributions of this research were minor advances in existing concepts, algorithms, or systems. However, it is worthwhile to review the most significant of these improvements. These are given below:

- **Proof of the concept of portable mobile mapping:** It is believed that the backpack MMS is the first example of a portable mobile mapping system. Using off-the-shelf components the backpack system successfully demonstrated that a portable mobile mapping system could provide absolute object space accuracies comparable to larger, more complex, and more expensive MMS.
- **Inclusion of GPS positions in a bundle adjustment:** Modified collinearity equations were derived to handle the inclusion of GPS positions in a bundle adjustment. Essentially, the new formulas permit the GPS positions to be used directly in the adjustment.
- **Inclusion of orientations in a bundle adjustment:** A detailed analysis was given regarding the inclusion of orientation observations in a bundle adjustment. A new technique was derived to rigorously include both the observations and their covariance in the adjustment.
- **Iterative IMU calibration algorithm:** A variation on the existing six-axis IMU calibration algorithm was developed. Through simulations the new algorithm was shown to be very effective at recovering accelerometer bias and scale errors, while still being simple to perform.

7.3 Future Investigations

In spite of the promising results achieved during testing of the prototype backpack MMS, it is felt that there is much room for improvement. Because the primary factor affecting object space accuracy is the accuracy of the navigations sensors, any effort to improve the system accuracy should begin with these sensors. Specific areas for improvement are described below.

- **Improving GPS accuracy:** In the prototype testing the GPS positions were entirely responsible for defining the datum of the photogrammetric networks measured from the backpack MMS's images. Even if the DMC's angles were included, the GPS positions would still have the most significant effect on the datum definition. Consequently, it would be worthwhile to focus on improving the accuracy of the GPS positions. One obvious way to improve the accuracy of the GPS positions is to average the measurements from more than one epoch. Alternatively, an antenna that was more effective at removing multipath than the one used in the prototype system could be tested.
- **Improving DMC accuracy:** Because of problems during testing, the DMC's angles were not used in the adjustment as weighted parameters. However, it is still felt that if a boresight calibration could be performed between the DMC and camera then the measured angles could contribute valuable information to the bundle adjustment. Another interesting investigation with the DMC would be to determine empirical temperature correction profiles for the accelerometer measurements. Using such profiles could significantly improve the roll and pitch accuracies of the DMC.

The DMC is one of a handful of devices that can provide the attitude of the backpack MMS. Other devices to supplant or supplement the DMC could be investigated. One obvious possibility is a dual-antenna GPS system. Such a system could likely only give a rough approximation of the azimuth, however it could be used to verify that the azimuth of the DMC is not being effected by magnetic disturbances.

The prototype system assembled as part of this research was only suitable for preliminary testing. An actual system would require several significant changes. Foremost among these is that RTK GPS would almost certainly have to be used so that the required position accuracies of the camera could be reliably maintained. This would require either a different GPS receiver or a different system configuration as currently the communications port in the NovAtel GPS receiver that would receive the real-time differential corrections is being used by the Leica DMC. The backpack MMS would also require a different camera. As outlined in the previous chapter, the Kodak cannot send an external flash signal and still perform automatic exposure compensation. Both are required for the practical application of the system. Finally, the operability of the backpack MMS would likely be increased by modifying the the physical arrangement of the various sensors. For example, mounting the whole system on a survey stick (prism pole) with the GPS antenna above the camera would likely make it much easier to maintain satellite lock. Use of a survey stick would also enable known points to be reliably occupied, as well as steady the camera during exposures.

Bibliography

- Abdel-Aziz, Y. I. and H. Karara, 1971. "Direct Linear Transformation from Comparator Coordinates into Object Space Coordinates in Close-Range Photogrammetry". In *Proceedings of the ASP/UI Symposium on Close-Range Photogrammetry*, pp. 1–18. Urbana, Illinois.
- Ackermann, F., 1992. "Kinematic GPS Control for Photogrammetry". *Photogrammetric Record*, 14(80):pp. 261–276.
- Alexander, J., 1996. "Gator Communicator: Design of a Hand Held Digital Mapper". In *Proceedings of the Third Congress on Computing in Civil Engineering*, pp. 1052–1057. Anaheim, CA.
- Barker-Benfield, S., 2000. "Extra Dimension: Professor-Patented Mapping Device Combines Old, New". *The Florida Times-Union*. URL http://www.jacksonville.com/tu-online/stories/071200/bus_3519070.html.
- Beliveau, A., G. Spencer, K. Thomas, and S. Robertson, 1999. "Evaluation of MEMs Capacitive Accelerometers". *IEEE Design and Test of Computers*, 16(4):pp. 48–55.
- Benning, W. and T. Aussems, 1998. "Mobile Mapping by a Car Driven Survey System (CDSS)". In H. Kahmen, E. Brückl, and T. Wunderlich (editors), *Proceedings of the Symposium on Geodesy for Geotechnical and Structural Engineering*. The International Association of Geodesy (IAG), Eisenstadt, Austria.
- Blaho, G. and C. Toth, 1995. "Field Experiences with a Fully Digital Mobile Stereo Image Acquisition System". In *Proceedings of the 1995 Mobile Mapping Symposium*, pp. 97–104. Columbus, OH.
- Bopp, H. and H. Krauss, 1978. "An Orientation and Calibration Method for Non-Topographic Applications". *Photogrammetric Engineering and Remote Sensing (PE&RS)*, 44(9):pp. 1191–1196.

- Brown, A., 1998. "High Accuracy Targeting Using a GPS-Aided Inertial Measurement Unit". In *Proceedings of the 54th Annual Meeting*. The Institute of Navigation (ION), Denver, CO.
- Brown, D. C., 1966. "Decentering Distortion of Lenses". *Photogrammetric Engineering*, 32(3):pp. 444–462.
- , 1971. "Close-Range Camera Calibration". *Photogrammetric Engineering*, 37(8):pp. 855–866.
- Burner, A., 1995. "Zoom Lens Calibration for Wind Tunnel Measurements". In *Proceedings of SPIE Vol. 2598 – Videometrics IV*. The International Society for Optical Engineering (SPIE), Philadelphia, PA.
- Caruso, M. J., 2000. "Applications of Magnetic Sensors for Low Cost Compass Systems". In *Positioning, Location, and Navigation Symposium (PLANS) 2000*, pp. 177–184. Institute of Electrical and Electronics Engineers (IEEE), San Diego, CA.
- Chaplin, B. A., 1999. *Motion Estimation From Image Sequences*. Master's Thesis, University of Calgary, Calgary, Canada.
- Clarke, T., X. Wang, and J. Fryer, 1998. "The Principal Point and CCD Cameras". *Photogrammetric Record*, 16(92):pp. 293–312.
- Coetsee, J., A. Brown, and J. Bossler, 1994. "GIS Data Collection Using The Gpsvan Supported By A GPS/Inertial Mapping System". In *Proceedings of GPS-94*. The Institute of Navigation (ION), Salt Lake City, UT.
- Cooper, M. and S. Robson, 1996. "Theory of Close Range Photogrammetry". In K. Atkinson (editor), *Close Range Photogrammetry and Machine Vision*, pp. 9–50. J.W. Arrowsmith, Bristol.
- Cosandier, D. and M. Chapman, 1992. "High Precision Target Location for Industrial Metrology". In *Proceedings of SPIE Vol. 3174 – Videometrics*, pp. 111–122. The International Society for Optical Engineering (SPIE), Boston, MA.
- Ebadi, H. and M. A. Chapman, 1998. "GPS-Controlled Strip Triangulation Using Geometric Constraints of Man-Made Structures". *Photogrammetric Engineering and Remote Sensing (PE&RS)*, 64(4):pp. 329–333.
- El-Hakim, S., 2001. "Homepage of ISPRS Working Group V/2 – Scene Modelling and Virtual Reality". URL <http://www.vit.iit.nrc.ca/elhakim/WGV2.html>. Holland1 Data Set.

- El-Hakim, S., P. Boulanger, F. Blais, and J. Beraldin, 1997. "A System for Indoor 3-D Mapping and Virtual Environments". In *Proceedings of SPIE Vol. 3174 – Videometrics V*, pp. 21–35. The International Society for Optical Engineering (SPIE), San Diego, CA.
- El-Sheimy, N., 1996. *The Development of VISAT – A Mobile Survey System for GIS Applications*. Ph.D. Thesis, University of Calgary, Calgary, Canada. URL <http://www.geomatics.ucalgary.ca/research/publications/index.php>.
- , 1999. "Mobile Multi-Sensor Systems: The New Trend in Mapping and GIS Applications". In K.-P. Schwarz (editor), *Geodesy Beyond 2000: The Challenges of the First Decade*, International Association of Geodesy Symposia Volume 120, pp. 319–324. Springer-Verlag, Berlin.
- El-Sheimy, N. and K.-P. Schwarz, 1996. "A Mobile Multi-Sensor System for GIS Applications in Urban Centers". *International Archives of Photogrammetry and Remote Sensing. Vol. XXXI. Part. B*, pp. 95–100. Proceedings of the XVIII ISPRS Congress. Vienna, Austria.
- Ellum, C., 2000. "Testing and Calibration of the Crossbow DMU-FOG Inertial Measurement Unit". Major Report for ENGO 623 GPS/INS Integration. Department of Geomatics Engineering, University of Calgary. Calgary, AB.
- Ellum, C. and N. El-Sheimy, 2002. "Land-Based Integrated Systems for Mapping and GIS Applications". *Survey Review*, 36(283).
- Faig, W. and T. Shih, 1988. "Functional Review of Additional Parameters". In *Proceedings of ASPRS 1988 Annual Convention*, pp. 158–168. American Society of Photogrammetry and Remote Sensing (ASPRS), St. Louis, MI.
- Fraser, C. S., 1983. "Photogrammetric Monitoring of Turtle Mountain: A Feasibility Study". *Photogrammetric Engineering and Remote Sensing (PE&RS)*, 49(11):pp. 1551–1559.
- , 1997. "Digital Camera Self-Calibration". *Photogrammetry and Remote Sensing*, 52:pp. 149–159.
- Fraser, C. S. and K. Edmundson, 2000. "Design and Implementation of a Computational Processing System for Off-Line Digital Close-Range Photogrammetry". *Photogrammetry and Remote Sensing*, 55(94-104).
- Fraser, C. S. and M. R. Shortis, 1992. "Variation of Distortion Within the Photogrammetric Field". *Photogrammetric Engineering and Remote Sensing (PE&RS)*, 58(6):pp. 851–855.

- Fraser, C. S., M. R. Shortis, and G. Ganci, 1995. "Multi-Sensor System Self-Calibration". In S. F. El-Hakim (editor), *Proceedings of SPIE Vol. 2598 – Videometrics IV*, pp. 2–18. The International Society for Optical Engineering (SPIE), Philadelphia, PA.
- Fryer, J. and D. Brown, 1986. "Lens Distortion for Close-Range Photogrammetry". *Photogrammetric Engineering and Remote Sensing (PE&RS)*, 52(1):pp. 51–58.
- Fryer, J. G., 1992. "Recent Developments in Camera Calibration for Close-Range Applications". *ISPRS International Archives of Photogrammetry and Remote Sensing*, IXXX(5):pp. 594–599. Proceedings of the ISPRS Congress, Commission V. Washington D.C.
- , 1996. "Camera Calibration". In K. Atkinson (editor), *Close Range Photogrammetry and Machine Vision*, pp. 156–179. J.W. Arrowsmith, Bristol.
- Geological Survey of Canada (GSC), 2000. "Magnetic Declination". URL http://www.geolab.emr.ca/geomag/e_magdec.htm. Accessed 31 Oct. 2000.
- Goad, C. C., 1991. "The Ohio State University Mapping System: The Positioning Component". In *Proceedings of the 47th Annual Meeting*, pp. 121–124. The Institute of Navigation (ION), Williamsburg, VA.
- Graefe, G., W. Caspary, H. Heister, J. Klemm, and M. Sever, 2001. "The Road Data Acquisition System MoSES – Determination and Accuracy of Trajectory Data Gained with the Applanix POS/LV". In N. El-Sheimy (editor), *Proceedings of The 3rd International Symposium on Mobile Mapping Technology (MMS 2001)*. Cario, Egypt. On CD-ROM.
- Granshaw, S., 1980. "Bundle Adjustment Methods in Engineering Photogrammetry". *Photogrammetric Record*, 10(56):pp. 181–207.
- Grejner-Brzezinska, D., C. Toth, and E. Oshel, 1999. "Direct Platform Orientation in Aerial and Land-Based Mobile Mapping Practice". *International Archives of Photogrammetry and Remote Sensing*, XXXII. Proceedings of the International Workshop on Mobile Mapping Technology. Bangkok, Thailand.
- Grejner-Brzezinska, D. A., 2001. "Mobile Mapping Technology: Ten Years Later (Part One)". *Surveying and Land Information Systems (SaLIS)*, 61(2):p. 75.
- Hatze, H., 1988. "High-Precision Three-Dimensional Photogrammetric Calibration and Object Space Reconstruction Using a Modified DLT Approach". *Journal of Biomechanics*, 21(7):pp. 533–538.

- He, G., K. Novak, and W. Feng, 1992. "Stereo Camera System Calibration with Relative Orientation Constraints". In S. F. El-Hakim (editor), *Proceedings of SPIE Vol. 1820 - Videometrics*, pp. 2–8. The International Society for Optical Engineering (SPIE), Boston, MA.
- He, G., G. Orvets, and R. Hammersley, 1996. "Capturing Urban Infrastructure Data Using Mobile Mapping System". In *Proceeding of the 52nd Annual Meeting*, pp. 667–674. The Institute of Navigation (ION), Cambridge, MA.
- Hock, C., W. Caspary, H. Heister, J. Klemm, and H. Sternberg, 1995. "Architecture and Design of the Kinematic Survey System KiSS". In *Proceedings of the 3rd International Workshop on High Precision Navigation*, pp. 569–576. Stuttgart, Germany.
- Intel, 2001. "Intel's JPEG Library". URL <http://support.intel.com/support/performance/tools/libraries/ijl>. Accessed 4 Nov. 2001.
- Kodak, 2001. "Kodak Frequently Asked Questions (FAQ): Kodak DC260 Zoom Digital Camera". URL <http://www.kodak.com/global/en/service/faqs/faq1539.shtml>. Accessed 14 Nov. 2001.
- Kuang, S., 1996. *Geodetic Network Analysis and Optimal Design: Concepts and Applications*. Ann Arbor Press, Inc, Chelsea, MI.
- Lachapelle, G., R. Klukas, D. Roberts, W. Qiu, and C. McMillan, 1994. "One-Meter Level Kinematic Point Positioning Using Precise Orbit and Timing Information". In *GPS-94*, pp. 1435–1443. The Institute of Navigation (ION), Salt Lake City, UT.
- Lambda Tech, 2001. "Welcome To Lambda Tech International". URL <http://www.lambdatech.com>. Accessed 10 Feb. 2001.
- Leica, 1999. *DMC-SX Performance Specifications*. Leica Product Literature.
- Li, D., S.-D. Zhong, S.-X. He, and H. Zheng, 1999. "A Mobile Mapping System Based on GPS, GIS and Multi-Sensor". In *Proceedings International Workshop on Mobile Mapping Technology*, pp. 1–3–1 – 1–3–5. Bangkok, Thailand.
- Li, Q., B. Li, J. Chen, Q. Hu, and Y. Li, 2001. "3D Mobile Mapping System for Road Modeling". In N. El-Sheimy (editor), *The 3rd International Symposium on Mobile Mapping Technology (MMS 2001)*. Cairo, Egypt. On CD-ROM.

- Li, R., 1997. "Mobile Mapping: An Emerging Technology for Spatial Data Acquisition". *Photogrammetric Engineering and Remote Sensing (PE&RS)*, 63(9):pp. 1085–1092.
- LibJPEG, 2001. "Homepage of the Independent JPEG Group". URL <http://www.ijg.org>. Accessed 4 Nov. 2001.
- LibPNG, 2001. "LibPNG Home Page". URL <http://www.libpng.org>. Accessed 4 Nov. 2001.
- LibTIFF, 2001. "LibTIFF Homepage". URL <http://www.libtiff.org>. Accessed 4 Nov. 2001.
- Lichti, D., M. Chapman, and D. Cosandier, 1995. "INDMET: An Industrial Oriented Softcopy Photogrammetric System". *Geomatica*, 49(4):pp. 471–477.
- Lichti, D. D., 1996. *Constrained Finite Element Method Self-Calibration*. Master's Thesis, University of Calgary, Calgary, Canada.
- Lichti, D. D. and M. A. Chapman, 1997. "Constrained FEM Self-Calibration". *Photogrammetric Engineering and Remote Sensing (PE&RS)*, 63(9):pp. 1111–1119.
- Livingston, R. G., 1980. "Aerial Cameras". In C. C. Slama (editor), *Manual of Photogrammetry*, chapter 1, pp. 187–277. American Society of Photogrammetry, Falls Church, USA, 4th edition.
- Magill, A., 1955. "Variation in Distortion with Magnification". *Journal of Research of the National Bureau of Standards*, 54(3):pp. 135–142. Research Paper 2574.
- Mikhail, E. M., 1976. *Observations and Least Squares*. IEP-A Dun-Donnelley, New York.
- Mikhail, E. M., J. S. Bethel, and J. C. McGlone, 2001. *Introduction to Modern Photogrammetry*. John Wiley and Sons, Inc., New York.
- Moffit, F. H., 1967. *Photogrammetry*. International Textbooks in Civil Engineering. International Textbook Company, 2nd edition.
- Moffit, F. H. and E. M. Mikhail, 1980. *Photogrammetry*. Series in Civil Engineering. Harper & Row, New York, 3rd edition.
- Morin, K., C. Ellum, and N. El-Sheimy, 2001. "The Calibration of Zoom Lenses on Consumer Digital Cameras, and Their Applications in Precise Mapping Applications". In N. El-Sheimy (editor), *The 3rd International Symposium on Mobile Mapping Technology (MMS 2001)*. Cario, Egypt. On CD-ROM.

- Mortensen, Z., 1995. "Matrix Transform Tutorial". URL <http://www.gamedev.net/reference/articles/article417.asp>. Accessed 17 Jan. 2002.
- Mostafa, M. and K.-P. Schwarz, 1999. "An Autonomous Multi-Sensor System for Airborne Digital Image Capture and Georeferencing". In *ASPRS Annual Convention*, pp. 976–987. Portland, Oregon.
- Mostafa, M. M. R., 1999. *Georeferencing Airborne Images From a Multiple Digital Camera System by GPS/INS*. Ph.D. Thesis, University of Calgary, Calgary, Canada.
- Murai, S., R. Matcuoka, and A. Okuda, 1984. "A Study on Analytical Calibration of Non-metric Camera and Accuracy of Three-dimensional Measurement". *ISPRS International Archives of Photogrammetry and Remote Sensing*, 25(A5):pp. 570–579. Proceedings of the ISPRS Congress.
- Novak, K., 1990. "Integration of a GPS Receiver and a Stereo-Vision System in a Vehicle". In *Proceedings of SPIE Vol. 1395 – Close-Range Photogrammetry Meets Machine Vision*, pp. 16–23. The International Society for Optical Engineering (SPIE), Zurich, Switzerland.
- , 1991. "The Ohio State University Mapping System: The Stereo Vision System Component". In *Proceedings of the 47th Annual Meeting*, pp. 121–124. The Institute of Navigation (ION), Williamsburg, VA.
- , 1993. "Data Collection For Multi-Media GIS Using Mobile Mapping Systems". *Geomatics Info Magazine (GIM)*, 7(3):pp. 30–32.
- , 1995. "Mobile Mapping Technology for GIS Data Collection". *Photogrammetric Engineering and Remote Sensing (PE&RS)*, 61(5):pp. 493–501.
- NovaTel, 1997. *MiLLennium GPSCard™ Command Descriptions Manual*. URL <http://www.novatel.ca/Products/productmanuals.html>. NovaTel Product Literature.
- Patias, P. and A. Streilein, 1996. "Contribution of Videogrammetry to the Architectural Restitution. Results of the CIPA "O. Wagner Pavillion" Test". *ISPRS International Archives of Photogrammetry and Remote Sensing*, 31(B5):pp. 457–462. Proceedings of the ISPRS Congress.
- Press, W. H., B. P. Flannery, S. A. Teukolsky, and W. T. Vetterling, 1992. *Numerical Recipes: The Art of Scientific Computing*. Cambridge University Press, Cambridge, United Kingdom, 2nd edition.

- Reed, M., C. Landry, and K. Werther, 1996. "The Application of Air and Ground Based Laser Mapping Systems to Transmission Line Corridor Surveys". In *Proceedings of Position, Location and Navigation Symposium (PLANS 1996)*, pp. 444–451. Institute of Electrical and Electronics Engineers (IEEE), Atlanta, GA.
- Schwarz, K.-P., 1997. *ENGO 421 Lecture Notes – Fundamentals of Geodesy*. Department of Geomatics Engineering, The University of Calgary, Calgary, Canada. Lecture Notes.
- Schwarz, K.-P. and N. El-Sheimy, 1999. "Future Positioning and Navigation Technologies". Technical report, Department of Geomatics Engineering, The University of Calgary. Report submitted to the US Topographic Engineering Centre. Contract No. DAAH04-96-C-0086.
- Schwarz, K.-P., H. Martell, N. El-Sheimy, R. Li, M. Chapman, and D. Cosandier, 1993. "VISAT – A Mobile Highway Survey System of High Accuracy". In *Proceedings of the Vehicle Navigation and Information Systems Conference*, pp. 467–481. Institute of Electrical and Electronics Engineers (IEEE), Ottawa, Canada.
- Schwarz, K.-P. and M. Wei, 2000. *ENGO 623 Lecture Notes – INS/GPS Integration for Geodetic Applications*. Department of Geomatics Engineering, The University of Calgary, Calgary, Canada. Lecture Notes.
- Seuss, D., 1960. *One Fish Two Fish Red Fish Blue Fish*. Random House of Canada, Ltd., Toronto.
- Shortis, M. and H. Beyer, 1996. "Sensor Technology for Digital Photogrammetry and Machine Vision". In K. Atkinson (editor), *Close Range Photogrammetry and Machine Vision*, pp. 106–155. J.W. Arrowsmith, Bristol.
- Shortis, M. R., C. L. Ogleby, S. Robson, E. Karalis, and H. A. Beyer, 2001. "Calibration Modelling and Stability Testing for the Kodak DC200 Series Digital Still Camera". In *Proceedings of SPIE Vol. 4309 – Videometrics and Optical Methods for 3D Shape Measurement*, pp. 148–153. The International Society for Optical Engineering (SPIE), Zurich, Switzerland.
- Shortis, M. R., S. Robson, and H. A. Beyer, 1998. "Extended Lens Model Calibration of Digital Still Cameras". *ISPRS International Archives of Photogrammetry and Remote Sensing*, 31(5):pp. 159–164. Proceeding of the Commission V Meeting. Okodate, Japan. Jun 2-5.
- Škaloud, J. and K.-P. Schwarz, 2000. "Accurate Orientation for Airborne Mapping Systems". *Photogrammetric Engineering and Remote Sensing (PE&RS)*, 66(4):pp. 393–402.

- Stephen, J., 2000. *Development Of A Multi-Sensor GNSS Based Vehicle Navigation System*. Master's Thesis, University of Calgary, Calgary, Canada. URL <http://www.geomatics.ucalgary.ca/research/publications/index.php>.
- Sternberg, H., W. Caspary, H. Heister, and J. Klemm, 2001. "Mobile Data Capturing on Roads and Railways Utilizing the Kinematic Survey System KiSS". In N. El-Sheimy (editor), *Proceedings of The 3rd International Symposium on Mobile Mapping Technology (MMS 2001)*. Cario, Egypt. On CD-ROM.
- Tabatabai, A. J. and O. R. Mitchell, 1984. "Edge Location to Subpixel Values in Digital Imagery". *IEEE Transactions on Pattern Analysis and Machine Intelligence*, PAMI-6(2):pp. 188–202.
- Tao, C. V., 1998. "Towards Sensor Integrated Technology to Fast Spatial Data Acquisition". In Q. Zhou, Z. Li, H. Lin, and W. Shi (editors), *Proceedings of Spatial Information Technology Towards 2000 and Beyond*, pp. 33–42. The Association of Chinese Professionals in GIS - Abroad, Beijing.
- Thompson, M. M., 1980. "Foundations of Photogrammetry". In C. C. Slama (editor), *Manual of Photogrammetry*, chapter 1, pp. 1–36. American Society of Photogrammetry, Falls Church, USA, 4th edition.
- Titterton, D. H. and J. Weston, 1997. *Strapdown Inertial Navigation Technology*, volume 5 of *IEE Radar, Sonar, Navigation and Avionics Series*. Peter Peregrinus Ltd., Stevenage, United Kingdom.
- Transmap, 2001. "Welcome To Transmap Corp". URL <http://www.transmap.com>. Accessed 10 Feb. 2001.
- Wolf, P. R., 1983. *Elements of Photogrammetry*. McGraw-Hill, Inc., New York, 2nd edition.

Appendix A

Derivations

A.1 Rotation Matrices and Derivatives

The elementary rotation matrices and their derivatives are as follows:

$$\begin{aligned}\mathbf{R}_x(\alpha) &= \begin{pmatrix} 1 & 0 & 0 \\ 0 & \cos(\alpha) & \sin(\alpha) \\ 0 & -\sin(\alpha) & \cos(\alpha) \end{pmatrix} \\ \frac{\partial \mathbf{R}_x(\alpha)}{\partial \alpha} &= \begin{pmatrix} 0 & 0 & 0 \\ 0 & -\sin(\alpha) & \cos(\alpha) \\ 0 & -\cos(\alpha) & -\sin(\alpha) \end{pmatrix} \\ &= \mathbf{R}_x(\alpha) \begin{pmatrix} 0 & 0 & 0 \\ 0 & 0 & 1 \\ 0 & -1 & 0 \end{pmatrix} = \begin{pmatrix} 0 & 0 & 0 \\ 0 & 0 & 1 \\ 0 & -1 & 0 \end{pmatrix} \mathbf{R}_x(\alpha) \quad (\text{A.1})\end{aligned}$$

$$\begin{aligned}
\mathbf{R}_y(\alpha) &= \begin{pmatrix} \cos(\alpha) & 0 & -\sin(\alpha) \\ 0 & 1 & 0 \\ \sin(\alpha) & 0 & \cos(\alpha) \end{pmatrix} \\
\frac{\partial \mathbf{R}_y(\alpha)}{\partial \alpha} &= \begin{pmatrix} -\sin(\alpha) & 0 & -\cos(\alpha) \\ 0 & 0 & 0 \\ \cos(\alpha) & 0 & -\sin(\alpha) \end{pmatrix} \\
&= \mathbf{R}_y(\alpha) \begin{pmatrix} 0 & 0 & -1 \\ 0 & 0 & 0 \\ 1 & 0 & 0 \end{pmatrix} = \begin{pmatrix} 0 & 0 & -1 \\ 0 & 0 & 0 \\ 1 & 0 & 0 \end{pmatrix} \mathbf{R}_y(\alpha) \quad (\text{A.2})
\end{aligned}$$

$$\begin{aligned}
\mathbf{R}_z(\alpha) &= \begin{pmatrix} \cos(\alpha) & \sin(\alpha) & 0 \\ -\sin(\alpha) & \cos(\alpha) & 0 \\ 0 & 0 & 1 \end{pmatrix} \\
\frac{\partial \mathbf{R}_z(\alpha)}{\partial \alpha} &= \begin{pmatrix} -\sin(\alpha) & \cos(\alpha) & 0 \\ -\cos(\alpha) & -\sin(\alpha) & 0 \\ 0 & 0 & 0 \end{pmatrix} \\
&= \mathbf{R}_z(\alpha) \begin{pmatrix} 0 & 1 & 0 \\ -1 & 0 & 0 \\ 0 & 0 & 0 \end{pmatrix} = \begin{pmatrix} 0 & 1 & 0 \\ -1 & 0 & 0 \\ 0 & 0 & 0 \end{pmatrix} \mathbf{R}_z(\alpha) \quad (\text{A.3})
\end{aligned}$$

A.2 Derivatives of Roll, Pitch, and Yaw Rotation Matrix

The partial derivatives of the rotation matrix \mathbf{R}_{ll}^b with respect to the roll, pitch, and yaw angles can be calculated using Equations (A.1), (A.2), and (A.3). The rotation matrix is given by

$$\mathbf{R}_{ll}^b = \mathbf{R}_y(\varphi)\mathbf{R}_x(\theta)\mathbf{R}_z(\psi). \quad (\text{A.4})$$

and the partial derivatives are given as

$$\begin{aligned} \frac{\partial \mathbf{R}_{ll}^b}{\partial \varphi} &= \frac{\partial \mathbf{R}_y(\varphi)}{\partial \varphi} \mathbf{R}_x(\theta) \mathbf{R}_z(\psi) \\ &= \begin{pmatrix} 0 & 0 & -1 \\ 0 & 0 & 0 \\ 1 & 0 & 0 \end{pmatrix} \mathbf{R}_{ll}^b \\ &= \begin{pmatrix} -r_{31} & -r_{32} & -r_{33} \\ 0 & 0 & 0 \\ r_{11} & r_{12} & r_{13} \end{pmatrix} \end{aligned} \quad (\text{A.5})$$

$$\begin{aligned} \frac{\partial \mathbf{R}_{ll}^b}{\partial \theta} &= \mathbf{R}_y(\varphi) \frac{\partial \mathbf{R}_x(\theta)}{\partial \theta} \mathbf{R}_z(\psi) \\ &= \mathbf{R}_y(\varphi) \mathbf{R}_x(\theta) \begin{pmatrix} 0 & 0 & 0 \\ 0 & 0 & 1 \\ 0 & -1 & 0 \end{pmatrix} \mathbf{R}_z(\psi) \end{aligned}$$

$$\begin{aligned}
&= \mathbf{R}_y(\varphi)\mathbf{R}_x(\theta) \begin{pmatrix} 0 & 0 & 0 \\ 0 & 0 & 1 \\ \sin(\psi) & -\cos(\psi) & 0 \end{pmatrix} \\
&= \mathbf{R}_y(\varphi)\mathbf{R}_x(\theta) \\
&\quad \begin{pmatrix} \cos(\psi) & \sin(\psi) & 0 \\ -\sin(\psi) & \cos(\psi) & 0 \\ 0 & 0 & 1 \end{pmatrix} \begin{pmatrix} 0 & 0 & -\sin(\psi) \\ 0 & 0 & \cos(\psi) \\ \sin(\psi) & -\cos(\psi) & 0 \end{pmatrix} \\
&= \mathbf{R}_{ll}^b \begin{pmatrix} 0 & 0 & -\sin(\psi) \\ 0 & 0 & \cos(\psi) \\ \sin(\psi) & -\cos(\psi) & 0 \end{pmatrix} \tag{A.6}
\end{aligned}$$

$$= \begin{pmatrix} r_{13} \sin(\psi) & -r_{13} \cos(\psi) & \sin(\varphi) \sin(\theta) \\ r_{23} \sin(\psi) & -r_{23} \cos(\psi) & \cos(\theta) \\ r_{33} \sin(\psi) & -r_{33} \cos(\psi) & -\cos(\varphi) \sin(\theta) \end{pmatrix} \tag{A.7}$$

$$\begin{aligned}
\frac{\partial \mathbf{R}_{ll}^b}{\partial \psi} &= \mathbf{R}_y(\varphi)\mathbf{R}_x(\theta) \frac{\partial \mathbf{R}_z(\psi)}{\partial \psi} \\
&= \mathbf{R}_{ll}^b \begin{pmatrix} 0 & 1 & 0 \\ -1 & 0 & 0 \\ 0 & 0 & 0 \end{pmatrix} \tag{A.8}
\end{aligned}$$

$$= \begin{pmatrix} -r_{12} & r_{11} & 0 \\ -r_{22} & r_{21} & 0 \\ -r_{32} & r_{31} & 0 \end{pmatrix}. \tag{A.9}$$

A.3 Error Propagation for Angle Conversion

The roll, pitch, and yaw angles (denoted by φ , θ , and ψ respectively), are related to the ω , ϕ , and κ angles by

$$\omega = \arctan\left(\frac{-r_{32}}{r_{33}}\right), \quad (\text{A.10a})$$

$$\phi = \arcsin(r_{31}), \quad (\text{A.10b})$$

and

$$\kappa = \arctan\left(\frac{-r_{21}}{r_{11}}\right). \quad (\text{A.10c})$$

where r_{ij} are the elements of the rotation matrix \mathbf{R}_{ll}^c , which is defined as

$$\mathbf{R}_{ll}^c = \mathbf{R}_b^c \mathbf{R}_{ll}^b = \mathbf{R}_b^c \mathbf{R}_y(\varphi) \mathbf{R}_x(\theta) \mathbf{R}_z(\psi). \quad (\text{A.11})$$

If, as in Section 3.3, the rotation matrix \mathbf{R}_b^c between the camera and body frames is approximated by

$$\mathbf{R}_b^c = \begin{pmatrix} -1 & 0 & 0 \\ 0 & 0 & 1 \\ 0 & 1 & 0 \end{pmatrix}, \quad (\text{A.12})$$

then \mathbf{R}_{ll}^c is equal to

$$\mathbf{R}_{ll}^c = \begin{pmatrix} -\cos(\varphi)\cos(\psi)+\sin(\varphi)\sin(\theta)\sin(\psi) & -\cos(\varphi)\sin(\psi)-\sin(\varphi)\sin(\theta)\cos(\psi) & \sin(\varphi)\cos(\theta) \\ \sin(\varphi)\cos(\psi)+\cos(\varphi)\sin(\theta)\sin(\psi) & \sin(\varphi)\sin(\psi)-\cos(\varphi)\sin(\theta)\cos(\psi) & \cos(\varphi)\cos(\theta) \\ -\cos(\theta)\sin(\psi) & \cos(\theta)\cos(\psi) & \sin(\theta) \end{pmatrix}. \quad (\text{A.13})$$

If the individual elements of the \mathbf{R}_{ll}^b matrix are indicated by r'_{ij} , then Equation (A.13) is equivalent to,

$$\mathbf{R}_{ll}^c = \begin{pmatrix} -r'_{11} & -r'_{12} & -r'_{13} \\ r'_{31} & r'_{32} & r'_{33} \\ r'_{21} & r'_{22} & r'_{23} \end{pmatrix}. \quad (\text{A.14})$$

Consequently, Equations (A.10) can be expressed as

$$\omega = \arctan\left(\frac{-r'_{22}}{r'_{23}}\right), \quad (\text{A.15a})$$

$$\phi = \arcsin(r'_{21}), \quad (\text{A.15b})$$

and

$$\kappa = \arctan\left(\frac{-r'_{31}}{-r'_{11}}\right). \quad (\text{A.15c})$$

Using error propagation, the covariance of the ω , ϕ , and κ angles can be calculated

from the covariance of the φ , θ , and ψ angles by

$$\mathbf{C}_{\omega\phi\kappa} = \mathbf{J}\mathbf{C}_{\varphi\theta\psi}\mathbf{J}^T \quad (\text{A.16})$$

where $\mathbf{C}_{\omega\phi\kappa}$ is the covariance matrix of the ω , ϕ , and κ angles, $\mathbf{C}_{\varphi\theta\psi}$ is the covariance matrix of the φ , θ , and ψ angles, and \mathbf{J} is the Jacobian of Equations (A.10), or

$$\mathbf{J} = \begin{pmatrix} \frac{\partial\omega}{\partial\varphi} & \frac{\partial\omega}{\partial\theta} & \frac{\partial\omega}{\partial\psi} \\ \frac{\partial\phi}{\partial\varphi} & \frac{\partial\phi}{\partial\theta} & \frac{\partial\phi}{\partial\psi} \\ \frac{\partial\kappa}{\partial\varphi} & \frac{\partial\kappa}{\partial\theta} & \frac{\partial\kappa}{\partial\psi} \end{pmatrix} \quad (\text{A.17})$$

To evaluate the Jacobian, the following relations are required:

$$\frac{d \arctan(u)}{dx} = \frac{1}{1+u^2} \frac{du}{dx} \quad (\text{A.18})$$

$$\frac{d \arcsin(u)}{dx} = \frac{1}{\sqrt{1-u^2}} \frac{du}{dx} \quad (\text{A.19})$$

Using Equation (A.18), the chain rule, and the quotient rule, the derivatives of Equation (A.15a) with respect to the φ , θ , and ψ angles can be calculated as,

$$\begin{aligned} \frac{\partial\omega}{\partial\varphi} &= \frac{\partial}{\partial\varphi} \left[\arctan \left(\frac{-r'_{22}}{r'_{23}} \right) \right] \\ &= \frac{1}{1 + \left(\frac{-r'_{22}}{r'_{23}} \right)^2} \frac{\partial}{\partial\varphi} \left(\frac{-r'_{22}}{r'_{23}} \right) \\ &= \frac{r'_{23}{}^2}{r'_{23}{}^2 + r'_{22}{}^2} \frac{-r'_{23} \frac{\partial r'_{22}}{\partial\varphi} + r'_{22} \frac{\partial r'_{23}}{\partial\varphi}}{r'_{23}{}^2} \\ &= 0, \end{aligned} \quad (\text{A.20})$$

$$\begin{aligned}
\frac{\partial \omega}{\partial \theta} &= \frac{-r'_{23} \frac{\partial r'_{22}}{\partial \theta} + r'_{22} \frac{\partial r'_{23}}{\partial \theta}}{r'_{23}{}^2 + r'_{22}{}^2} \\
&= \frac{r'_{23}{}^2 \cos \psi + r'_{22} \cos \theta}{r'_{23}{}^2 + r'_{22}{}^2} \\
&= \frac{\cos \psi}{r'_{23}{}^2 + r'_{22}{}^2}
\end{aligned} \tag{A.21}$$

and

$$\begin{aligned}
\frac{\partial \omega}{\partial \psi} &= \frac{-r'_{23} \frac{\partial r'_{22}}{\partial \psi} + r'_{22} \frac{\partial r'_{23}}{\partial \psi}}{r'_{23}{}^2 + r'_{22}{}^2} \\
&= \frac{-r'_{23} r'_{21}}{r'_{23}{}^2 + r'_{22}{}^2}.
\end{aligned} \tag{A.22}$$

Similarly, the derivatives of Equation (A.15b) with respect to φ , θ , and ψ are

$$\begin{aligned}
\frac{\partial \phi}{\partial \varphi} &= \frac{\partial \arcsin(r'_{21})}{\partial \varphi} \\
&= \frac{1}{\sqrt{1 - r'_{21}{}^2}} \frac{\partial r'_{21}}{\partial \varphi} \\
&= 0,
\end{aligned} \tag{A.23}$$

$$\begin{aligned}
\frac{\partial \phi}{\partial \theta} &= \frac{1}{\sqrt{1 - r'_{21}{}^2}} \frac{\partial r'_{21}}{\partial \theta} \\
&= \frac{r'_{23} \sin \psi}{\sqrt{1 - r'_{21}{}^2}},
\end{aligned} \tag{A.24}$$

and

$$\frac{\partial \phi}{\partial \psi} = \frac{1}{\sqrt{1 - r'_{21}{}^2}} \frac{\partial r'_{21}}{\partial \psi}$$

$$= \frac{-r'_{22}}{\sqrt{1 - r'_{21}{}^2}}. \quad (\text{A.25})$$

And finally, the derivatives of Equation (A.15c) are

$$\begin{aligned} \frac{\partial \omega}{\partial \varphi} &= \frac{r'_{11} \frac{\partial r'_{31}}{\partial \varphi} - r'_{31} \frac{\partial r'_{11}}{\partial \varphi}}{r'_{11}{}^2 + r'_{31}{}^2} \\ &= \frac{r'_{11}{}^2 + r'_{31}{}^2}{r'_{11}{}^2 + r'_{31}{}^2} \\ &= 1, \end{aligned} \quad (\text{A.26})$$

$$\begin{aligned} \frac{\partial \omega}{\partial \theta} &= \frac{r'_{11} \frac{\partial r'_{31}}{\partial \theta} - r'_{31} \frac{\partial r'_{11}}{\partial \theta}}{r'_{11}{}^2 + r'_{31}{}^2} \\ &= \frac{r'_{11} r'_{33} \sin \psi - r'_{31} r'_{13} \sin \psi}{r'_{11}{}^2 + r'_{31}{}^2}, \\ &= \frac{r'_{23}}{r'_{23}{}^2 + r'_{22}{}^2}, \end{aligned} \quad (\text{A.27})$$

and

$$\begin{aligned} \frac{\partial \omega}{\partial \psi} &= \frac{r'_{11} \frac{\partial r'_{31}}{\partial \psi} - r'_{31} \frac{\partial r'_{11}}{\partial \psi}}{r'_{11}{}^2 + r'_{31}{}^2} \\ &= \frac{-r'_{11} r'_{32} + r'_{31} r'_{12}}{r'_{11}{}^2 + r'_{31}{}^2} \\ &= \frac{r'_{22} \sin \psi}{r'_{23}{}^2 + r'_{22}{}^2}. \end{aligned} \quad (\text{A.28})$$

If \mathbf{R}_b^c is more complicated than a simple reflection matrix, then error propagation becomes exponentially more difficult (the r_{ij} terms in Equation (A.10) become very lengthy). However, if \mathbf{R}_b^c is close to being a reflection matrix, then error propagation performed on a simplified \mathbf{R}_b^c will likely be adequate for virtually all applications.

A.4 Linearised Collinearity Equations for Roll, Pitch, and Yaw Angles

First, the partial derivatives of the numerators and denominator of the collinearity equations are required. The numerators and denominators are given by Equation (2.10). Again, they are

$$\begin{pmatrix} x_{c/p} \\ y_{c/p} \\ z_{c/p} \end{pmatrix}^c = \mathbf{R}_b^c \mathbf{R}_{ll}^b \begin{pmatrix} X_P - X_c \\ Y_P - Y_c \\ Z_P - Z_c \end{pmatrix}^M. \quad (\text{A.29})$$

The partial derivatives are then given by,

$$\begin{aligned} \frac{\partial}{\partial \varphi} \begin{pmatrix} x_{c/p} \\ y_{c/p} \\ z_{c/p} \end{pmatrix}^c &= \mathbf{R}_b^c \frac{\partial \mathbf{R}_{ll}^b}{\partial \varphi} \begin{pmatrix} X_P - X_c \\ Y_P - Y_c \\ Z_P - Z_c \end{pmatrix}^M \\ &= \mathbf{R}_b^c \begin{pmatrix} 0 & 0 & -1 \\ 0 & 0 & 0 \\ 1 & 0 & 0 \end{pmatrix} \mathbf{R} \begin{pmatrix} X_P - X_c \\ Y_P - Y_c \\ Z_P - Z_c \end{pmatrix}^M \\ &= \mathbf{R}_b^c \mathbf{R} \begin{pmatrix} Y_P - Y_c \\ 0 \\ -(Z_P - Z_c) \end{pmatrix}^M \end{aligned} \quad (\text{A.30})$$

$$\begin{aligned}
\frac{\partial}{\partial \theta} \begin{pmatrix} x_{c/p} \\ y_{c/p} \\ z_{c/p} \end{pmatrix}^c &= \mathbf{R}_b^c \frac{\partial \mathbf{R}_{ll}^b}{\partial \theta} \begin{pmatrix} X_P - X_c \\ Y_P - Y_c \\ Z_P - Z_c \end{pmatrix}^M \\
&= \mathbf{R}_b^c \mathbf{R} \begin{pmatrix} 0 & 0 & -\sin(\theta) \\ 0 & 0 & \cos(\theta) \\ \sin(\theta) & -\cos(\theta) & 0 \end{pmatrix} \begin{pmatrix} X_P - X_c \\ Y_P - Y_c \\ Z_P - Z_c \end{pmatrix}^M \\
&= \mathbf{R}_b^c \mathbf{R} \begin{pmatrix} -\sin(\theta)(Z_P - Z_c) \\ \cos(\theta)(Z_P - Z_c) \\ \sin(\theta)(X_P - X_c) - \cos(\theta)(Y_P - Y_c) \end{pmatrix}^M \tag{A.31}
\end{aligned}$$

$$\begin{aligned}
\frac{\partial}{\partial \psi} \begin{pmatrix} x_{c/p} \\ y_{c/p} \\ z_{c/p} \end{pmatrix}^c &= \mathbf{R}_b^c \frac{\partial \mathbf{R}_{ll}^b}{\partial \psi} \begin{pmatrix} X_P - X_c \\ Y_P - Y_c \\ Z_P - Z_c \end{pmatrix}^M \\
&= \mathbf{R}_b^c \mathbf{R} \begin{pmatrix} 0 & 1 & 0 \\ -1 & 0 & 0 \\ 0 & 0 & 0 \end{pmatrix} \begin{pmatrix} X_P - X_c \\ Y_P - Y_c \\ Z_P - Z_c \end{pmatrix}^M \\
&= \mathbf{R}_b^c \mathbf{R} \begin{pmatrix} Y_P - Y_c \\ -(X_P - X_c) \\ 0 \end{pmatrix}^M \tag{A.32}
\end{aligned}$$